CHARGE DENSITY WAVE FORMATION IN RARE-EARTH TRITELLURIDES

A DISSERTATION
SUBMITTED TO THE DEPARTMENT OF APPLIED PHYSICS
AND THE COMMITTEE ON GRADUATE STUDIES
OF STANFORD UNIVERSITY
IN PARTIAL FULFILLMENT OF THE REQUIREMENTS
FOR THE DEGREE OF
DOCTOR OF PHILOSOPHY

Nancy Ru

March 2008

I certify that I have read this dissertation and that, in my opinion, it is fully adequate in scope and quality as a dissertation for the degree of Doctor of Philosophy.

(Ian R. Fisher) Principal Adviser

I certify that I have read this dissertation and that, in my opinion, it is fully adequate in scope and quality as a dissertation for the degree of Doctor of Philosophy.

(Michael F. Toney)

I certify that I have read this dissertation and that, in my opinion, it is fully adequate in scope and quality as a dissertation for the degree of Doctor of Philosophy.

(Zhi-Xun Shen)

Approved for the University Committee on Graduate Studies.

Abstract

Charge density wave formation is explored in the rare-earth tritelluride family of compounds ($R\mathrm{Te}_3$, R = Y, La–Nd, Sm, Gd–Tm). These quasi-two-dimensional compounds host a simple lattice modulation with very little variance across the series. They have an especially simple electronic structure, which can be easily tuned by chemical pressure via rare-earth substitution.

The Fermi surface (FS) of $R\mathrm{Te}_3$ is derived mainly from the p-orbitals of the Te atoms, which are arranged in double layers of nearly square-planar sheets. Despite the nearly four-fold symmetry of the Fermi surface and electronic structure, it is energetically favorable for $R\mathrm{Te}_3$ to form an incommensurate CDW that is unidirectional, rather than bidirectional—that is, of "stripe" rather than "checkerboard" symmetry. This CDW wavevector lies along one of the in-plane directions and partially nests nearly-parallel regions of the FS.

In this thesis, I present the results of resistivity and high resolution x-ray diffraction measurements that follow the CDW transition temperatures across the $R\mathrm{Te}_3$ series. Critical temperatures T_{c1} were found to vary remarkably across the series, attributed to the subtle effects of chemical pressure on the electronic structure. For the compounds with the smallest lattice parameters (R = Dy, Ho, Er, Tm), second CDW transitions were observed at lower temperatures T_{c2}. X-ray diffraction measurements

for $ErTe_3$ revealed this to be the onset of a CDW with wavevector lying in the in-plane direction perpendicular to the first, which is reminiscent of bidirectional order. Yet, as this second CDW forms at a lower temperature than the first, and nests a Fermi surface that has been previous nested, this CDW state with two order parameters for perpendicular wavevectors may be more appropriately termed a "rectangular" state.

Quantum oscillation studies are also presented that probe the reconstructed FS of $LaTe_3$. Additionally, antiferromagnetism arising from the local moments on the rare earth ions is explored, with Néel temperatures generally much lower than the CDW transition temperatures.

The measurements presented in this thesis establish RTe_3 as a model CDW system and a potential "toy box" for future study.

Acknowledgements

Over the long process of completing my Ph.D. many people have taught me, helped me, or have otherwise made my graduate student experience richer and fuller.

First of all, I would like to thank my advisor, Ian Fisher, for his continued patience, optimism and good cheer. Ian has been a great advisor, involved and always enthusiastic, and it's been a good experience working on my Ph.D in the Fisher group.

My labmates in the Fisher group have been fun and supportive. The students in the year ahead of me - Suchitra, Yana, and Kyungyun - broke ground as the first students in the group, and served as older siblings in the doing of new things. Milestones like taking the qual, traveling to experiments, and going to conferences were all easier to approach knowing that I had their support. Seeing first-hand how Suchitra and Yana defended and wrote their theses made it easier for me to go through that process myself. Thanks to Suchitra for much practical and moral support, for travel and adventures, and for continued help and advice even from overseas. I am grateful to Yana for being always a source of sympathy as well as of experimental knowledge. Kyungyun and I have had many discussions about CDWs and career decisions, and he is a great partner to have on long beamline sessions. Ann has been a supportive labmate, easy-going and always up for making celebratory posters. It's been fun chatting with Eric on our breaks from work or at Monday donuts, and with

Jiun-Haw the $R\mathrm{Te}_3$ project is in perhaps better hands than mine. Thanks to you all for being such great labmates. We celebrated many birthdays, quals, and thesis defenses together.

The beamline was the arena of some of my most intense and rewarding research experiences. I owe Mike Toney for teaching me everything I know about x-ray diffraction and for being a good mentor; I am honored to have him on my thesis committee. Cathie Condron was always cheerful and upbeat and was a good companion to have on the beamline.

One of the most rewarding aspects of my graduate student experience has been the opportunity to work with so many collaborators. Z.-X Shen, Veronique Brouet, Rob Moore, Ruihua and Felix worked on ARPES experiments that were complimentary to my own in often very exciting ways. Conversations with Veronique early on in my research were invaluable for gaining an understanding of $R\mathrm{Te}_3$, while Rob's investigation of ErTe_3 was remarkably synergistic with my own work on ErTe_3. Alan Fang and I had many discussions about his STM data and I also appreciate Alan's help with fixing things around the lab and his advice on auto repair. Hong Yao, Eun-Ah Kim, and Steve Kivelson discussed CDW theory with me and provided numerous insights on $R\mathrm{Te}_3$. I've had numerous good discussions with Jude Laverock and Stephen Dugdale, although most of them were carried out remotely. Andy Mackenzie, Chufo Borzi, and Andreas Rost were gracious hosts during my visits to St. Andrews. Many thanks to Z.-X Shen, Steve Kivelson, and Mac Beasley for joining my thesis committee.

Undergraduate assistants have also contributed to this research project. I very much appreciate George's careful experimental expertise and initiative and for sharing with me the excitement of discovering the CDW transitions.

GLAM would not be the same without the warm and friendly presences of Larry,

Corrina, Mark and Lily. I especially appreciate all of Mark's efforts in shipping our samples to collaborators. Thanks to Lily for her thoughtful help in setting up for my defense. At the SNL, I learned a great deal about TEM measurements from Ann Marshall and Arturas provided much assistance with x-ray diffraction. Thanks also to Paula and Claire in AP for the hearty welcome when I arrived as a first-year student and for checking up on me in the years since then.

Without the friends I've made at Stanford, graduate student life would not have been as interesting or fun. Most of you celebrated with me after my oral defense. The Stanford Taiji class has been a great source for companionship in the pursuit of my martial arts, as well as for commiserations on graduate student life. Janice, Chuck, Pearline, Yves, Serena, and George have been good friends. Thanks also to Chuck for being always a clearheaded sounding board and for much support during the writing of this thesis. Finally, I would like to thank my parents for always encouraging me to pursue science.

Contents

Chapter 1

Introduction

As presented in this thesis, the rare-earth tritellurides $R\mathrm{Te}_3$ (R = rare earth) form an incommensurate charge-density wave at the transition temperature T_{c1} with wavevector $q_1 \approx 2/7\ c^*$. The heavier rare earth compounds (R = Dy, Ho, Er, Tm) undergo a second CDW transition at a lower temperature T_{c2} with wavevector $q_2 \approx 1/3\ a^*$ as measured in ErTe_3. The phase diagram for the CDW transitions in $R\mathrm{Te}_3$ is illustrated in Fig. 1.1 and is the result of experiments described in Chapter 4.

This introduction gives a brief outline of charge-density waves and describes how they manifest in the $R\mathrm{Te}_3$ system. The crystal and electronic structure of $R\mathrm{Te}_3$ is presented, as well as calculations of the susceptibility $\chi(q)$ and theoretical work investigating "stripe" versus "checkerboard" order. An overview of experimental literature is presented including results for angle-resolved photoemission (ARPES), scanning tunneling microscopy (STM), thermodynamic and transport measurements for $R\mathrm{Te}_3$ within the q_1 CDW state. Finally, an outline is given for the subsequent chapters of this thesis.

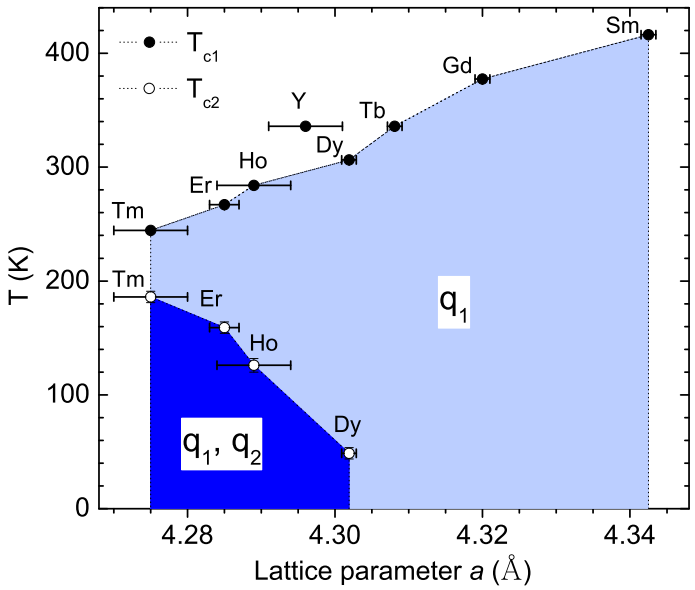

Figure 1.1: The CDW transition temperatures T_{c1} and T_{c2} for each $R\mathrm{Te}_3$ compound, plotted as a function of the lattice parameter a. Below T_{c1} a CDW forms with wavevector q_1. Below T_{c2} an additional CDW forms for $R =$ Dy, Ho, Er, and Tm with wavevector q_2. This phase diagram is the result of the experimental work described in Chapter 4.

1.1 Charge Density Waves

A charge density wave (CDW) is a periodic distortion in the density of charge-carriers with an accompanying distortion in the lattice. This discussion is limited to those CDWs that arise from nesting of the band structure near the Fermi surface (FS), a state that occurs in systems with highly anisotropic Fermi surfaces. CDWs can be found in 1D chain compounds such as $NbSe_3$, or layered 2D materials such as RTe_3.

The following introduction to CDWs closely follows the treatment given by G. Gruner in "Density Waves in Solids[1]."

1.1.1 Susceptibility $\chi(q)$

The response of an electron gas to a time-independent potential ϕ is described by

$$\rho^{ind}(\vec{q}) = \chi(\vec{q})\phi(\vec{q}) \tag{1.1}$$

where the potential ϕ and the induced charge ρ^{ind} are given in terms of their fourier components, and $\chi(\vec{q})$ is the Lindhard response function, or susceptibility, given in d dimensions by

$$\chi(q) = \int \frac{d\vec{k}}{2\pi^d} \frac{f_k - f_{k+q}}{\epsilon_k - \epsilon_{k+q}} \tag{1.2}$$

where $f_k = f(\epsilon_k)$ is the Fermi function.

The susceptibility is very sensitive to the topology of the band structure near the Fermi surface. The states k and $k+q$ that contribute most to the integral are those for which the denominator of the integrand is small (states close in energy) and the numerator is close to one—that is, a pair consisting of an occupied and unoccupied state near the Fermi surface. As shown for the 1D case in Fig. 1.2, such a condition is

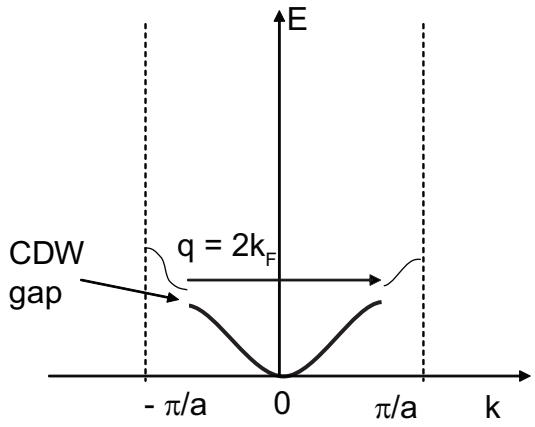

Figure 1.2: The CDW for a purely 1D system. A charge density results in a gap at the Fermi energy and a new periodicity of $2k_F$.

satisfied with the wavevector $q_{CDW} = 2k_F$. A calculation of $\chi(q)$ for a 1D electron gas shows a divergence at the wavevector q_{CDW}=$2k_F$. (Fig. 1.3) The 1D gas is unstable to perturbations and will form a standing wave with wavevector $q_{CDW} = 2k_F$.

This redistribution of charge creates a gap at the Fermi surface, and on formation of the CDW, the former metal becomes a semiconductor. This results in a gain in one-electron energy as occupied states near the Fermi surface are lowered in energy. The charge redistribution pulls the lattice away from its neutral positions. This lattice modulation costs energy, balancing the gain in one-electron energy.

The Fermi surface is "nested" by q_{CDW}, which introduces a new periodicity to the system, generally incommensurate to the lattice periodicity.

While for the 1D case, a single wavevector can nest all portions of the Fermi surface, this is no longer the true for higher dimensions, as can be seen for the 2D and 3D cases in which the representative Fermi surfaces are taken as a circle and a sphere, respectively. The corresponding susceptibility curves, shown in Fig. 1.3, do not show a divergence at $q = 2k_F$. The Fermi surface of $R\mathrm{Te}_3$, as explained in 1.2.3, is quasi-2D with sections that are nearly parallel. In such a case, a particular

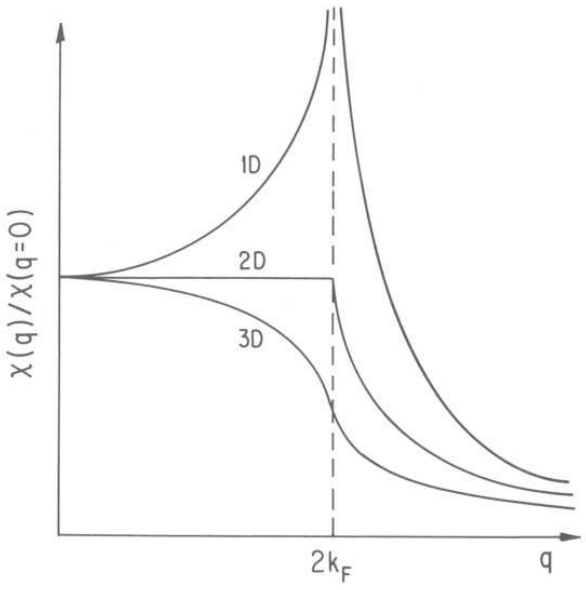

Figure 1.3: The susceptibility $\chi(q)$ for purely 1D, 2D, and 3D systems. From G. Gruner, *Density Waves in Solids*[1].

wavevector can nest portions of the FS, which leads to a partially nested Fermi surface that continues to display metallic behavior in the CDW state.

While "Fermi surface nesting" is common terminology, and much can be inferred about possible CDW nesting vectors by "eyeing" the FS topology, portions of the band above and below the FS also contribute to $\chi(q)$, and so a formal calculation of the susceptibility is necessary to determine realistic nesting vectors[2].

The susceptibility curves shown in Fig. 1.3 are for $T = 0$. As T is increased from zero, the peak in the susceptibility becomes smaller and broader. For the 1D case, the peak amplitude has a logarithmic dependence on temperature, given by

$$\chi(q = 2k_F, T) = -e^2 n(\epsilon_F) \ln \frac{1.14\epsilon_0}{k_B T} \tag{1.3}$$

where $n(\epsilon_F)$ is the density of states at the Fermi energy.

1.1.2 Kohn Anomaly

By considering the electron-phonon interaction within a mean-field approximation, the renormalized phonon dispersion relation for the 1D model can be derived and an expression obtained for the mean-field CDW transition temperature.

The Frölich Hamiltonion is given by

$$H = \sum_k \epsilon_k a_k^\dagger a_k + \sum_q \hbar\omega_q b_q^\dagger b_q + \sum_{k,q} g_q a_{k+q}^\dagger a_k (b_{-q}^\dagger + b_q) \tag{1.4}$$

where the first term is the Hamiltonion of the electron gas, where $a^\dagger$ and a are creation and annihilation operators. The second is that of the phonons with $b^\dagger$,b the phonon creation and annihilation operators. The third represents the electron-phonon interaction where the q-dependent electron-phonon coupling constant is

$$g_q = i\left(\frac{\hbar}{2M\omega_q}\right)^{1/2} |q| V_q \tag{1.5}$$

To derive the renormalized phonon spectrum, consider the equation of motion

$$\hbar^2 \ddot{Q}_q = -[[Q_q, H], H] \tag{1.6}$$

which on insertion of the Hamiltonion and utilizing the commutation relations $[Q_q, P_{q'}] = i\hbar\delta_{q,q'}$ becomes

$$\ddot{Q}_q = -\omega_q^2 Q_q - g\left(\frac{2\omega_q}{M\hbar}\right)^{1/2} \rho_q \tag{1.7}$$

where the second term represents a potential energy $U = g\left(\frac{2M\omega_a}{\hbar}\right)^{1/2} \rho_q Q_q$ of the electron-phonon interaction. Inserting the expression $\rho^{ind}(\vec{q}) = \chi(\vec{q})\phi(\vec{q})$ with $\phi =$

U/ρ into Eq. 1.7, the following expression is obtained:

$$\ddot{Q}_q = -\left[\omega_q^2 + \frac{2g^2\omega_q}{M\hbar}\chi(q,T)\right]Q_q \tag{1.8}$$

The expression in the brackets is the renormalized phonon spectrum.

The mean-field transition temperature can be now be derived for the 1D model by using the expression for $\chi(q)$ as derived in Section 1.1.1. As $\chi(q)$ is largest for $q = 2k_F$, $\chi(q = 2k_F, T)$, Eq. 1.3 is used to obtain the phonon frequency for the wavevector $q = 2k_F$ as a function of temperature:

$$\omega_{ren,2k_F}^2 = \omega_{2k_F}^2 - \frac{2g^2 n(\epsilon_F)\omega_{2k_F}}{\hbar}\ln\left(\frac{1.14\epsilon_0}{k_B T}\right) \tag{1.9}$$

which goes to zero (freezes) at the mean-field transition temperature

$$k_B T_{CDW}^{MF} = 1.14\epsilon_0 e^{(-1/\lambda)} \tag{1.10}$$

where $\lambda = \frac{g^2 n(\epsilon_F)}{\hbar\omega_{2k_F}}$ is the dimensionless electron-phonon coupling constant.

The above equation (Eq. 1.10) is also the expression for the mean-field transition temperature for BCS superconductivity. Charge density waves can be described within a BCS framework in which electron-hole pairing is considered instead of electron-electron paring. In addition to Eq. 1.10, other relevant BCS expressions include

$$2\Delta = 3.52 k_B T_{CDW}^{MF} \tag{1.11}$$

relating the mean-field transition temperature to the order parameter Δ. The temperature dependence of the order parameter can be calculated numerically and is shown in Fig. 1.4.

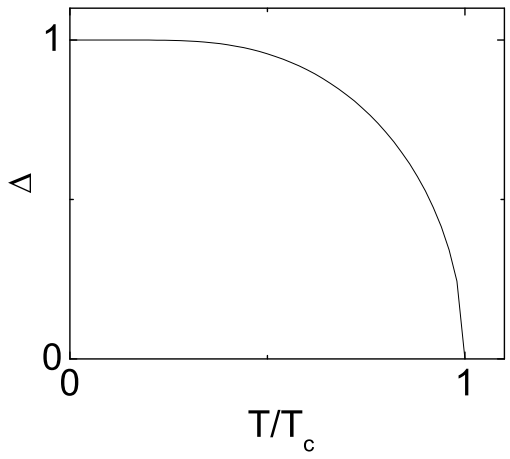

Figure 1.4: The BCS order parameter as a function of reduced temperature T/T_c.

1.2 Rare-earth tritellurides

1.2.1 Crystal structure

RTe$_3$ is composed of doubled sheets of nearly square planar tellurium (Te) separated by a corrugated R-Te slab, as shown in Fig. 1.5. The average crystal structure (i.e. the unmodulated structure above the CDW transitions), is orthorhombic and belongs to the space group $Cmcm$[4].[1] The convention for this space group labels the long axis as the b-axis and the in-plane axes as a and c. Though this may be non-intuitive, this is the notation that will be followed in this thesis, along with the corresponding reciprocal lattice units (r.l.u.) as denoted by HKL (e.g. H in units of $a^*= 2\pi/a$, K in units of $b^*= 2\pi/b$, L in units of $c^*= 2\pi/c$).

Although orthorhombic symmetry implies an asymmetry between the a and c

[1]There exists is an alternate unit cell for RTe$_3$ as described in Ref.[5] that contains only two formula units per cell, as opposed to the four formula units per cell for the unit cell illustrated here.

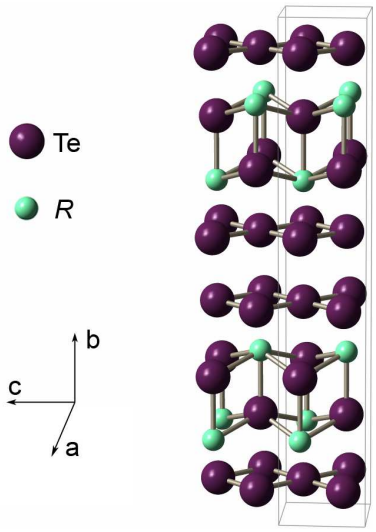

Figure 1.5: The crystal structure of $R\mathrm{Te}_3$ with unit cell outlined. $R\mathrm{Te}_3$ contains two double layers of nearly square-planar Te separated by an R-Te interlayer. The space group symmetry is orthorhombic. (Crystal structure generated using *Balls & Sticks*[3].)

orientations - 2-fold rather than 4-fold symmetry about the b-axis, it might be difficult to acquire an intuitive feel for this asymmetry by casually perusing the crystal structure diagram. As the electronic structure of $R\mathrm{Te}_3$ is often simplified by using a tetragonal model, where $a = c$, it is worth describing here the details that give $R\mathrm{Te}_3$ its orthorhombic nature.

The space group $Cmcm$ contains a glide plane located halfway down the b-axis, between the doubled tellurium layers. This glide plane indicates that if the top half of the unit cell is translated by $c/2$, it will then reflect across this plane to map directly onto the bottom half of the unit cell. This symmetry occurs only in the c and not the a direction, resulting in the two orientations being inequivalent.

An alternate description is provided by considering the related compound $R\mathrm{Te}_2$ which contains a single Te layer. The crystal structure, as shown in Fig. 1.6, has tetragonal symmetry. (Its long axis is its c-axis, but that distinction can be ignored

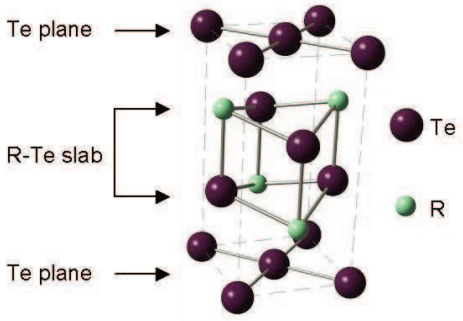

Figure 1.6: The crystal structure of the related compound rare-earth ditelluride (RTe$_2$)[6]. RTe$_2$ contains a single tellurium sheet and has a tetragonal space group symmetry (space group P4/nmm).

for now.) On putting two units of RTe$_2$ one on top of the other, with one of the units offset by $a/2$, the symmetry is reduced and we create the orthorhombic RTe$_3$ crystal structure.

There is a resulting very small difference in the magnitudes of the in-plane lattice parameters a and c. For TbTe$_3$ at room temperature, c larger than a by 0.13%, as described in more detail in 4.2.1.

The subtlety of the of 2-fold symmetry in RTe$_3$ leads us to speak of the system as being "weakly" orthorhombic. The square-planar Te planes, which dominate the electronic structure are nominally tetragonal. When considering the Te planes on their own, we often refer to a "2D" unit cell that contains only a single Te atom. This 2D unit cell is $\sqrt{2}$ smaller than the original "3D" unit cell, and rotated by 45 degrees. It has an associated 2D Brillouin zone (BZ) which is $\sqrt{2}$ larger than the 3DBZ, and rotated by 45 degrees. The 2DBZ is used in the tight-binding model description, as described later in this chapter.

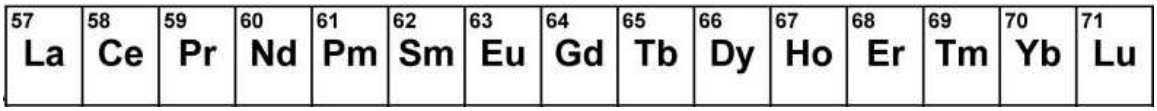

Figure 1.7: The rare earths (lanthanides).

1.2.2 Role of the rare earth ion

Rare earths and chemical pressure

The rare earths, also known as the lanthanides, are the $4f$ series that lie near the bottom of the periodic table. Figure 1.7 shows the rare earth series as shown on a periodic table. The similarity of the electronic properties across the series often enables a rare-earth containing compound to form for more than one of the rare-earth elements. In particular, $R\mathrm{Te}_3$ forms for nearly all the elements. This enables us to use "chemical pressure" as a tuning parameter. As we move along the series from left to right on the periodic table, the molar mass becomes steadily heavier, but the size of the atom becomes smaller as the nucleus gains protons and become more highly charged, attracting the orbitals inwards. Thus for $R\mathrm{Te}_3$ chemical pressure increases as R goes from lighter to heavier rare earths, with a corresponding decrease in the size of the unit cell (as known as "lanthanide contraction").

Rare-earth magnetism

As shown in Table 1.1, nearly all the rare earths ionize to 3+, leaving the $4f$ shell as the only unfilled shell. These $4f$-electrons are strongly localized and lie closer to the atomic core than the completely filled $5s^2$ and $5p^6$ shells[7]. As a result, the magnetic moments resulting from the partially filled $4f$ shell can be considered as local moments.

The ground state configuration of the partially filled $4f$ shell is governed by Hund's

Rare earth	Shell Config.	Ion	Shell Config.	S	L	J	p_{eff}
La	[Xe]$5d6s^2$	La^{3+}	[Xe]	0	0	0	0
Ce	[Xe]$4f^26s^2$	Ce^{3+}	[Xe]$4f^1$	1/2	3	5/2	2.54
Pr	[Xe]$4f^36s^2$	Pr^{3+}	[Xe]$4f^2$	1	5	4	3.58
Nd	[Xe]$4f^46s^2$	Nd^{3+}	[Xe]$4f^3$	3/2	6	9/2	3.62
Pm	[Xe]$4f^56s^2$	Pm^{3+}	[Xe]$4f^4$	2	6	4	2.68
Sm	[Xe]$4f^66s^2$	Sm^{3+}	[Xe]$4f^5$	5/2	5	5/2	0.85
Eu	[Xe]$4f^76s^2$	Eu^{3+}	[Xe]$4f^6$	3	3	0	0
Gd	[Xe]$4f^75d6s^2$	Gd^{3+}	[Xe]$4f^7$	7/2	0	7/2	7.94
Tb	[Xe]$4f^96s^2$	Tb^{3+}	[Xe]$4f^8$	3	3	6	9.72
Dy	[Xe]$4f^{10}6s^2$	Dy^{3+}	[Xe]$4f^9$	5/2	5	15/2	10.63
Ho	[Xe]$4f^{11}6s^2$	Ho^{3+}	[Xe]$4f^{10}$	2	6	8	10.60
Er	[Xe]$4f^{12}6s^2$	Er^{3+}	[Xe]$4f^{11}$	3/2	6	15/2	9.59
Tm	[Xe]$4f^{13}6s^2$	Tm^{3+}	[Xe]$4f^{12}$	1	5	6	7.56
Yb	[Xe]$4f^{14}6s^2$	Yb^{3+}	[Xe]$4f^{13}$	1/2	3	7/2	4.53
Lu	[Xe]$4f^{14}5d6s^2$	Lu^{3+}	[Xe]$4f^{14}$	0	0	0	0

Table 1.1: The electronic shell configurations for rare-earths and their ions. After ionization, the $4f$ shell remains the only unfilled shell. The S, L, and J values for the Hund's rule groundstates are shown, along with the corresponding effective moments p_{eff}. (A few rare earth elements will sometimes ionize to valencies other than 3+, e.g. Ce^{3+} vs. Ce^{4+}, Eu^{2+} vs. Eu^{3+}, Yb^{2+} or Yb^{3+}.) Promethium (Pm) is radioactive.

rules (see for example Ref.[8]). In order of priority, the Hund's rules are

1. Fill states as to maximize total spin S.

2. Fill states as to maximize total orbital angular momentum L.

3. If the shell is less than half filled, the total angular momentum $J = |L - S|$. If the shell is more than half filled, $J = |L + S|$.

The S, L, and J values for the rare earths ions are shown in Table 1.1. This results in an dimensionless effective moment $p_{eff} = \mu_{eff}/\mu_B = g_J[J(J+1)]^{1/2}$ where g_J is the Landé g-factor. Values for p_{eff} are shown in Table 1.1 (after Ref.[8])

$R\mathrm{Te}_3$ orders antiferromagnetically at temperatures much lower than the CDW transition temperatures. Experiments probing the long range magnetic order of $R\mathrm{Te}_3$ are described in Ch. 6.

1.2.3 Electronic Structure

The electronic structure of $R\mathrm{Te}_3$ is often described by a tight-binding model which considers a single square-planar Te layer[9, 10, 11, 12]. This model is presented below and compared with full band structure calculations for $R\mathrm{Te}_3$.

Tightbinding model

The electronic structure can be modeled by a tight-binding bands as have been described by many authors[9, 10, 11, 12]. The following discussion follows closely that presented by Brouet *et al*[9] and Yao *et al*[11]. The tight-binding bands are easy to understand and this model lends to insight into the dimensionality of the $R\mathrm{Te}_3$ system.

The tight-binding model considers the p bands of a single square-planar Te sheet, with band filling adjusted to match that of $R\mathrm{Te}_3$, which includes electrons donated from the R-Te interlayer. As Te ionizes to Te^{2-} and the rare earth ionizes to R^{3+}, each R-Te unit donates one electron to the doubled Te sheets, which is shared by two Te atoms. As the neutral Te atom has the filling $[Kr]4d^{10}5s^25p^4$, the additional electron brings the filling of the p bands to $5p^{4.5}$. As shown in band calculations by Kikuchi *et al.*[13] and Laverock *et al.*[5], the p_y orbitals, which in our notation is the out-of-plane orientation, lie at a lower energy relative to the other p orbitals and are completely filled. The remaining 2.5 electrons are shared between the $5p_x$ and $5p_z$ orbitals ($2.5/4 = 5/8$ filling).

The p_x and p_z orbitals are shown in Fig. 1.8(a). $t_{||}$ represents hopping along the length of the extended p orbital while $t_\perp$ represents transverse hopping. t', a second-nearest-neighbor hopping, is the shortest-range interaction that mixes the p_x and p_z bands. These parameters have been determined by V. Brouet[9, 10] using the bands

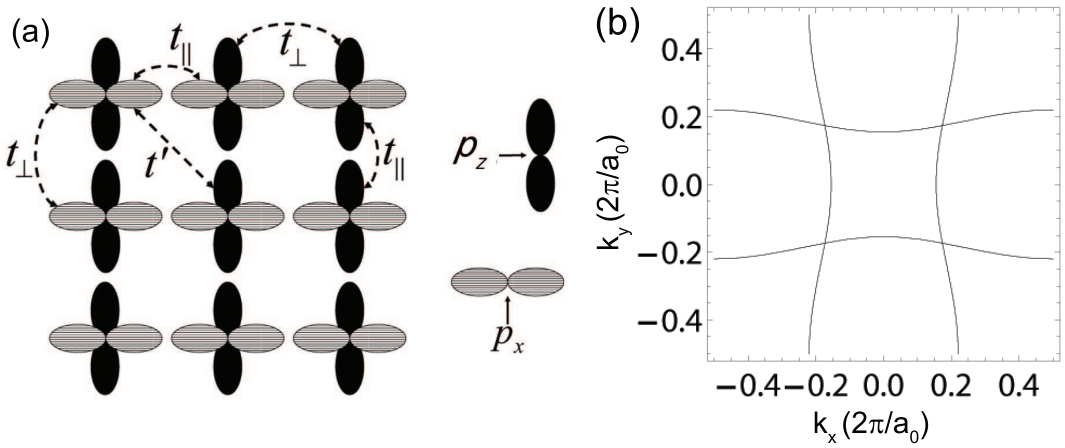

Figure 1.8: (a) p-orbitals and hopping for square-planar Te, as reprinted from Yao *et al.*[11] (b) The FS in the 2DBZ as obtained from the tight-binding bands.

calculated by Kikuchi[13] and are $t_{||}$ = -2 eV, $t_{\perp}$ = .37 eV, and $t' \approx$ .16 eV. However as t' is very small and can be neglected for this model, which contains no hybridization between p_x and p_z bands.

This results in the following equations for the tight-binding bands - one for p_x and one for p_z:

$$E_k(k_x) = -2t_{||}cos[(k_x)a_0] + 2t_{\perp}cos[(k_z)a_0] \tag{1.12}$$

$$E_k(k_z) = -2t_{||}cos[(k_z)a_0] + 2t_{\perp}cos[(k_x)a_0] \tag{1.13}$$

where a_0 is the 2D lattice constant, with magnitude $\sqrt{2}$ smaller than the 3D unit cell in-plane lattice constant.

The tightbinding FS is plotted in Fig. 1.8(b) with bands filled to E_F = 1.5 eV. They are two sets of nearly parallel curves. This lends a quasi-1D character to the band structure. As the curvature of the bands is given by $t_{\perp}/t_{||}$, if $t_{\perp}$ were zero, the FS sheets would be perfectly flat, and the system would be completely 1D, albeit

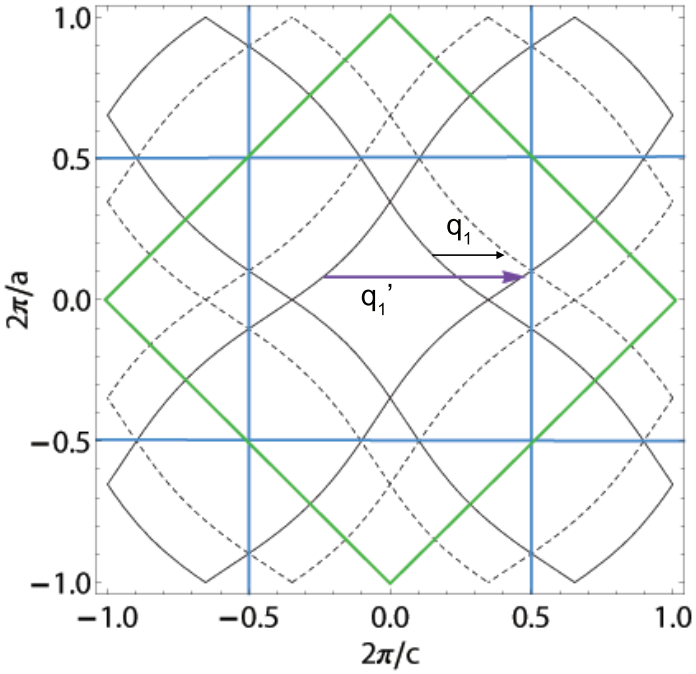

Figure 1.9: Fermi surface shown in the 3DBZ, as obtained by the tightbinding model. Solid curves represent the original 2DBZ bands. Dashed curves are those folded by the 3DBZ periodicity. The blue lines mark the 3DBZ and the larger green square is the 2DBZ. The arrows mark the CDW wavevector $q_1 \approx 2/7\ c^*$ and its alternate form $q_1' \approx 5/7\ c^*$.

with 4-fold symmetry.

To include effects of the "3D unit cell", we rotate the bands by 45 degrees and express them in terms of the 3D lattice constant:

$$E_k(k_x, k_z) = -2t_{||}cos[(k_x + k_z)a/2] + 2t_{perp}cos[(k_x - k_z)a/2] \tag{1.14}$$

$$E_k(k_x, k_z) = -2t_{||}cos[(k_x - k_z)a/2] + 2t_{perp}cos[(k_x + k_z)a/2] \tag{1.15}$$

Additionally, the bands are translated by the "3DBZ" periodicity $2\pi/a$, or equivalently, reflected across the 3DBZ boundaries. Fig. 1.9 shows the 3DBZ where the

solid lines are the original FS and the dashed lines are those translated by the 3D periodicity.

As described in the following sections, the CDW wavevector q_1 is expressed as either $q_1 \approx 2/7\ c^*$ or $q_1' \approx 5/7\ c^*$. While q_1 falls within the first 3DBZ and is the commonly accepted notation for diffraction data, ARPES and STM results show that the magnitude of q_1' may have more physical meaning. As shown in Fig. 1.9, the q_1' wavevector lies outside of the first Brillouin zone, but nests two sets of solid black lines, as opposed to one solid and one dashed line for q. In the absence of coupling to the 3D unit cell, q' would still be a valid nesting vector.

As the curvature of the FS is given by the ratio $t_{perp}/t_{||}$, changes in the lattice constant are anticipated to cause only minimal changes in the topology of the FS. However the band width (to which the density of states at the Fermi level, $n(\epsilon_F)$, is closely related) is directly proportional to $t_{||}$, and $n(\epsilon_F)$ would be expected to rise linearly with the expansion of the lattice. In Ch. 4, changes in the lattice constant as a result of chemical pressure is shown to have a direct effect on the CDW transition temperature via changes in $n(\epsilon_F)$.

Full band structure

The full band structure for the average structure - the structure above the CDW transition - has been calculated from first principles by J. Laverock *et al.* and Fig. 1.10 shows the resulting band structure and Fig. 1.11 shows the Fermi surface sheets. It is very similar to that obtained from the tight-binding bands alone. The differences are mainly (a) hybridization at band crossings and (b) a doubling of the FS sheets, also called a bi-layer splitting, that arises from the doubled Te sheets which gives rise to a degeneracy in the p-bands. There is a very slight dispersion along the b^* axis,

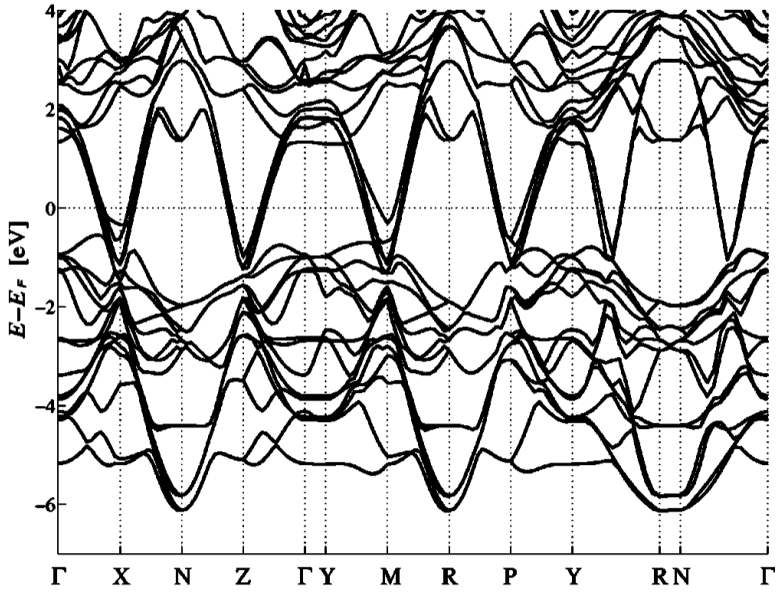

Figure 1.10: Band structure for $LuTe_3$ as calculated from first principles by Laverock *et al*[5].

although the FS is definitely quasi-2D. The inner diamonds are hole surfaces and the outer sheets are electron surfaces.

Although this band structure incorporates the full orthorhombic crystal structure, anisotropy between the two in-plane directions a and c is very hard to distinguish. There are some small differences at the tips of the diamonds.

1.2.4 Susceptibility $\chi(q)$

The susceptibility $\chi(q)$ is shown for the tight-binding model and full band structure. These calculations show the likelihood of a CDW forming from the undistorted FS and can be compared with experimental results in the q_1 regime. The second CDW q_2 forms from a FS that is already gapped by the first CDW and separate calculations starting from this gapped FS would be needed to obtain $\chi(q)$ values for q_2.

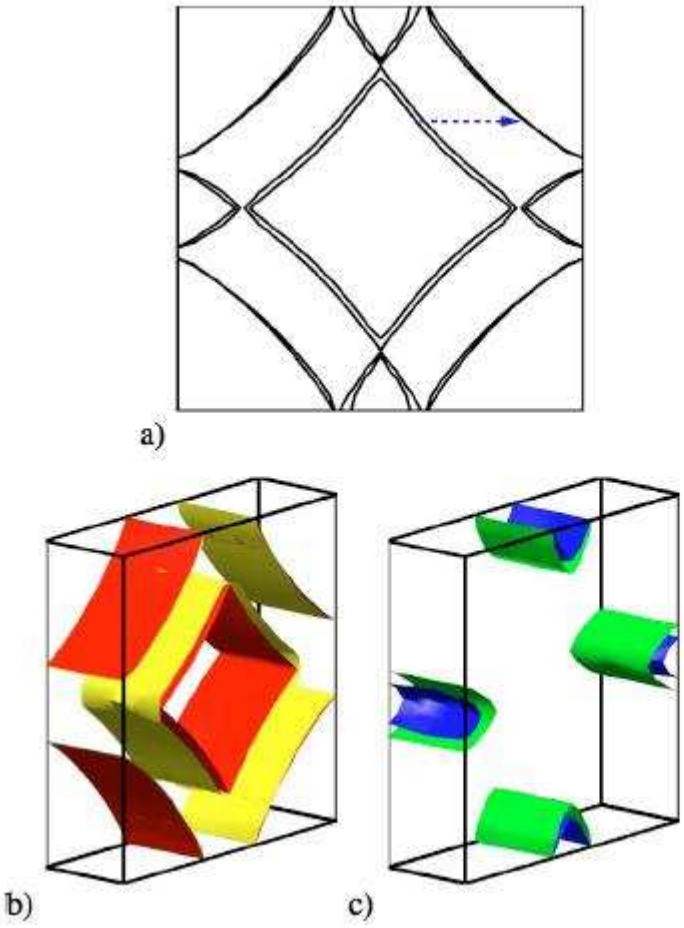

Figure 1.11: Fermi surface for $LuTe_3$ as calculated from first principles by Laverock *et al*[5] (a) on a (010) plane through Γ with an arrow marking 2/7 c^*. (b) The outer FS sheets. (c) The inner FS sheets.

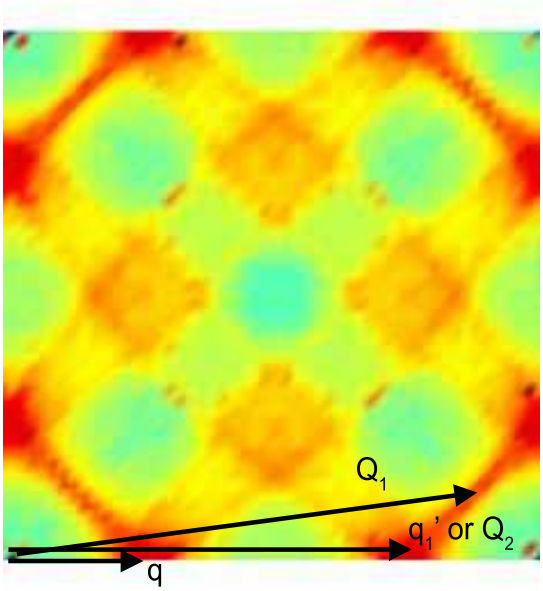

Figure 1.12: Susceptibility $\chi(q)$ for tightbinding bands, as calculated by K. Y. Shin[14]. The origin is in the lower left corner and the dimensions are $a^* \times c^*$ (3DBZ). Higher intensity regions are in red and lower intensity regions in green. Arrows mark the experimentally observed wavevectors q_1 and q_1', as well as Q_1 and Q_2 (same as q_1') as described in Ref.[11].

Susceptibility using tightbinding bands

Figure 1.12 shows the susceptibility $\chi(q)$ as calculated by K. Y. Shin[14]. One 3DBZ is shown. The experimentally observed q_1' is marked. As the bands were folded into the 3DBZ for this calculation, the 3DBZ value of $q_1 = c^*\text{-}q_1'$ is also observed in the susceptibility. As seen in Fig. 1.9, these wavevectors indeed nest parallel regions of the FS.

Yao *et al.* explored the competition between "stripe" and "checkerboard" order for wavevectors that they refer to as Q_1 and Q_2. While Q_2 is the same as the experimentally observed q_1', Q_1 marks the center of a ridge of high-intensity in the susceptibility as shown in Fig. 1.12. The competition between Q_1 and Q_2 is described further in 1.2.5.

Susceptibility using the full band structure

The susceptibility $\chi(q)$ has been calculated for the full band structure by Johannes and Mazin[2], as shown in Fig. 1.13. As in the tightbinding model, the dominant features are peaks at $q_1 \approx 2/7$ and $q_1' \approx 5/7$ along a^* and c^*. The susceptibility is remarkably symmetric between the a^* and the c^* directions. The peaks in the c^* direction are very slightly higher than those in the a^* direction, which for an isotropic electron-phonon coupling will prompt the CDW q_1 to choose the c direction orientation.

1.2.5 "Stripes" vs "Checkerboard"

Despite the nearly four-fold symmetry of the band structure and the calculated susceptibility, the q_1 CDW always forms unidirectionally and in the c direction and not along the a direction. An intuitive explanation for this is that once the CDW forms along one direction, not enough FS remains for a CDW to form along the other direction, and the very subtle effects of the crystal structure's orthorhombic symmetry cause the CDW to chose the c direction every time.

The competition between "stripe" (unidirectional) and "checkerboard" (bidirectional) order has been rigorously explored by Yao *et al.* They considered two candidates for the CDW wavevector, Q_1 and Q_2, as shown in Fig. 1.14(a) for the 2D tightbinding bands. A single wavevector Q_1 nests one set of either p_x or p_z very well while a single wavevector Q_2 nests both sets equally but less well. As a result, if Q_1 forms it would have checkerboard symmetry whereas if Q_2 forms it would have stripe symmetry. As shown in Fig. 1.14(b), Q_2, which nests more of the Fermi surface, is favored for higher transition temperatures while Q_1 is favored for lower transition temperatures.

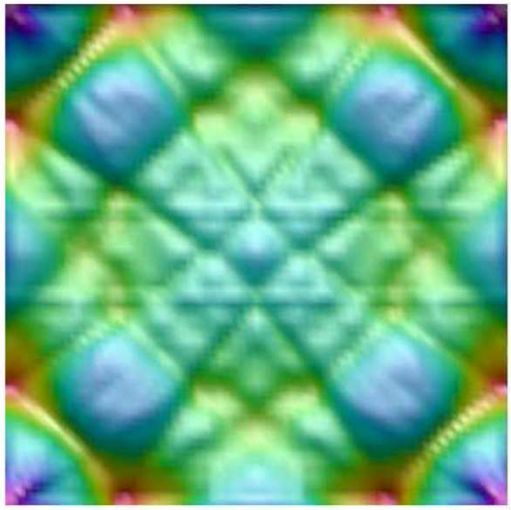

top view

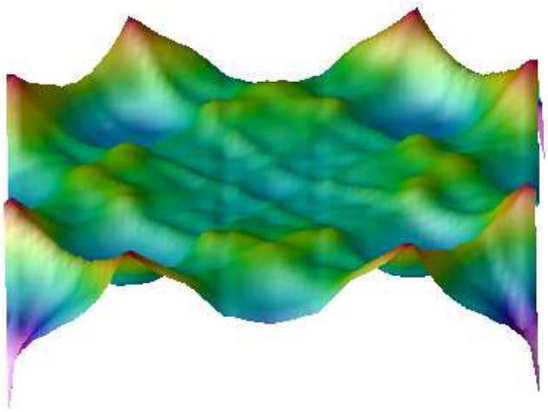

side view

Figure 1.13: $\chi(q)$ for full band structure as calculated by Johannes and Mazin.[2] As in Fig. 1.12(a), the origin is in the lower left corner and the dimensions are $2\pi/a \times 2\pi/c$

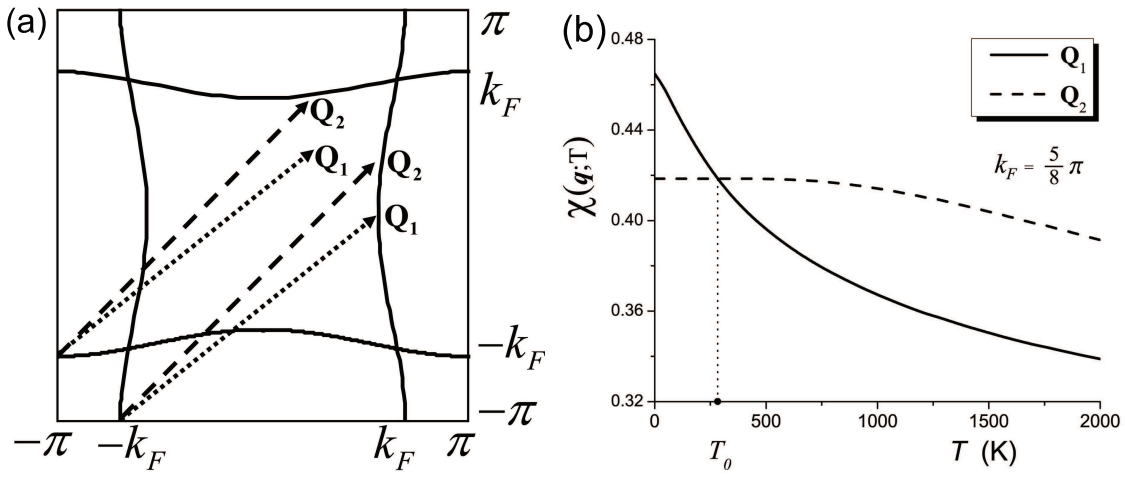

Figure 1.14: (a) Q_1 and Q_2 shown on the 2D tightbinding FS. Units for are for the 2DBZ. (b) Susceptibility $\chi(q)$ for Q_1 and Q_2. Q_2 is favored at higher transition temperatures, while Q_1 is favored for lower transition temperatures. From Ref.[11].

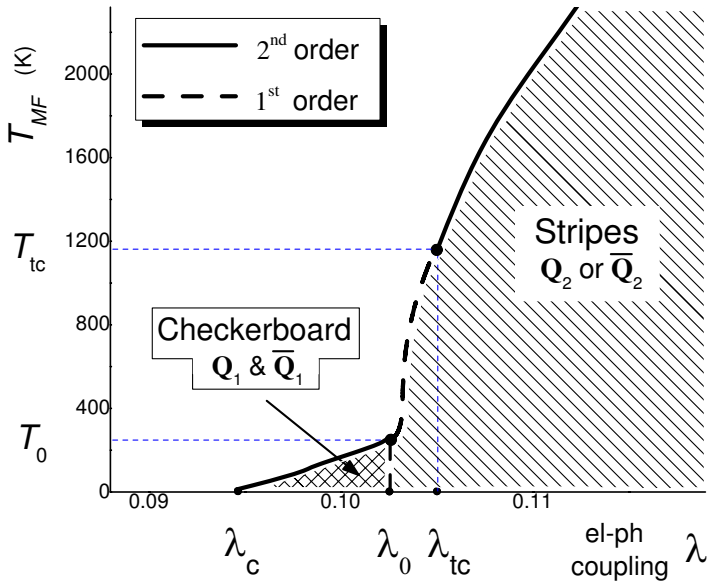

Figure 1.15: Stripe versus checkerboard order for $R\mathrm{Te}_3$ as calculated by Yao *et al*[11]. The y-axis is the mean-field transition temperature.

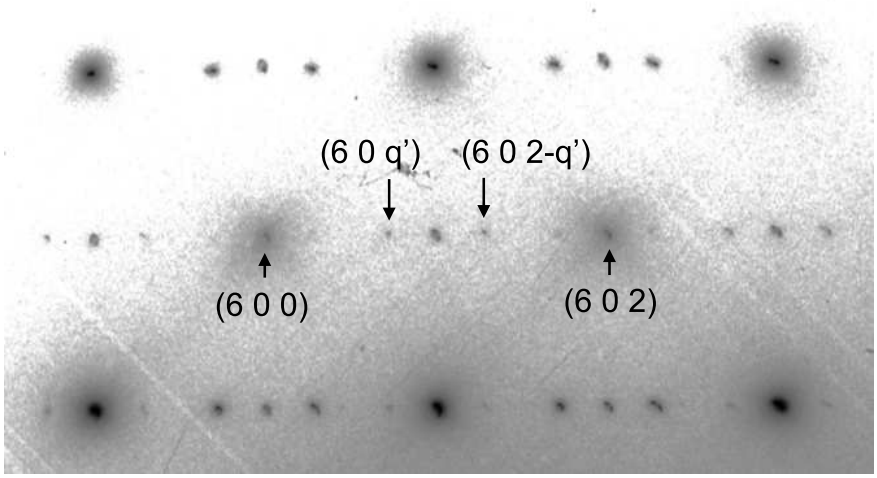

Figure 1.16: TEM of $ErTe_3$ along [010] at 118 K with select average lattice and superlattice reflections labeled.

The resulting phase diagram is shown in Fig. 1.15 with electron-phonon coupling along the x-axis and the mean-field transition temperature as the y-axis. A larger electron-phonon coupling leads to a higher mean-field transition temperature which selects for the stripe Q_2 phase. As described in following section, ARPES measurements of the gap [9, 10] correspond to mean-field transition temperatures (1500 - 2600 K) that select for the experimentally observed stripe Q_2. As suggested by Fig. 1.15, the CDW transition to Q_2 has indeed been found to be second order, to be described in Ch.4 of this thesis.

1.2.6 Overview of experimental evidence for CDW

Early experiments on $R\mathrm{Te}_3$ were performed almost entirely within the q_1 regime. The evidence for this CDW and its characteristics are presented here.

This incommensurate modulation was first discovered as superlattice peaks in TEM [12]. A selected area diffraction (SAD) image from my own TEM measurement

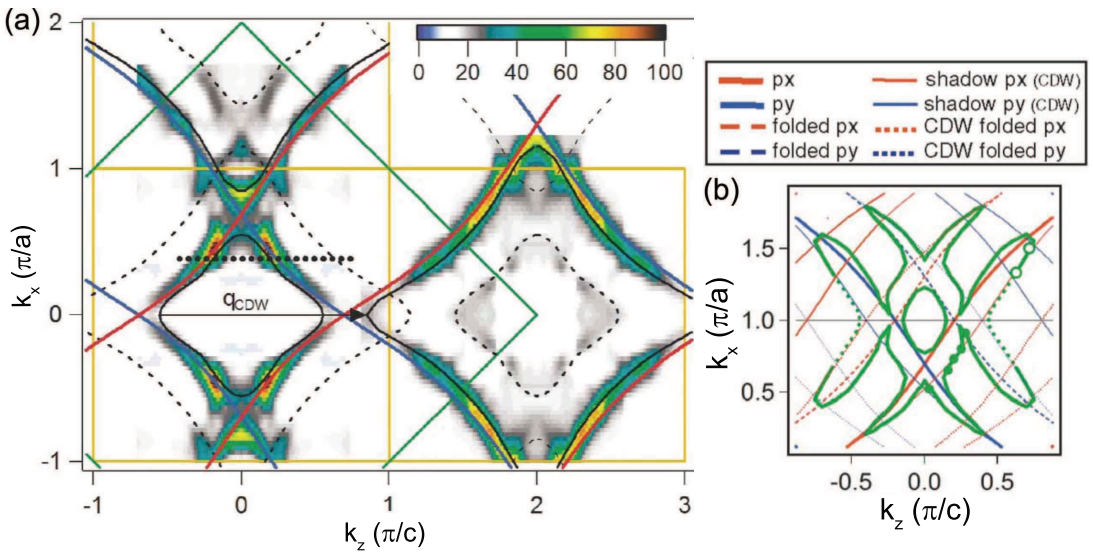

Figure 1.17: (a) ARPES measurement of $CeTe_3$ from Ref.[9]. Ungapped portions of the FS are shown by the intense regions. The 2DBZ is outlined in green and the 3DBZ in yellow. The FS is outlined in black in solid and dashed curves, with the dashed curves representing those obtained from translating by the 3DBZ periodicity. (b)Illustration of reconstructed FS from Ref.[9].

of $ErTe_3$ is shown in Fig. 1.16. (TEM SAD patterns are further described in Ch. 2.) CDW superlattice peaks were subsequently observed across the RTe$_3$ series via x-ray diffraction[15, 16]. The CDW is remarkably robust across the series, showing only slight variances in the absolute value of the nesting vector: from $q_1 = 0.275\ c^*$ for R = La to $q_1 = 0.298$ for R = Dy (room temperature values from [16]). This wavevector corresponds with peaks seen in the susceptibility.

Angle-resolved photoemission (ARPES) experiments [9, 10, 17, 18] show that the FS is partially gapped with this wavevector. Results are presented here for ARPES work performed in collaboration with V. Brouet, Z.-X. Shen, and coworkers[9, 10] Figure 1.17(a) shows a map of the ARPES spectral weight in $CeTe_3$ integrated between E_F and $E_F - 200$ meV[9]. The 2DBZ is drawn in green and the 3DBZ in yellow. The black solid and dashed curves show the FS that is obtained from the tight-binding

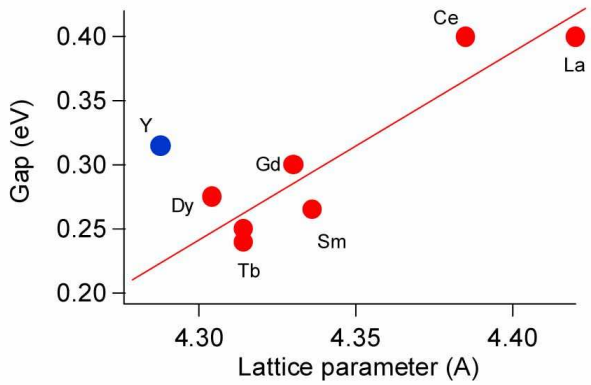

Figure 1.18: ARPES measurements of the maximum gap value for different rare-earths and YTe3, plotted as a function of the lattice parameter c. The straight line is a guide for the eyes. From Ref.[10].

bands and folded over the 3DBZ boundaries. The bright regions indicate the presence of the FS while the absence of intensity along the solid black lines indicates FS gapping. Excepting portions close to the 3DBZ boundaries, ARPES is not sensitive to the dashed translated bands because of weak coupling to the 3D unit cell. Correspondingly, the wavevector is drawn using the $q_1' \approx 5/7\ c^*$ value. Fig. 1.17(b) shows possible outlines of the reconstructed FS as derived from ARPES measurements[9]. This reconstructed FS is further explored via quantum oscillation measurements in Ch. 5.

ARPES measurements for $CeTe_3$ reveal a maximum gap of 400 meV at the Fermi energy for $k_x = 0$ (i.e. the "tips" of the diamond sheets of the FS that are pointing along the c direction. The gap diminishes in magnitude the further one goes around the FS from this point, reaching zero at approximately 0.5 k_x/a[9].

Measurements across the $R\mathrm{Te}_3$ series show that similar regions of the FS are nested for each compound, although the maximum gap is smaller for the compounds with heavier rare earths[10]. The maximum gaps are plotted in Fig.1.18 and range from

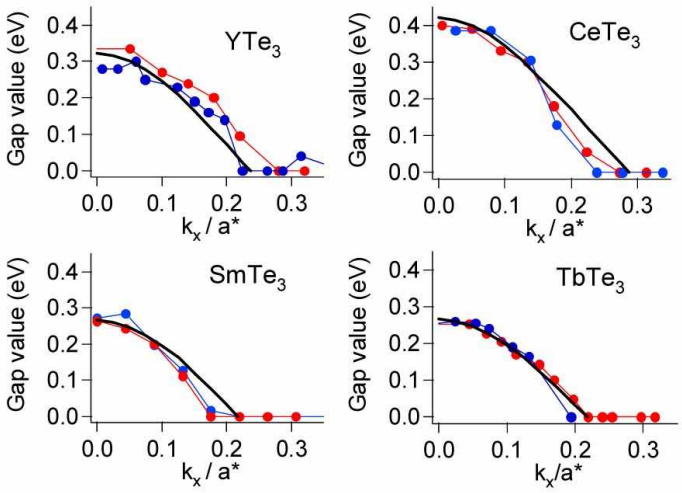

Figure 1.19: The k-dependence of the gap along the Fermi Surface for the square part of FS (red points) and outer part (blue points). k_x is used as implicit parameter for the position on FS. The black line describes the decrease of the gap expected because of the imperfect nesting away from $k_x = 0$. From Ref.[10].

400 meV for $CeTe_3$ to 240 meV for $TbTe_3$. Optical reflectivity measurements also show a similar variation in the gap across the series.[19]

The mean-field transition temperature T_{MF} can be estimated using Eq. 1.10 and the maximum gap values from ARPES. These temperatures range from 1500 K for $TbTe_3$ to 2600 K for $CeTe_3$, and are higher than the melting point of RTe_3. (As can be seen on the Gd-Te phase diagram in Fig. 2.1, $GdTe_3$ melts incongruently at 835°C or 1108 K.) The work presented in Ch. 4 show that the actual transition temperatures are greatly suppressed from the mean-field values.

As shown in Fig. 1.19, the gap diminishes in magnitude the further one goes around the FS from $k_x =$, reaching zero at approximately $k_x = 0.25\ a^*$ for $CeTe_3$. In comparison, for $SmTe_3$, for which the maximum gap is only 280 meV, the gap extends only as far as $k_x = 0.18\ a^*$[10]. The results of this thesis, as discussed in Ch. 4 show that compounds with heavier rare earths and smaller gaps have enough FS remaining

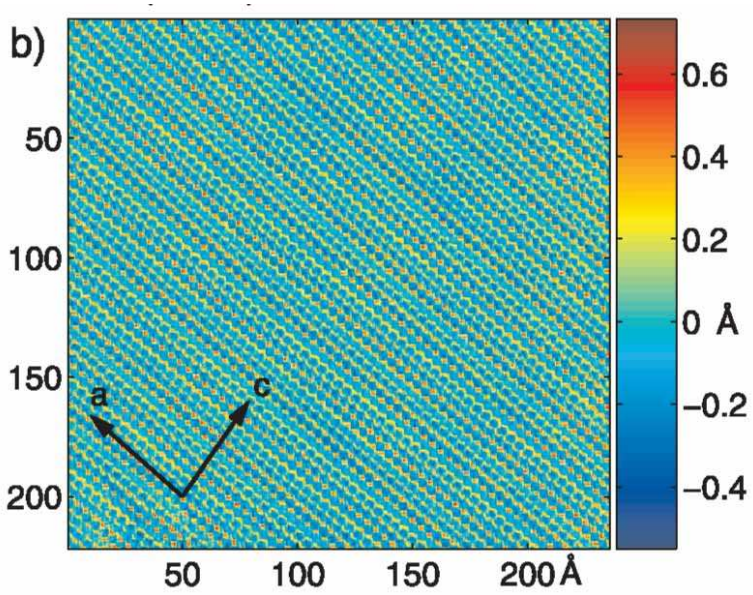

Figure 1.20: STM topography of $TbTe_3$ at T $\approx$ 6 K with voltage bias +200 mV, 50 pA current. From Ref.[20].

that the FS can be nested again by the second wavevector q_2.

The CDW has also been observed in real space by via scanning tunneling microscopy (STM)[20, 21]. Results are presented here for work performed in collaboration with A. Fang and A. H. Kapitulnik[20]. Fig. 1.20 shows an STM topograph for a voltage bias of +200 mV. The CDW can be seen oriented in the c direction. The fourier transform along this direction is shown in Fig. 1.21 for data taken at two different bias voltages. The wavevector $q' = 1 - q \approx 0.71$ is identified as the dominant CDW nesting vector. Other peaks at $q \approx 0.29$, $2q$ and $1 - 2q$, prominent for voltage bias +200 mV but reduced for voltage bias -800 mV, are attributed to mixing between q' and the lattice. An analysis by Fang *et al.* shows that the CDW is fully incommensurate and is free of discommensurations. An additional feature in the fourier transform spectrum was observed at $\approx 5/7c^* + 2/3a^*$. This could mark the appearance of an extraordinary transition present only on the surface, or it could indicate

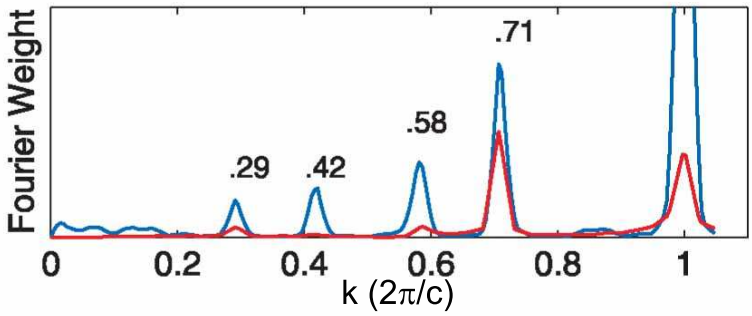

Figure 1.21: Fourier transform of STM topograph of $TbTe_3$(Fig. 1.20) along the c^* direction. Blue: from voltage bias +200 mV topograph. Red: from voltage bias -800 mV topograph. From Ref.[20].

that $TbTe_3$ has a second CDW transition with $T_{c2} > 6$ K, but with accompanying resistivity feature too small to be observed in the datasets presented in Ch. 4.

Transport measurements for R = Y, La - Dy from room temperature and below found metallic resistivity consistent with a Fermi surface that is only partially nested. [22, 23] Measurements for resistivity within the CDW state and an estimate of the density of states for the nested FS are described below in 1.2.7.

1.2.7 Thermodynamic and Transport Measurements

To conclude this introduction to the q_1 CDW state, thermodynamic and transport measurements are presented for $LaTe_3$ and YTe_3. Measurements were performed below the CDW transition temperatures for these compounds. Transport results for $LaTe_3$ show anisotropic resistance with no CDW transitions up to 300 K. Heat capacity measurements for YTe_3 and $LaTe_3$ show small densities of states consistent with a large portion of the FS being gapped by the CDW. These results are published as Ref.[23].

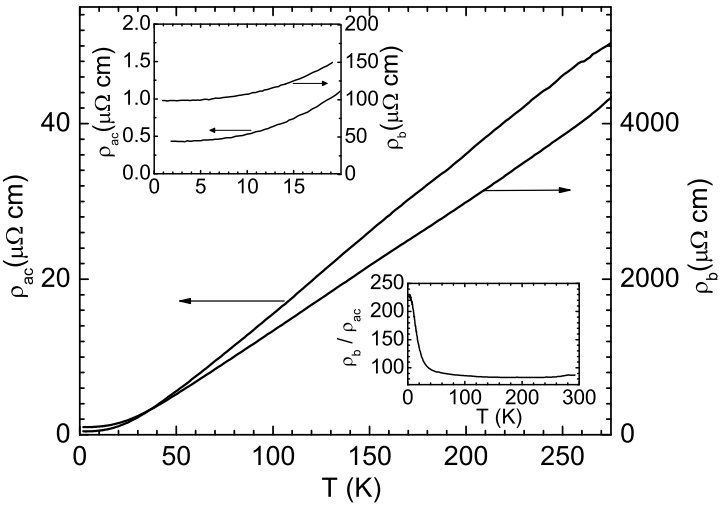

Figure 1.22: Representative resistivity data for $LaTe_3$, for currents flowing in the ac plane (left axis) and along the b-axis (right axis). Insets show (top) residual resistivity and (bottom) temperature dependence of anisotropy ρ_b/ρ_{ac}.

Resistivity of $LaTe_3$

The anisotropic resistivity of $LaTe_3$ is shown in Figure 1.22. The material is clearly metallic, consistent with the presence of significant ungapped portions of the Fermi surface. No electronic transitions are observed up to 300 K. As has been previously noted for $SmTe_3$ [24], the material has a large anisotropy, consistent with the weak b-axis dispersion suggested by band structure calculations [5]. Values of ρ_b / ρ_{ac} (where subscripts refer to the direction in which current is flowing) are approximately 100 above 40 K, rising to over 200 at 1.8 K, a value somewhat smaller than previous estimates by DiMasi and coworkers for $SmTe_3$[24]. The increase in ρ_b / ρ_{ac} presumably reflects increased scattering for currents flowing in the b-axis direction relative to within the Te planes. Given the layered crystal structure, this effect is possibly associated with elastic scattering from stacking faults in the b-axis direction.

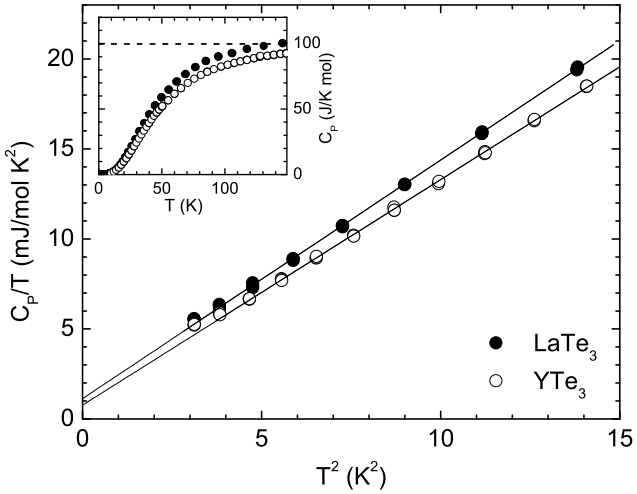

Figure 1.23: Low temperature heat capacity C_p of YTe_3 and $LaTe_3$, shown as C_p/T vs T^2. Straight lines show linear fits as described in the main text. Upper inset shows C_p vs T to 150 K, with the dashed line marking the Dulong-Petit value.

Density of states of YTe_3 and $LaTe_3$

The heat capacity of the nonmagnetic compounds YTe_3 and $LaTe_3$ is measured to provide an estimate of the density of states $n(E_F)$ at the Fermi level within the CDW state. Measuring the nonmagnetic RTe_3 enables an accurate estimate of the low-temperature electronic contribution to the specific heat, with is difficult to do in the presence of the low-temperature ordering seen for the magnetic RTe_3, as described in Ch. 6.

Heat capacity data for the two non-magnetic members of the RTe_3 series (R = Y and La) are shown in Figure 1.23. Linear fits to C_p/T vs. T^2 were performed from 2.1 to 3.7 K for YTe_3 and 1.9 to 3.7 K for $LaTe_3$, avoiding the slight deviation from linearity below 2 K which is presumably associated with a nuclear Schottky anomaly. The resulting estimate for the low-T T^3 coefficient gives Debye temperatures Θ_D of

183.8 ± 0.5 and 180.4 ± 0.5 K for YTe_3 and $LaTe_3$ respectively, and indeed the heat capacity rises to the Dulong-Petit value ($4 \times 3R = 99.7$ J/molK; inset to Fig. 2) for temperatures above approximately 180 K. The small difference in Θ_D is consistent with the different atomic weights of Y and La. The y-intercept of the linear fit gives the electronic contribution to the heat capacity, with $\gamma = 0.8$ and 1.1 ± 0.1 mJ/molK^2 for YTe_3 and $LaTe_3$ respectively. Within a free-electron model, these values correspond to densities of states of 0.33 and 0.48 states/eV/f.u. (or 4.5 and 6.5 states/Ry/f.u.) respectively for the two compounds.

The density of states of YTe_3 and $LaTe_3$ estimated from heat capacity measurements are significantly smaller than values calculated for the unmodulated crystal structure. (0.8 states/eV/f.u. [5, 25]), consistent with the charge density wave gapping a large portion of the FS in these compounds. Small differences in the measured density of states for the two compounds likely reflecting subtle differences in the nesting features of their respective Fermi surfaces. In spite of their small density of states, the RTe_3 compounds remain good metals within the CDW state.

1.3 Outline of Thesis

While the CDW state for the q_1 wavevector had been established for the RTe_3 series at room temperature for most of the compounds, the CDW transition temperatures had not yet been measured. Given the high mean-field transition temperatures estimated from the maximum gap as measured by ARPES[10], it was thought that the transition temperatures might be too high to be easily accessible by experiment. These measurements presented here not only show that the transition temperatures T_{c1} are only slightly higher or even sometimes lower than room temperature for the heaviest

rare-earth compounds, they also show that the transition temperatures vary remarkably across the series for a CDW that is otherwise very similar between compounds. In addition, an entirely new CDW is discovered for the compounds with heaviest rare earths and smallest lattice parameters which nests a FS previously nested by the original CDW wavevector.

Single crystals were grown by a binary flux growth technique that yields large, high quality crystals. Crystal growth and characterization is described in Ch. 2. Methods for thermodynamic, transport and diffraction measurements are described in Ch. 3. Resistivity and high resolution x-ray diffraction results detailing the CDW transition temperatures T_{c1} and T_{c2} and the discovery of the second CDW with wavevector q_2 are presented in Ch. 4. Measurements of de Haas van Alphen(dHvA) oscillations investigating the reconstructed FS for the CDW state of $LaTe_3$ are described in Ch. 5. Transport and thermodynamic measurements focussing on the low-temperature antiferromagnetic order across the $R\mathrm{Te}_3$ series are outlined in Ch. 6. Finally, conclusions for this thesis are presented in Ch. 7. In the appendix, a tutorial is given for how superlattice peaks are observed by diffraction measurements with a simple 1D model presented, and a short introduction is given for dHvA.

Chapter 2

Crystal Growth and Characterization

2.1 Crystal Growth

Single crystals were grown in an excess of tellurium via a self flux technique. An advantage of using this self-flux technique, over the previously reported alkali halide flux technique[24], is that it does not introduce other elements to the melt. Figure 2.1 shows the phase diagram of Gadolinium-Tellurium, with the arrow indicating the path of the growth. Elements in the molar ratio $R_x\mathrm{Te}_{1-x}$, $x = 0.015 - 0.030$, were put into alumina crucibles and vacuum sealed in quartz tubes, as pictured in Fig. 2.2. The mixtures were heated to 800-900°C and slowly cooled over a period of 4 days to end temperatures in the range of 500-700°C. The remaining melt was decanted in a centrifuge. Small spots of tellurium flux remaining on the crystal, more of a problem for growths decanted near 500°C, can be removed with a scalpel.

Resulting crystals were malleable, micaceous plates with dimensions of up to 8

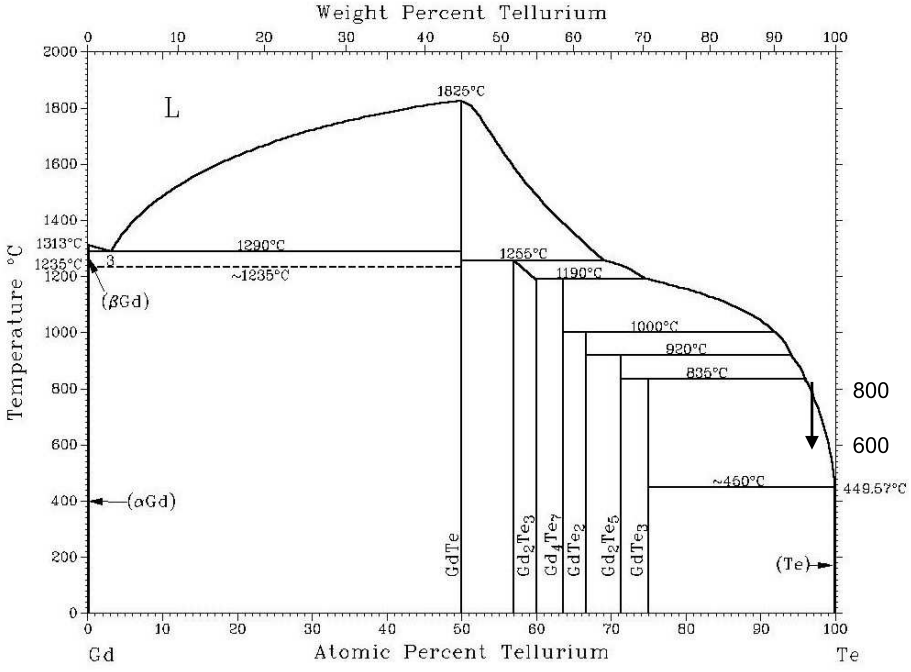

Figure 2.1: Binary phase diagram for Gd-Te.[26] Arrow indicates path of growth.

$\times$ 0.4 $\times$ 8 mm, and oriented with the long b-axis perpendicular to the plane of the crystal plates. A representative crystal is shown in Fig. 2.3. The color of the crystals vary subtly across the series, from the light gold of $LaTe_3$ and $CeTe_3$ to the darker tone of the heavier rare earth compounds. The material is somewhat air-sensitive, and crystals must be stored in an oxygen and moisture-free environment. The heaviest rare earth compounds, $ErTe_3$ and $TmTe_3$ are the most sensitive and an hour's exposure to air will subtly darken the surface of the crystals. On further exposure to air, $R\mathrm{Te}_3$ oxidizes to a dull gray color.

Unlike the related compounds $R\mathrm{Te}_2$ and $R_2\mathrm{Te}_5$, $R\mathrm{Te}_3$ is a soft crystal and care must be taken during handling to prevent accidental deformation of the crystal. The crystals cleave easily under a light touch from a scalpel, but cutting the plate-like crystals in the perpendicular direction will often result in edges that are smeared

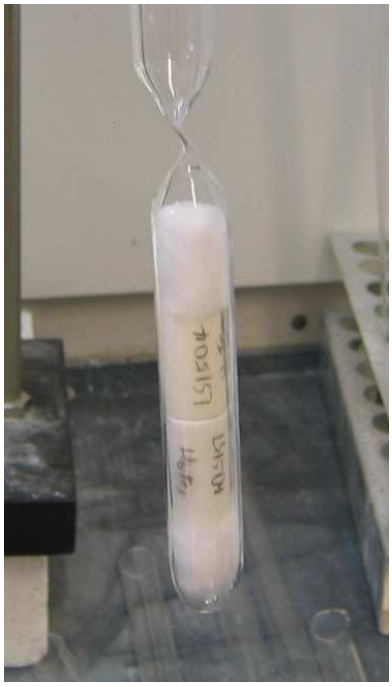

Figure 2.2: Starting materials are placed in alumna crucibles and sealed in an evacuated quartz tube. Here, a partially sealed growth is being evacuated. Quartz wool is placed on either end of the alumina crucibles to protect the growth from impact during the decanting process.

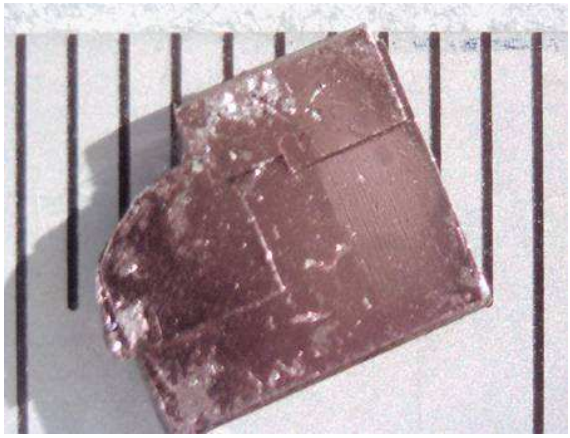

Figure 2.3: Single crystal of $GdTe_3$ shown over a mm scale. The b axis is out of the page.

from the pressure of the scalpel. As a result, an as-grown crystal is usually of higher quality than a sample that has been excised from a larger piece of material.

Residual resistance ratios (RRR, or "Triple R") are a measure of the disorder present in metallic compounds, and is defined as the room temperature resistivity divided by that at a 1.8 K. The RRRs for $R\mathrm{Te}_3$ vary amongst the series, being up to 120 for $LaTe_3$ and lower ($\sim$40) for heavier rare earth compounds such as $TbTe_3$.

2.2 X-ray Diffraction

$R\mathrm{Te}_3$ is prone to twinning within the plane of the Te sheets due to the weak van der Waals bonds between the Te bilayers. High resolution x-ray measurements show that a seemingly single crystal will often be composed of several domains rotated within the plane by fractions of a degree, and will also have domains that are rotated 90° from each other. A high resolution x-ray beam can be aligned onto a single domain, but care must be taken in the interpretation of other bulk measurements, such a resistivity, in that the orientation along the a and c axes of a particular sample

cannot be precisely determined.

Crystals were characterized using a Panalytical X'Pert Pro Diffractometer in both the Mirror + Parallel Plate Collimator (PPC) and the Hybrid + RC Triple configurations. As the penetration depth is very small - on the order of microns - this measurement is very sensitive to the composition near the surface of the crystals. The quality of the bulk crystal can sometimes be inferred from this measurement.

Fig. 2.4 shows rocking curve (omega) scans for a few samples. Fig. 2.4(a) and (b) are the $TbTe_3$ crystals that were respectively used for the room temperature and high temperature studies at SSRL, as described in a later chapter. The X'Pert rocking curves for these samples show well-formed peaks, and indeed, these crystals proved to be very suitable for high-resolution x-ray measurements. In contrast, Fig. 2.4(c) shows the crystal of $LaTe_3$ that was used for PPMS torque measurements, as described in Ch.4. This is a sample that has been extensively handled and cut to fit onto the torque platform. However, Fig. 2.4(d) shows a relatively clean rocking curve for an $ErTe_3$ sample that was later found in the high-resolution x-ray studies to be far inferior to the $TbTe_3$ samples. Data showing the second superlattice modulation with wavevector q_2, as described in Ch.3, was obtained with this sample,.

2.3 Transmission Electron Microscopy

Transmission electron microscopy (TEM) served as a characterization tool. Selected area diffraction (SAD) patterns were taken for samples oriented along [010]. TEM experimental methods are described in 3.5.

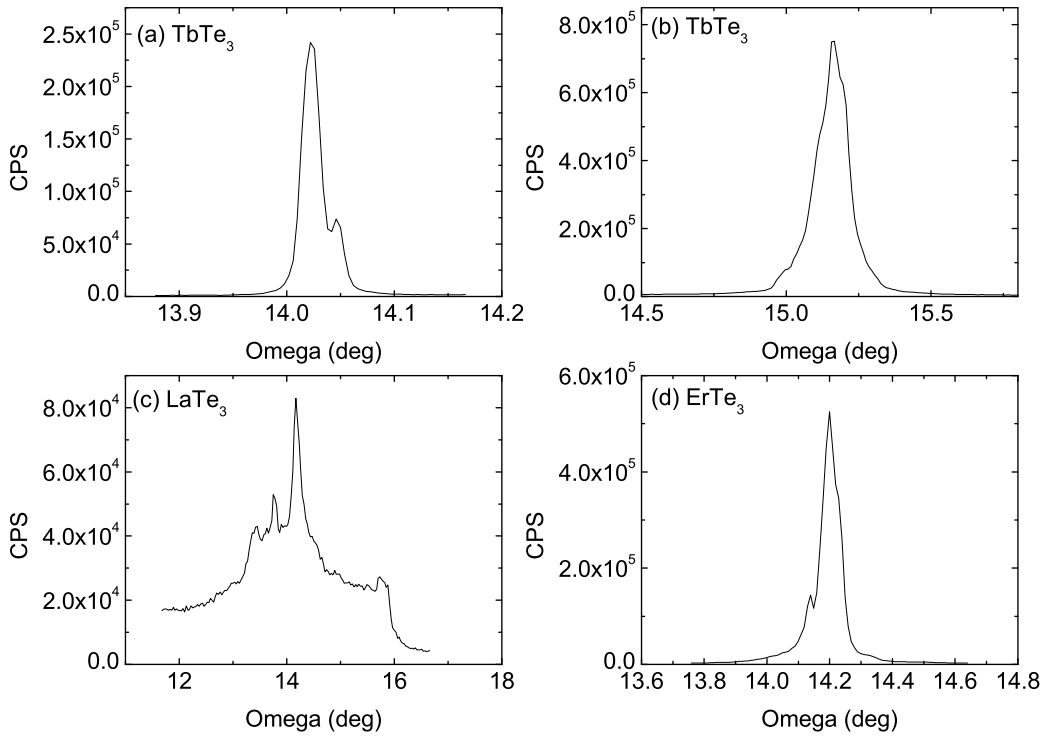

Figure 2.4: Rocking curves as measured on the X'Pert. (a)LS999 $TbTe_3$, 26.9 mg, Mirror + PPC. This sample was used for room-temperature diffraction studies at SSRL. (b)LS1280A $TbTe_3$, 54.2 mg, Hybrid + RC Triple. This sample was used for high-temperature diffraction studies at SSRL. (c)$LaTe_3$ crystal that was used for angle-dependent torque-measurements in the PPMS as described in Ch. 4. (d) $ErTe_3$ 1592A used for SSRL diffraction studies in June 2007.

2.3.1 $TbTe_3$

$TbTe_3$ has a CDW transition temperature of $T_c = 336(3)$ K as observed from resistivity. The CDW superlattice in $TbTe_3$ is very clearly visible at room temperature, as shown in Fig. 2.5. With the beam parallel to the b-axis, the SAD images the section of reciprocal space for K = 0. For the RTe$_3$ $Cmcm$ space group, when K = 0 the allowed reflections are for H = even and L = even. Fig. 2.5 shows a section of from (5 0 -5) to (5 0 5). The labeled reflections, with both H and L odd, are technically allowed and can be attributed to sample bending[12]. Nevertheless, CDW superlattice reflections can be observed on either side of these main reflections.

CDW superlattice reflections (5 0 -3+5/7) and (5 0 -1-5/7) are indicated by the arrows. The distance between each CDW reflection and the nearest allowed average lattice reflection is c^*-$q \approx 5/7\ c^*$. For $TbTe_3$ at room temperature, CDW superlattice reflections near the zone axis were so weak to be invisible, and appeared with increasing intensity with increasing distance from the origin. This attribute of superlattice peaks is described in the Appendix.

TEM measurements were performed with samples mounted in a heating probe. As samples were heated above room temperature, thermal expansion caused the sample position to shift considerably and refocussing was needed at each new temperature. An effort was made to refocus on the same portion of the sample at each temperature. TEM temperatures were read from the thermocouple located on the sample probe.

In a particular $TbTe_3$ sample, upon heating superlattice peaks decreased in intensity until only a few were visible at 60°C (333 K), and none visible at 73°C (346 K). On cooling, a few superlattice spots reappeared again at 61°C (334 K), with the full superlattice returning at room temperature. This is consistent with the value of T_c = 336(3) K from resistivity.

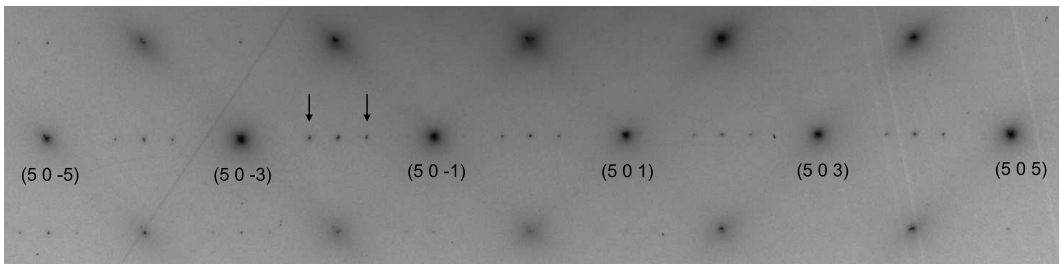

Figure 2.5: Selected area diffraction pattern for $TbTe_3$ along [010] at room temperature. Spots from average structure indicated by large arrows. CDW peaks indicated by small arrows.

In some cases, an unusual pattern was observed at high temperatures. An example is shown in Fig. 2.6. Most likely this is due to some sample oxidation or other undesirable reaction occurring at high temperatures. This effect was not seen in high-resolution x-ray diffraction measurements at SSRL. On cooling to room temperature, the unusual pattern coexisted with the CDW superlattice, with the unusual pattern strongest near the zone axis (as shown in the figure), and the CDW superlattice more visible in high-order zones.

2.3.2 $ErTe_3$

$ErTe_3$ undergoes two CDW transitions T_{c1} at 267(3) K and T_{c2} at 159(4) K. As they are both below room temperature, a cooling probe was needed to observe superlattice peaks.

On filling the cooling probe with liquid nitrogen, the sample temperature decreased very rapidly, reaching base temperature of -160 to -169 C (104 to 113 K) within half an hour. After letting the temperature stabilize, the heater was turned on and SAD images were taken as the temperature swept upwards, over the course of an hour. Images were taken as quickly as possible. As the sample shifts with temperature, the focus needed to be adjusted with each image. An effort was made

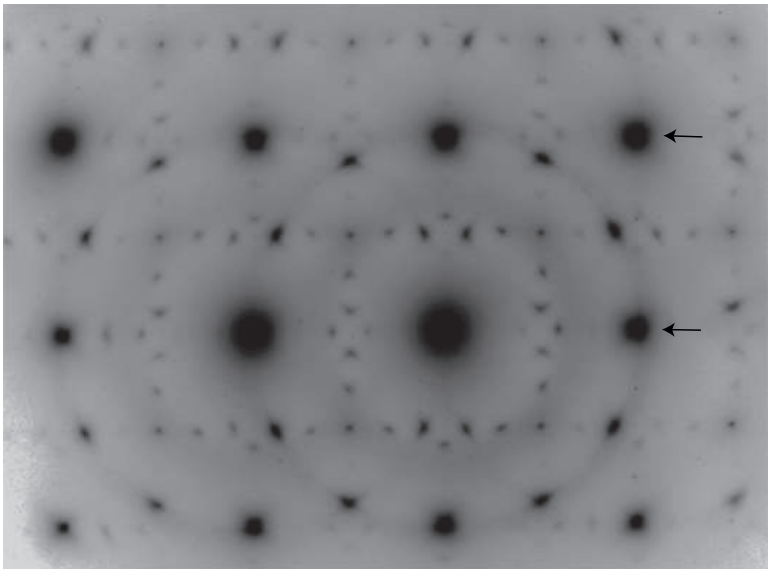

Figure 2.6: Unusual SAD pattern along [010] observed for some crystals of $TbTe_3$ at 427 K. The zone axis is the large spot just to the left of middle. To indicate orientation and scale, arrows are drawn for two average lattice reflections that are separated by $2c^*$

to focus on the same part of the sample.

The superlattice with wavevector q_1 was observed below T_{c1}. This superlattice was found to increase in intensity as temperature was further decreased below T_{c1}. No observable change in the superlattice was observed on crossing below T_{c2}. The q_2 superlattice was too faint to be observed via TEM, but has been identified using high resolution x-ray diffraction as described in Ch. 4.

For a particular sample, on cooling the superlattice was first seen at -47°C (226 K). On heating, with more stable temperature control, superlattice peaks were seen up to -13°C (260 K). The superlattice of $ErTe_3$ at the base temperature of -155 C (118 K) is shown in Ch. 1.

Chapter 3

Experimental Methods

A variety of experimental techniques were used to probe the CDW formation in the $R\mathrm{Te}_3$ family of compounds. These techniques are briefly outlined here.

3.1 Resistivity measurements

Electrical resistivity measurements provided the first evidence for CDW formation in the $R\mathrm{Te}_3$ family of compounds, and were used to obtain T_c values across the rare earth series. These measurements also revealed the large electrical anisotropy associated with the quasi-2D Fermi surface as described in 1.2.3.

The electrical resistivity was measured using geometric bars cut and cleaved from the larger as-grown crystals. In-plane measurements were made for arbitrary current directions in the *ac* plane, using a standard 4 point contact geometry. The *b*-axis resistivity was measured using a modified Montgomery geometry [27], with one current and one voltage contact on the top face of the plate-like crystal, and the other voltage and current contacts on the bottom face. For the crystals that were used for *b*-axis

resistivity measurements, the equivalent isotropic crystals [27] had typical aspect ratios of approximately one-to-one, implying that estimates of the b-axis resistivity are meaningful.

Initial measurements were made with platinum wires (50 μm diameter) attached directly onto the sample surface using Dupont 4929 silver paint with n-Butyl acetate added as a thinner. This silver paint is a one-component epoxy that cures quickly at room-temperature. Since $R\mathrm{Te}_3$ oxidizes in air, epoxies that require heat-curing are not recommended. Typical contact resistances of 10-15 Ω were obtained, although contact quality degraded with time. Multi-day measurements usually experienced some contact degradation.

In subsequent experiments, gold pads were either evaporated or sputtered onto the crystal surface, and platinum wires were attached to the gold pads with silver paint. With the gold pads, contact resistances improved to 2-3 Ω. Additionally, contacts with gold pads were more stable with time, showing little change with the passage of days or weeks as long as the sample was kept in an oxygen-free environment.

For heating above room temperature, the contacts showed an annealing or "settling" behavior such that the first pass from room temperature to, say, 400 K would result in uneven data, but results from second and third passes would be stable and reproducible.

Temperature control was provided by either a Quantum Design MPMS SQUID magnetometer, or a Janis flow cryostat. In the MPMS, the temperature range is 1.8 to 400 K with the sample immersed in a helium atmosphere. The flow cryostat allowed a temperature range of 1.6 to 450 K. (The Janis flow cryostat itself has a maximum temperature of 475 K, but the use of particular solders for sample mounting limited the temperature to 450 K). The sample is immersed in a helium atmosphere for

below room temperature measurements, and in vacuum for above room temperature measurements. In either system, the resistance was measured using either an LR-700 AC resistance bridge operating at 16 Hz, or a Lakeshore 370 AC resistance bridge operating at 13.7 Hz.

3.2 Magnetization measurements

Magnetization measurements served to characterize the long range order associated with rare earth ions, and to probe the effects of the CDW transition on the susceptibility (Ch. 6). Quantum oscillations were also observed in magnetization; these measurements are described separately in 3.3.

Magnetization measurements were made using a commercial (Quantum Design MPMS) SQUID magnetometer. Samples were mounted on polymer disks that were machined to fit inside a plastic drinking straw, which was then mounted on the end of the sample probe. Samples were secured to the disk and straw with Duco Cement, a polymer-based glue by Devcon. The susceptibility of the sample is obtained by subtracting the background susceptibility (disk and glue) from that of total measured susceptibility. For the magnetic rare earth compounds, the background susceptibility is small compared to that of the sample. For a few measurements, particularly for the nonmagnetic compounds (R = Y, La), the disc was omitted and the sample was mounted in between two straws to minimize the background susceptibility

Applied fields of 1000 and 5000 Oe were used to measure the temperature dependence of the low field d.c. susceptibility (M/H). Temperatures from 1.8 to 400 K could be reached with the MPMS, although for most measurements a temperature range of 1.8 to 300 K was used. Data were taken for fields oriented along the b-axis

(i.e. perpendicular to the plane of the crystal) and for an arbitrary direction in the *ac* plane (i.e. in the plane of the Te sheets). The polycrystalline average $\chi_{poly} = (\chi_b + 2\chi_{ac})/3$ was calculated for each sample.

Magnetization (M) was measured at the base temperature of 1.8 K for fields from 0 to 5 T.

3.3 De Haas van Alphen oscillations

De Haas van Alphen oscillations were observed for the non-magnetic YTe_3 and $LaTe_3$ as described in Ch. 5. Preliminary measurements were made using the Quantum Design MPMS as described in 3.2. Subsequent measurements were made either by measuring susceptibility in a dilution refrigerator, or by measuring torque in a Quantum Design PPMS.

3.3.1 Susceptibility in dilution refrigerator

The magnetic susceptibility for de Haas van Alphen experiments was measured at the University of St. Andrews (UK) in an Oxford Instruments dilution refrigerator at a base temperature of 10 mK and in fields up to 15 T. AC susceptibility measurements were made using a susceptometer consisting of two counterwound secondary coils inside a primary coil. The sample was inserted in one of the secondary coils, held in place with grease, and thermally grounded with gold wires.

A typical measurement at base temperature consisted of a magnetic field sweep from 15 T to 0.5 T at a rate of 0.025 T/min, with a data density of one point per 0.6 Oe.

3.3.2 Torque magnetometry

Torque measurements were made in a 14 T Quantum Design Physical Properties Measurement System (PPMS). Crystals were shaped to square platelets weighing 1-2 mg and attached to the PPMS cantilever chip using a small amount of grease. The torque chip is mounted on a platform that allows rotation along an axis perpendicular to the field. At zero angle, the $R\mathrm{Te}_3$ sample is positioned such that the magnetic field is parallel to the b-axis of the crystal.

The nominal range of rotation is from -10° to 375°. However, one turn on the dial is not precisely 360°. From correlating experimental data, the nominal angle of 365° was found to be closer to 360°. When angles in the range of -45° to 0° were desired, data was taken in the range of 320° to 365°, incorporating the known 5° offset.

For a typical de Haas van Alphen measurement, the temperature was set to the base temperature—1.9K or 2.0 K, and the magnetic field was swept from 14T to 2 T at a rate of 0.063 T/min with a data density of one point per 75 Oe, which was the slowest possible rate for the PPMS.

3.4 Heat Capacity

Specific heat measurements were used to probe the magnetic ordering of the rare earth ions (Ch. 6), and to arrive at estimates of the density of states (1.2.7).

The heat capacity of the single crystal samples was measured using a relaxation time technique in a 9 T Quantum Design Physical Property Measurement System (PPMS). Crystals with a mass of approximately 10 mg and flat surfaces were selected for good thermal contact with the sample platform. Data were taken in zero applied field from 1.8 to 300 K.

3.5 Transmission electron microscopy

Transmission electron microscopy (TEM) served as a characterization tool with results presented in 2.3. Since heating and cooling sample probes were available, temperature dependent measurements could be made through the CDW transition temperatures. These measurements served as a guideline for later high-resolution x-ray diffraction measurements.

Thin slices of crystal were cleaved with a scalpel and mounted on copper grids and ion milled. Selected area diffraction (SAD) patterns were taken with the beam parallel to the b-axis. The crystals were illuminated on the edge of the hole and SADs were obtained using a Philips CM20 FEG-TEM operating at 200 kV. Temperature control was provided by a heating probe and a cooling probe. The cooling probe contains a well to hold liquid nitrogen, as well as a heater and thermocouple.

3.6 High resolution x-ray diffraction

High resolution x-ray diffraction was performed on single crystals to measure the superstructure arising from the CDW, as presented in Section 4.2. Superlattice measurements following the order parameter of the q_1 CDW confirmed that the features observed in resistivity measurements at T_{c1} were indeed CDW transition temperatures. Measurements of $ErTe_3$ observed the second CDW wavevector T_{c1}.

These measurements were performed at the Stanford Synchrotron Radiation Laboratory (SSRL) on Beamlines 7-2 and 11-3. Data were collected in reflection geometry using x-ray energies of 9 to 13 keV. Either 1 or 2 milliradian slits or a Ge(111) crystal analyzer were used to define the diffracted beam. A Kappa goniometer was used in BL11-3 while a four-circle goniometer was used for BL7-2.

Crystals were pre-selected using X'Pert characterization as described in Section 2.2. For room temperature measurements, crystals were mounted with epoxy onto a glass slide, which was in turn mounted with epoxy onto the sample stage. Samples were kept in a flow of He gas to prevent oxidation.

The sample was positioned so that the center of the beam avoided the edges of the sample was much as possible, as the edges were more likely to be inhomogeneous. Care was taken that crystals were mounted flat on the sample stage with the b-axis vertical and parallel to the ϕ axis of rotation. For some measurements, a laser was used to make this alignment. Such a careful alignment made it much easier to orient the crystal in reciprocal space.

For heating and cooling measurements, the sample was mounted onto a thin square of aluminum using "Leitsilber" 200 silver paint from Ted Pella. The sample was placed in an Anton-Paar furnace for measurements above room temperature and kept in a flow of helium gas to prevent oxidation.

For cooling experiments, an ARS displex refrigerator was used at BL7-2, with the sample under vacuum. The hose connections between the sample stage and the refrigerator restricted access to ϕ angles to one or two quadrants of reciprocal space. Changing temperatures caused the sample stage to contract and expand, and as the refrigerator sample stage did not have motorized xyz positioning, it difficult to keep the sample centered in the beam. As a result, uncertainties in absolute values of both the CDW wavevector and superlattice peak intensities were larger for experiments performed in the displex refrigerator.

Chapter 4

CDW Transitions in $R\mathrm{Te}_3$

In this chapter, results of experiments probing the CDW transition in $R\mathrm{Te}_3$ are described, together with an analysis of the effect of chemical pressure on T_c and the symmetry of the CDW state. These results appear in Ref.[28].

Resistivity measurements are presented that show signatures of CDW transitions for R = Sm - Tm, with transition temperatures T_{c1} that vary monotonically across the series. Measurements for the smaller lattice parameter compounds R = Dy - Tm show an unexpected second CDW feature at temperature T_{c2} lower than that of T_{c1}. High-resolution x-ray diffraction for TbTe_3 and ErTe_3 show that T_{c1} is indeed the CDW transition temperature for the CDW with wavevector $q_1 \approx 2/7\ c^*$. For ErTe_3, the lower transition temperature was found to be that of a second CDW lying in the in-plane direction perpendicular to the first with wavevector $q_2 \approx 1/3\ a^*$.

The large variation of T_{c1} across the series and the appearance of the second CDW are shown to be intimately linked to the variation of the density of states across the series, values for which are calculated by collaborators J. Laverock and S. B. Dugdale.

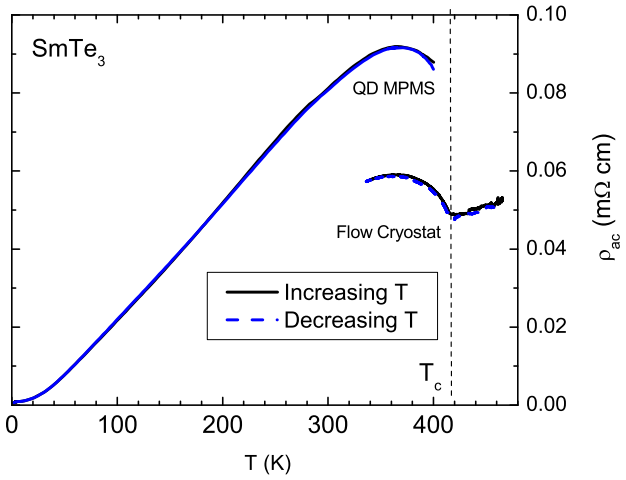

Figure 4.1: Temperature dependence of the resistivity of $SmTe_3$. Data are shown for currents oriented along an arbitrary in-plane orientation. Data was taken on two different apparatus to cover the entire temperature range. Different crystals were used for each measurement. Both warming (solid lines) and cooling (dashed lines) cycles are shown. T_c is marked by a vertical line.

4.1 Signature of CDW transition in resistivity

Representative resistivity data for $SmTe_3$ is shown in Fig. 4.1, and that for $GdTe_3$ and $TbTe_3$ are shown in Fig. 4.2(a) and (b), respectively. For $SmTe_3$, the Quantum Design MPMS was used for temperatures between 1.8 K and its maximum temperature 400 K, while the Janis flow cryostat was used for temperatures from 300 to 450 K. Different samples were used for each measurement. The compounds $GdTe_3$ and $TbTe_3$ were measured in the MPMS, and absolute values of the resistivity have been normalized to the average of several measurements of different samples. As has been previously observed for this family of compounds, the resistivity is strongly anisotropic[23, 24]. For $GdTe_3$ and $TbTe_3$ compounds, a clear feature can be seen for both current orientations, with an onset at $T_c = 377(3)$ for $GdTe_3$ and 336(3) K for

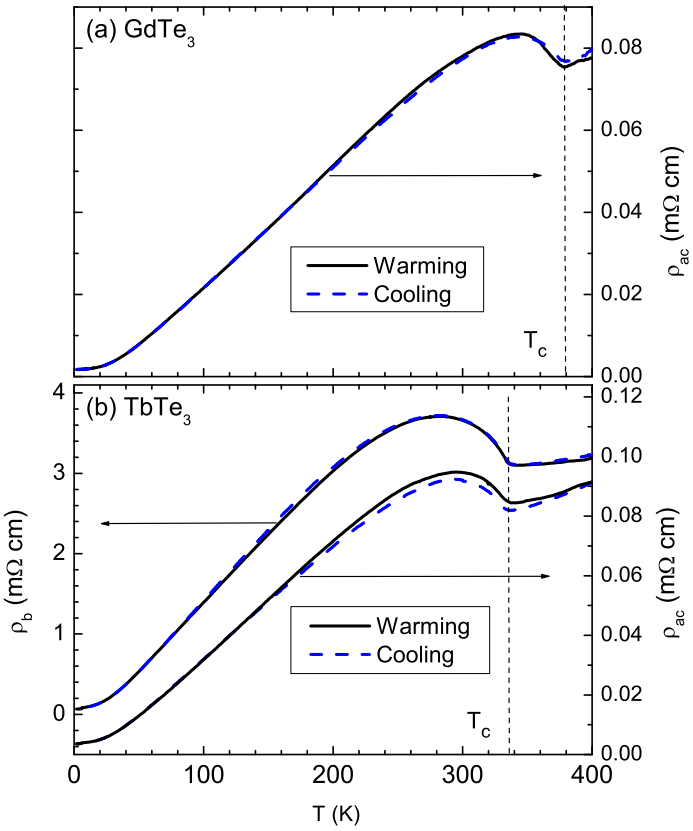

Figure 4.2: Temperature dependence of the resistivity of GdTe$_3$(a) and TbTe$_3$(b). Data are shown for currents oriented along the b-axis (ρ_b, left axis) and arbitrary in-plane orientations (ρ_{ac}, right axis). Vertical axes are offset for clarity. Both warming (solid lines) and cooling (dashed lines) cycles are shown. T_c is marked by a vertical line.

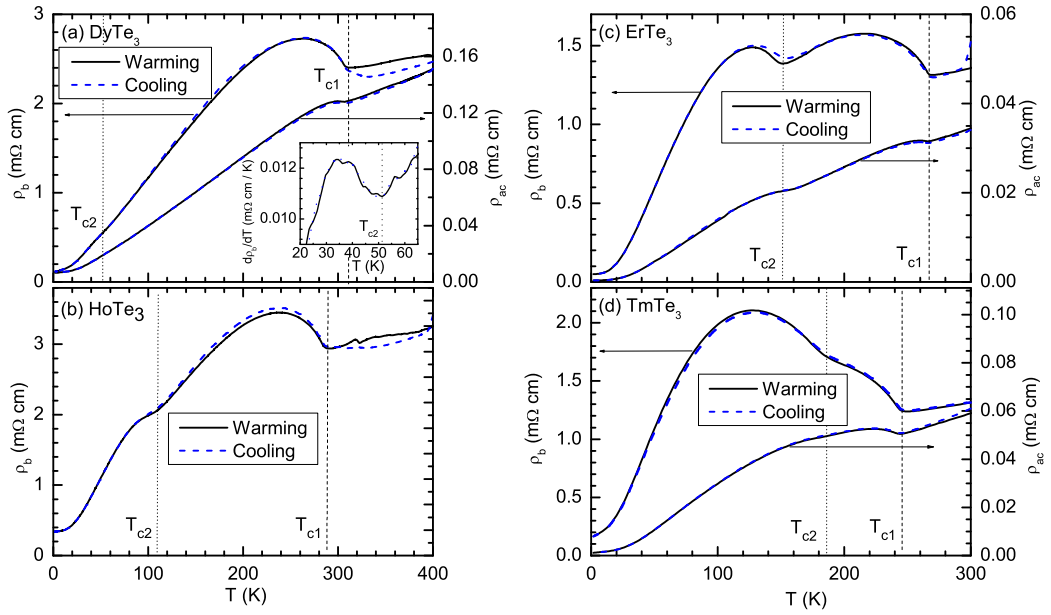

Figure 4.3: Temperature dependence of the resistivity of (a) $DyTe_3$ (Inset: dρ/dT), (b) $HoTe_3$, (c) $ErTe_3$ and (d) $TmTe_3$. Data are shown for currents oriented along the b-axis (ρ_b, left axis) and arbitrary in-plane orientations (ρ_{ac}, right axis). Both warming (solid lines) and cooling (dashed lines) cycles are shown. Both CDW transitions are marked for each compound.

$TbTe_3$. There is no hysteresis between warming and cooling cycles. For $SmTe_3$, despite the use of two different samples with different geometries, a similar feature can be seen with $T_c = 416(3)$ K. As described in the next section, x-ray diffraction measurements show that this feature marks the CDW transition for $TbTe_3$. Excepting the loss of spin-disorder scattering at $T_N = 3$ K for $SmTe_3$ and $T_N = 5.6$ K for $TbTe_3$, further discussed in Ch. 6, no other features were observed in either the resistivity or its derivative, suggesting that there are no additional CDW phase transitions below T_c for either compound.

The resistivity for the heavier members of the series (R = Dy, Ho, Er, and Tm) was

measured in the MPMS and are shown in Fig. 4.3 (a) - (d). These are qualitatively different than those of the lighter rare earths, showing two transitions at T_{c1} and T_{c2}. Again, data are shown for both heating and cooling cycles, as well as for in-plane and b-axis orientations. Looking at the b-axis data - for which the current direction is better defined - the feature at T_{c2} is largest for the heaviest member of the series, TmTe$_3$. This feature then decreases in both magnitude and temperature for the lighter rare earths, vanishing for compounds lighter than DyTe$_3$.[1] The derivative dρ/dT for DyTe$_3$ is shown in the inset to Fig. 4.3(a) to highlight the feature at T_{c2}. In the next section we identify for ErTe$_3$ that T_{c2} marks the onset of a CDW with wavevector perpendicular to the first. Subsequent measurements by C. L. Condron and J. H. Chu have confirmed a similar second CDW wavevector for HoTe$_3$[29].

Figure 4.4 shows representative data for YTe$_3$ as measured in the MPMS. It shows a clear transition at 334(3) K which is very similar to that of TbTe$_3$. The small downturn at 400 K is assumed to be an experimental artifact, although a second CDW transition at 400 K cannot be ruled out based on these data.

The CDW transition temperatures are summarized in Table 4.1, and in Figure 4.5 they are plotted as a function of the in-plane a-axis lattice parameter,[2] which provides a measure of the chemical pressure. The first transition temperature T_{c1} ranges from a low of 244(3) K for TmTe$_3$, the compound with the smallest lattice parameter in the series, and increases monotonically with increasing lattice parameter (decreasing chemical pressure). In contrast, the second transition temperature T_{c2} shows the

[1] While a second lower transition was not observed in the resistivity for TbTe$_3$, STM measurements on TbTe$_3$ at 6K[20]show an ordering with wavevector $\sim 2/3\ a^*$ which is similar to q_2' a observed by x-ray diffraction in ErTe$_3$ below T_{c2}. This could mark the appearance of an extraordinary transition present only on the surface, or it could indicate that TbTe$_3$ does in fact have a second transition with $T_{c2} > 6$ K, but with accompanying resistivity feature too small to be observed

[2] The lattice parameters for GdTe$_3$, TbTe$_3$, and DyTe$_3$ were obtained at SSRL BL11-3 by x-ray diffraction on single crystals. Lattice parameters for SmTe$_3$ from DiMasi *et al*[24]. Lattice parameters for HoTe$_3$, ErTe$_3$, TmTe$_3$ from Ref. [30].

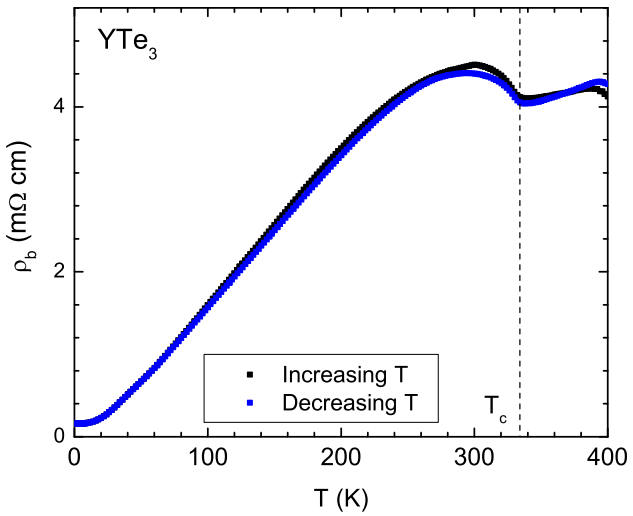

Figure 4.4: Temperature dependence of the resistivity of YTe$_3$. Data are shown for currents oriented along the b-axis. Both warming (solid lines) and cooling (dashed lines) cycles are shown. T_c is marked by a vertical line.

RTe$_3$	$T_{c1}(K)$	$T_{c2}(K)$
YTe$_3$	334(3)	–
SmTe$_3$	416(3)	–
GdTe$_3$	377(3)	–
TbTe$_3$	336(3)	–
DyTe$_3$	306(3)	49(5)
HoTe$_3$	284(4)	126(6)
ErTe$_3$	267(3)	159(5)
TmTe$_3$	244(3)	186(5)

Table 4.1: The CDW transition temperatures T_{c1} and T_{c2}. Based on the trend in T_{c1} with chemical pressures, values for T_{c1} are anticipate to be greater than 450 K for R = La, Ce, Pr, Nd.

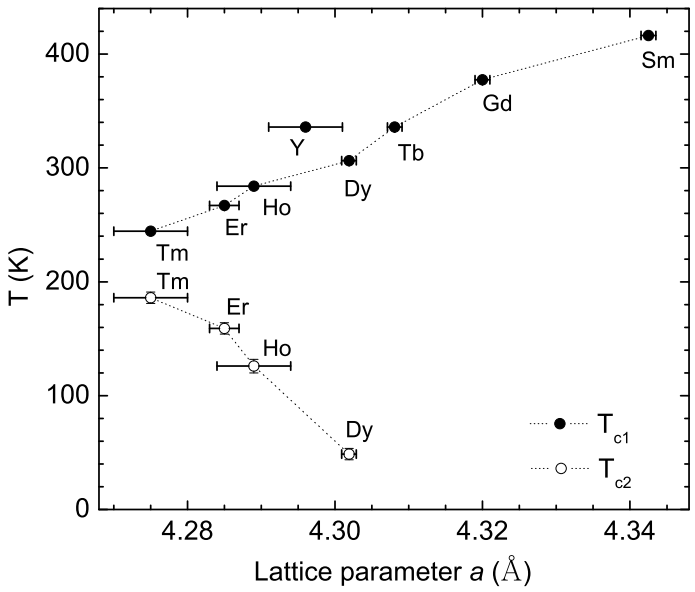

Figure 4.5: T_{c1} and T_{c2}, as obtained from resistivity measurements, plotted as a function of in-plane lattice parameter a at 300 K for several compounds in the RTe$_3$ series (labeled). Note that the lattice parameter is smaller for the heavier members of the RTe$_3$ series. Dashed lines are drawn between points to guide the eye. (The lattice parameters for GdTe$_3$, TbTe$_3$, and DyTe$_3$ were obtained at SSRL BL11-3 by x-ray diffraction on single crystals. Lattice parameters for SmTe$_3$ from DiMasi *et al*[24]. Lattice parameters for HoTe$_3$, ErTe$_3$, TmTe$_3$ from Ref. [30].)

RTe$_3$	a (Å)	b (Å)	c (Å)	q (c^*)
LaTe$_3$	4.4056(10)	26.267(10)	4.4210(10)	0.2710(4)
GdTe$_3$	4.3200(10)	25.570(10)	4.3302(10)	0.2920(4)
TbTe$_3$	4.3081(10)	25.470(10)	4.3136(10)	0.2960(4)
DyTe$_3$	4.3019(10)	25.405(10)	4.3043(10)	0.2990(4)

Table 4.2: Lattice parameters and q_1 measured at room temperature at SSRL BL11-3.

opposite trend, *decreasing* as the lattice parameter increases, eventually vanishing for compounds lighter than DyTe$_3$. [3] Following the trend for T_{c1} transition temperatures for the lightest members of the series, LaTe$_3$, CeTe$_3$, NdTe$_3$, and PrTe$_3$, are presumed to have CDW transition temperatures greater than 450 K. (No CDW transitions were seen in the resistivity for NdTe$_3$ up to 450 K, and none for LaTe$_3$ or CeTe$_3$ up to 300 K.)

4.2 High resolution x-ray diffraction

High-resolution x-ray diffraction measurements were performed on single crystals of LaTe$_3$, GdTe$_3$, TbTe$_3$, DyTe$_3$, and ErTe$_3$ at Stanford Synchrotron Radiation Laboratory (SSRL). Lattice parameters and values for the q_1 CDW are shown in Table 4.2[4]

Results of detailed studies TbTe$_3$ and ErTe$_3$, examples of RTe$_3$ with one transition and two transitions, respectively, are reported here.

[3] While a second lower transition was not observed in the resistivity for TbTe$_3$, STM measurements on TbTe$_3$ at 6K [20] show an ordering with wavector $\sim 2/3\ a^*$ which is similar to q_2' a observed by x-ray diffraction in ErTe$_3$ below T_{c2}. This could mark the appearance of an extraordinary transition present only on the surface, or it could indicate that TbTe$_3$ does in fact have a second transition with $T_{c2} > 6$ K, but with accompanying resistivity feature too small to be observed.

[4] Lattice parameters reported by Malliakas *et al.*[16] were found to be consistently larger than those reported in Ref. [30] and those measured by myself on single crystals at SSRL. These were therefore not used for Fig. 4.5

4.2.1 High resolution x-ray diffraction of TbTe_3

X-ray diffraction data for TbTe_3 at room temperature reveal an incommensurate modulation wavevector $q = 0.296(4)\ c^*$ and its harmonic $2q$. Here, for clarity, we reference the superlattice peak inside the first Brillouin zone, resulting in a wavevector $q \approx 2/7\ c^*$, although ARPES[9] and STM[20] results suggest that the equivalent $q' = c^*\text{-}q = 0.704(4)\ c^* \sim 5/7\ c^*$ has more physical meaning. Figures 4.6 and 4.7 show representative diffraction patterns along the direction of the CDW wavevector for TbTe_3, as measured at SSRL Beamline 11-3 using 2 milliradian slits. Intensities of Bragg peaks from the average crystal structure are indicated by open circles and are scaled down by a factor of 1000. First and second harmonic superlattice peaks are marked by blue and red arrows. Higher harmonics were not observed. Some stray peaks were present from misoriented crystallites. The wavevector q and the equivalent q' are indicated in Fig. 4.6(b). Both the average structure Bragg peaks and the CDW superlattice peaks alternate in intensity, which can be attributed to the presence of two inequivalent Te atoms in the Te planes[4]. A simple model describing qualitative features of the diffraction pattern is presented in the Appendix.

The superstructure peaks in TbTe_3 are very sharp and, along with the average lattice peaks, were resolution-limited in our experiments. The inset to Fig. 4.8 shows a typical superlattice peak as measured in high-resolution mode, using a Ge(111) crystal analyzer at SSRL Beamline 7-2. From this we can draw lower bounds on the CDW correlation length ξ, calculated to be 1.8 μm within the Te planes and 0.5 μm perpendicular to the planes.

Heating measurements were taken with the sample mounted in an Anton-Paar furnace at SSRL Beamline 7-2 using a Ge(111) crystal analyzer. The integrated intensity of the (1 1 q) peak in TbTe_3 was followed as a function of temperature. Fig. 4.8 shows

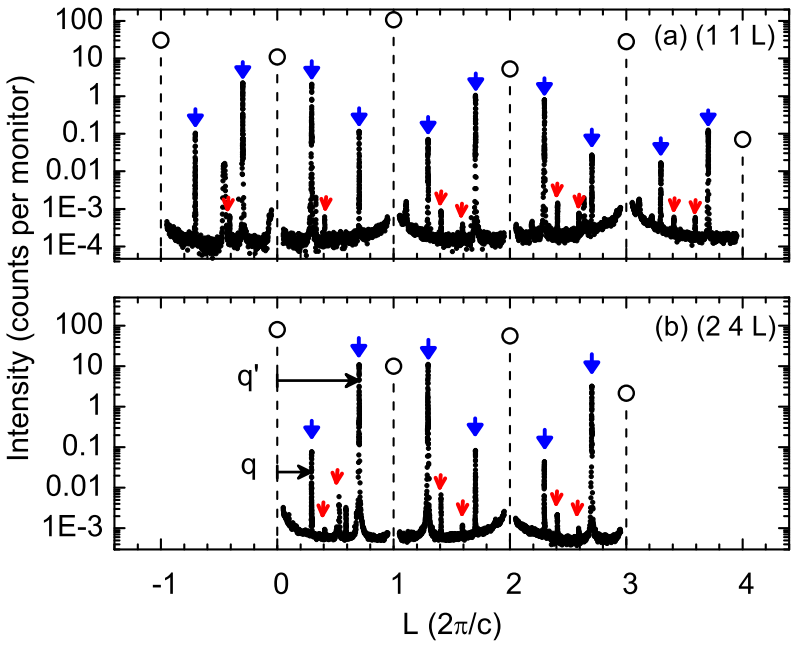

Figure 4.6: Representative x-ray diffraction patterns for $TbTe_3$ along (a) (1 1 L) and (b) (2 4 L). Intensities of Bragg peaks from the average structure are indicated by open circles and are scaled down by a factor of 1000. First and second harmonics of the CDW modulation are marked by blue and red arrows, respectively. The wavevector q and the alternate wavevector q' are marked.

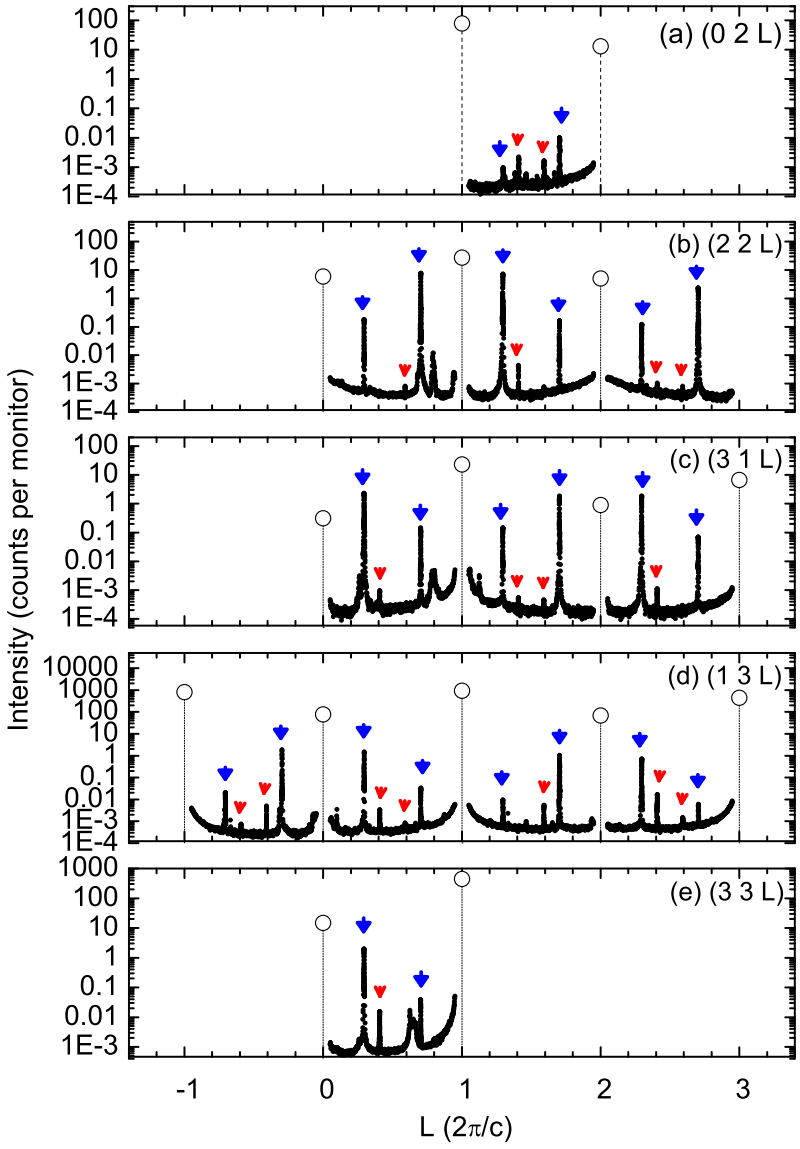

Figure 4.7: Representative x-ray diffraction patterns for TbTe$_3$ along (a) (0 2 L), (b) (2 2 L), (c) (3 1 L), (d) (1 3 L), and (e) (3 3 L). Intensities of Bragg peaks from the average structure are indicated by open circles and are scaled down by a factor of 1000. First and second harmonics of the CDW modulation are marked by blue and red arrows, respectively.

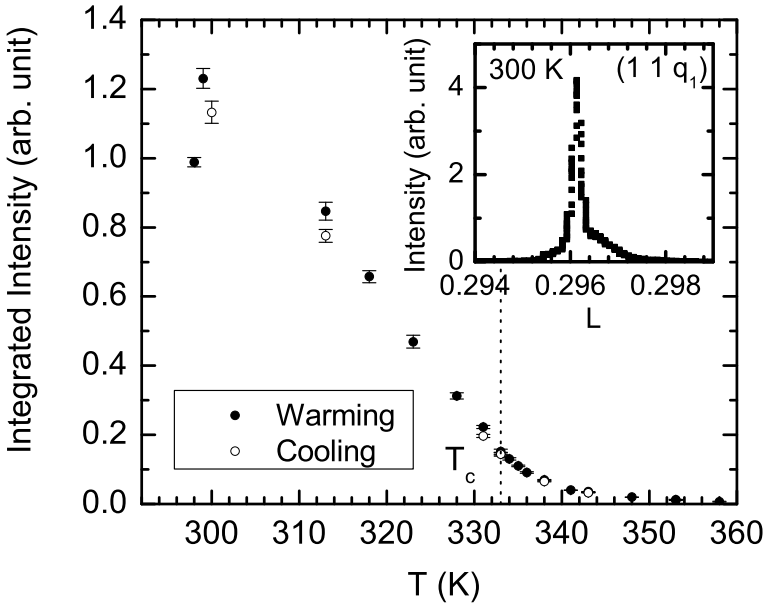

Figure 4.8: Temperature dependence of the integrated intensity of the (1 1 q) superlattice peak of $TbTe_3$ for increasing and decreasing temperatures. Inset: Raw data showing L scan for (1 1 q) at room temperature. T_c is indicated by a dashed vertical line.

the integrated intensity through the CDW transition for increasing and decreasing temperatures. The intensity rapidly decreases on heating from room temperature with no observable hysteresis, indicative of a second-order CDW transition as described theoretically[11]. Some scattering intensity, attributed to fluctuations, was observed above T_c up to 363 K, beyond which the peaks were too weak to distinguish from background. Error bars shown are obtained from Lorentz fits to the individual scans. A dashed vertical line marks the transition temperature T_c, which is derived from the correlation length analysis described below.

The full width at half maximum (FWHM) is shown in Fig. 4.9(a) for (1 7 q) along the b^* direction, and in Fig. 4.9(b) and (c) for (1 1 q) along the in-plane directions a^*

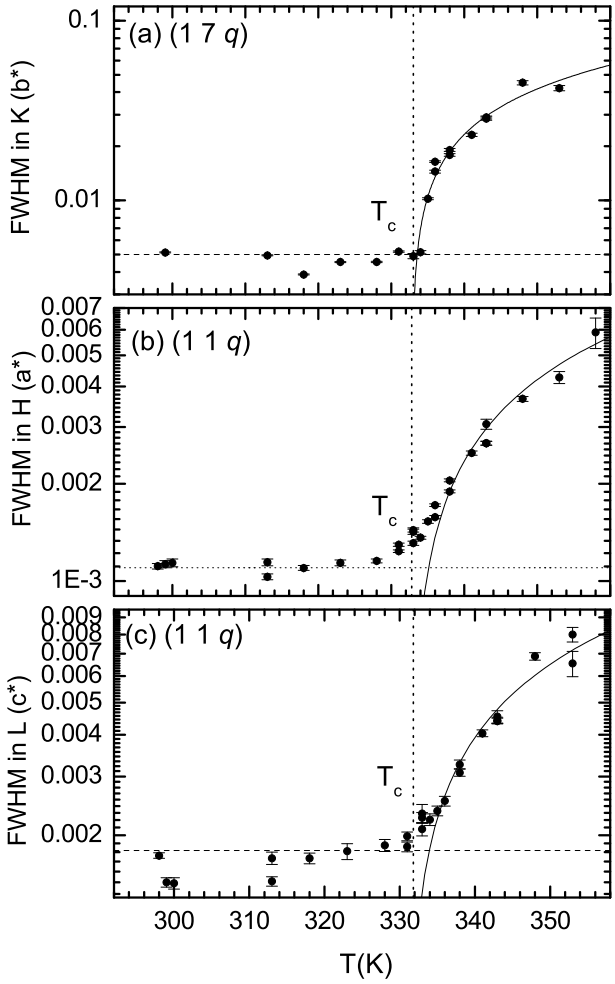

Figure 4.9: FWHM for TbTe_3 is shown for the (a)(1 7 q) superlattice peak in the out-of-plane direction, and for (1 1 q) superlattice peak in the in-plane directions (b)a and (c)c. Dashed horizontal lines mark the limits of resolution. The solid curves represent $\xi^{-1} \sim (T - T_c)^{\gamma}$ with T_c= 332.8(5) K and $\gamma = 2/3$. T_c is indicated by a dashed vertical line through all panels.

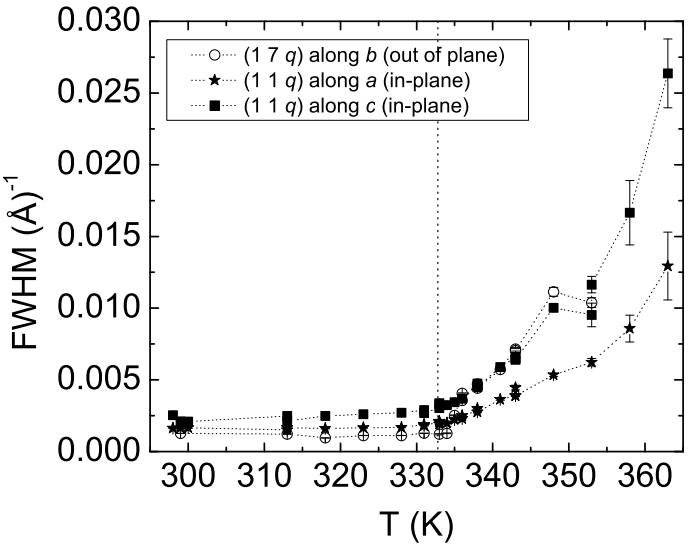

Figure 4.10: The FWHM for TbTe$_3$ from Fig. 4.9 in units of inverse angstroms.

and c^*, respectively. The FHWM are resolution limited at lower temperatures and increase sharply at the CDW transition. The FHWM in the b^* direction, while having the largest resolution limit, increases the most rapidly above the CDW transition to a reach a value of 0.042 at 353 K, while in the a^* direction at 353 K, the FWHM is almost 10 times smaller. The FWHM, being inversely proportional to the correlation length ξ, can be described by the expression $\xi^{-1} \approx (T - T_c)^{\gamma}$, where γ is taken as 2/3 to correspond to the X-Y model universality class (complex order parameter and three dimensions). The FWHM in the b^* direction, having the sharpest transition point, is fit in the interval from 334 to 353 K to this expression to obtain a transition temperature of $T_c = 332.8(5)$ K is obtained which is used for the ξ^{-1} fits in Figs. 4.9(b) and (c). This temperature is drawn as a dotted vertical line through all three panels of Figs. 4.9. Within error, this value of T_c corresponds with that obtained from resistivity measurements (336(3) K).

The CDW transition in TbTe_3 is also reflected in the temperature dependence of the in-plane lattice parameters a and c (Fig. 4.11(c)). Above T_c, a and c have a similar dependence, increasing linearly with temperature, and with a small relative difference of only 0.031% at 370K. Formation of the CDW appears to "stretch" the lattice from its expected value along the direction of the modulation wave vector (c axis), whilst slightly compressing the lattice in the perpendicular direction, such that the relative difference between a and c at 300 K, 0.13%, is larger than above the CDW transition.

The absolute value of the CDW wavevector for TbTe_3 is plotted in Fig. 4.11(d). The absolute value of q does not vary significantly with temperature between room temperature and T_c. For temperatures above T_c, the absolute value of q decreases with increasing temperature.

Measurements for TbTe_3 were extended from room temperature down to 25 K by using an ARS displex refrigerator at SSRL Beamline 7-2 using 1 milliradian slits. Fig. 4.12(a) shows the temperature dependence of the square root of the integrated intensity, which is proportional to the order parameter[1], together with the standard BCS curve. Data have been normalized by taking the average of the first four data points, from 30 to 100 K, and setting this value to unity. The close correspondence between the data and the BCS result confirm that the system can be treated within the weak-coupling limit. Error bars shown are $\pm 20\%$ of the integrated intensity, and represent the scatter associated with difficulties of centering the sample within the refrigerator. The apparent dip in the experimental data at approximately 150 K does not correlate with any additional features in the resistivity, and is most likely an experimental artifact.

Finally, the wavevector q (Fig. 4.12(b))remains incommensurate to the lowest

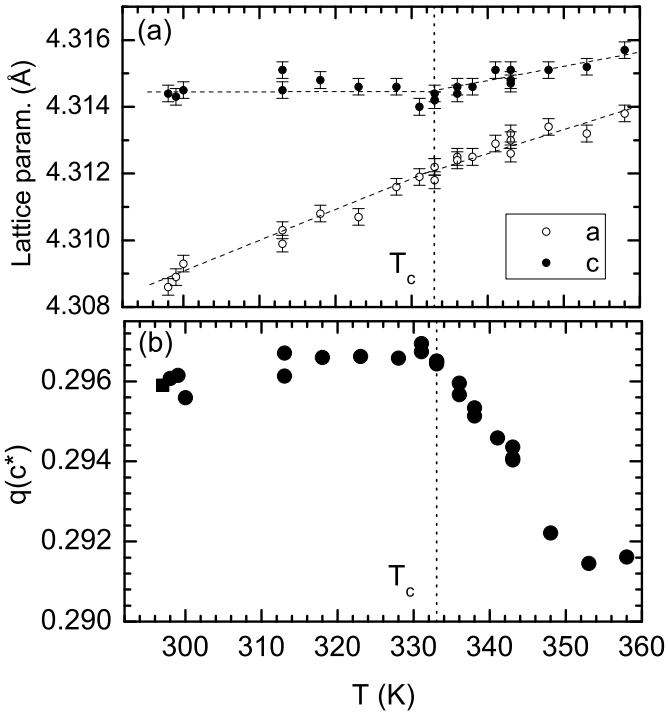

Figure 4.11: (a) The in-plane lattice parameters a and c for TbTe_3, with lines drawn to guide the eye. (b) The absolute value of q as a function of temperature. T_c is indicated by a dashed vertical line through both panels.

temperatures, and does not exhibit a lock-in transition.

4.2.2 High resolution x-ray diffraction of ErTe$_3$

To explore the case with two transitions, single crystal x-ray diffraction experiments were performed for ErTe$_3$ with sample mounted in a ARS displex refrigerator at SSRL Beamline 7-2. An incommensurate modulation similar to TbTe$_3$ with $q_1 \approx 2/7$ c^* was found in the temperature region $T_{c2} < T < T_{c1}$, as also noted by Malliakas *et al*[16]. For temperatures $T < T_{c2}$, an additional ordering along a^* was observed, perpendicular to the first wavevector. As investigated at 10K using a Ge(111) crystal analyzer, the wavevector of this additional ordering was $q_2 = 0.313(5)$ a^* whereas that of the original ordering was $q_1 = 0.300(5)$ c^*. Again, these values are cited in the first Brillouin zone even though the equivalent values $q_1' = c^*$ - $q_1 = 0.700(5)$ c^* and $q_2' = a^*$ - $q_2 = 0.687(5)$ a^*, may have more physical meaning for this system[9, 20]. The absolute value of q_2 is close but not identical to that of q_1.

A section of reciprocal space explored at 10 K is shown in Figure 4.13. Here, K = 3 (remember that b is the long axis) L $\in$ [3.5 5.5] and H $\in$ [0.5 3.5]. Filled symbols are those that were investigated, open symbols are those assumed to be present from symmetry. Bragg peaks for the average structure are marked by large (black) circles. Note that for K $>$ 0 these are extinct for H + K = odd. The superlattice peaks q_1 $\approx 2/7$ c^* are shown as (red) squares, with second harmonics in smaller (red) squares. The superlattice peaks $q_2 \approx 1/3$ a^* are shown as (blue) diamonds, with smaller (blue) diamonds denoting the second harmonics. Superlattice peaks at the linear combination $q_1 + q_2$, denoted as (purple) stars, were also observed, providing further evidence that these two wavevectors are real and present in the same crystallite.

Raw data taken at 155 K using a Ge(111) crystal analyzer are shown in Fig. 4.14(a)

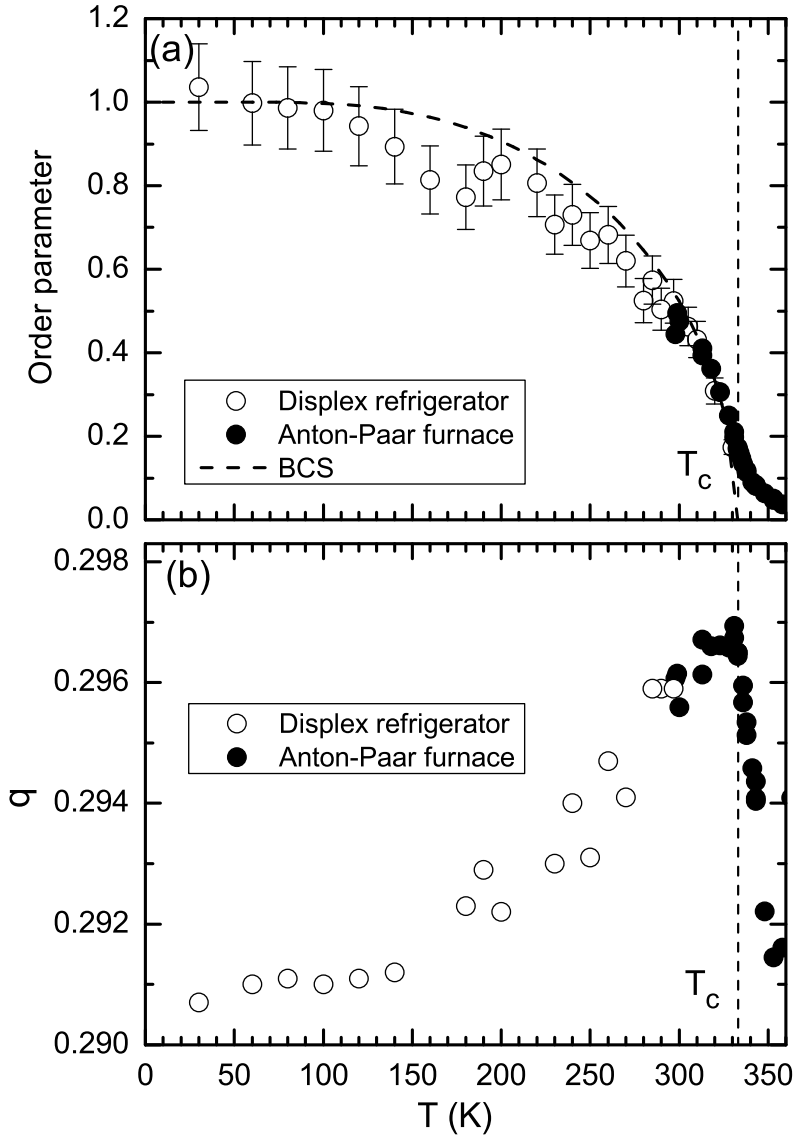

Figure 4.12: (a) Temperature dependence of the square root of the integrated intensity of the (1 1 q) superlattice peak of TbTe_3, which is proportional to the order parameter. Data are normalized to unity at T = 0. (b) The absolute value of q over the same temperature range. T_c is indicated by a dashed vertical line in both panels.

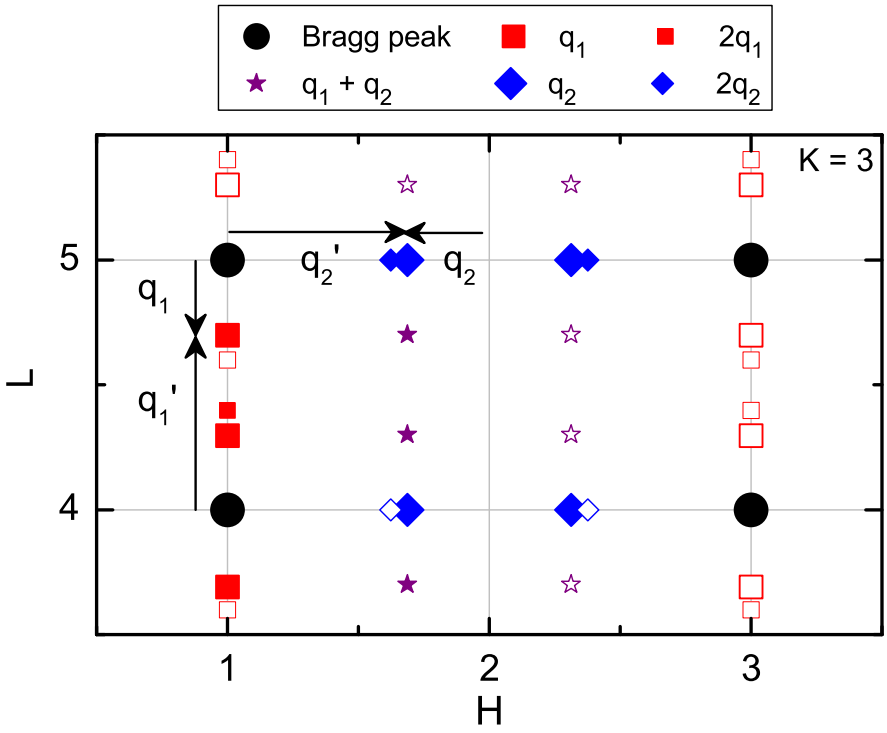

Figure 4.13: (color online) Reciprocal lattice map as obtained from the x-ray diffraction of ErTe$_3$. Solid symbols mark diffraction peaks found at 10 K. Hollow symbols mark peaks assumed to be present from symmetry.

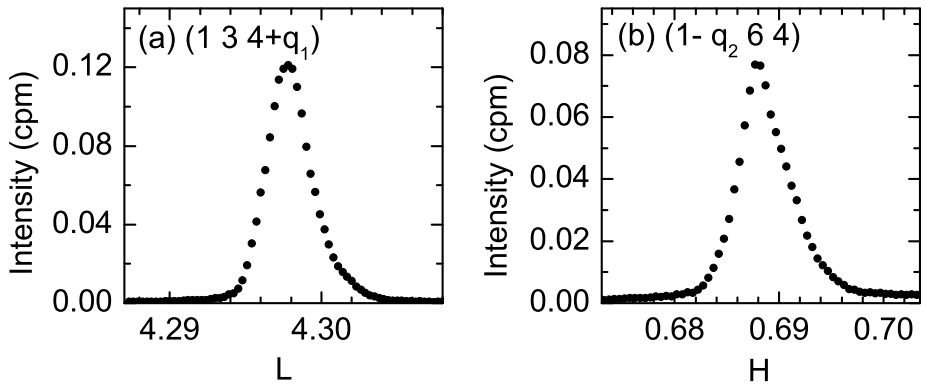

Figure 4.14: X-ray diffraction of ErTe$_3$. (a) L scan for (1 3 4+q_1) at 155 K. (b) H scan for (1-q_2 6 4) at 155 K.

and (b) for superlattice peaks q_1 and q_2, respectively. At this temperature, q_1 = 0.298(5) c^* and q_2 = 0.312(5) a^*. The FWHM for these peaks is larger for ErTe$_3$ due to a larger crystal mosaic, yet it remains clear that the magnitudes of q_1 and q_2 are very close but not identical.

Fig. 4.15 shows ϕ scans taken at 90 K using a Ge(111) crystal analyzer for (a) a q_2 first harmonic (2-q_2 3 5) and a neighboring linear combination peak (2-q_2 3 4+q_1). The intensity of the linear combination peaks decreases very rapidly with increasing temperature. Near T_{c2} this peak is still present but indistinct.

Temperature dependent measurements were performed on selected superlattice peaks in ErTe$_3$. The integrated intensities of a q_1 peak (-1 3 2+q_1) and a second harmonic of q_1 (-1 3 3-2q_1) were measured using 1 milliradian slits. Integrated intensities were normalized to the main Bragg peak (-1 3 2). In Fig. 4.16, as for TbTe$_3$, the square root of the integrated intensity of the first harmonic is plotted with the average of the first four data points (from 25 to 100 K) normalized to one. This agrees well

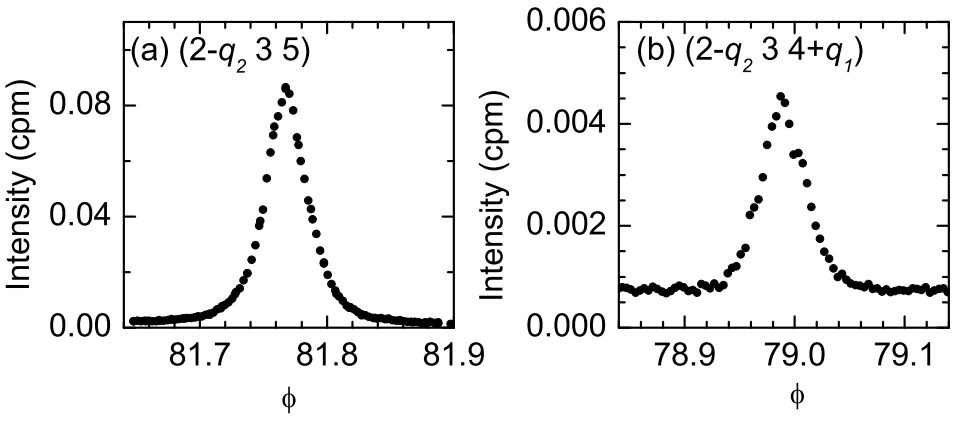

Figure 4.15: X-ray diffraction of $ErTe_3$. (a) ϕ scan for (2-q_2 3 5) at 90 K. (b) ϕ scan for (2-q_2 3 4+$q-1$) at 90K.

with the BCS order parameter, which is plotted using a transition temperature of T_{c1} = 267(3) K as obtained from resistivity, and is shown as a dashed curve. The second harmonic superlattice peak can be considered as either a second order diffraction harmonic of the first-order superlattice peak, or as the $2q_1$ component of a non-sinusoidal modulation[31]. As further discussed in the Appendix, in both cases, the integrated intensity of the second harmonic would be proportional to the order parameter to the fourth power[32]. In Fig. 4.16, the fourth root of the integrated intensity of (-1 3 3-2q_1), with the average of first four data points normalized to one, is shown to agree with the BCS curve. This is consistent with the case of the purely sinusoidal modulation, although the presence of non-sinusoidal components cannot be ruled out. Just above T_{c2} there is small dip in intensities of both peaks. Although this could be a sign of the second CDW interacting with the first, errors are such that this dip should not be overly interpreted. Error bars shown are ± 10 % of integrated intensity for both peaks.

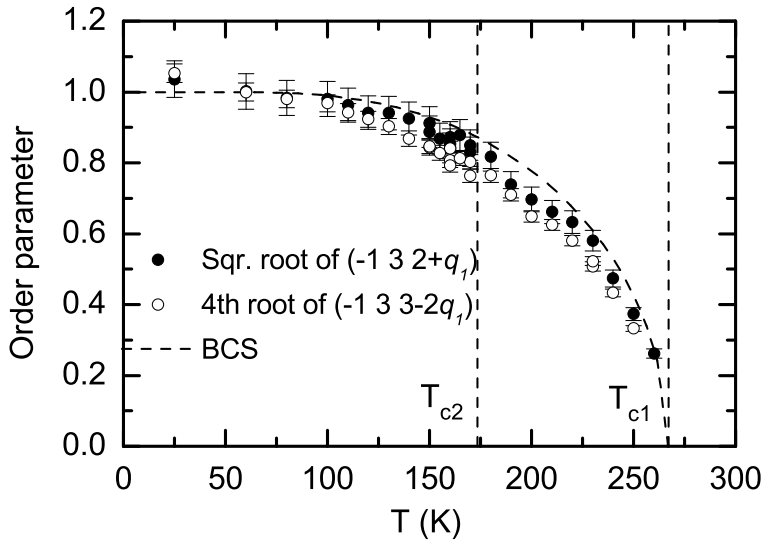

Figure 4.16: Temperature dependence of $ErTe_3$ superlattice peaks. The BCS order parameter (dashed line)is shown plotted with the square root of the integrated intensity of (-1 3 2+q_1), and the fourth root of the integrated intensity of (-1 3 3-2q_1), both of which are normalized to unity at T = 0.

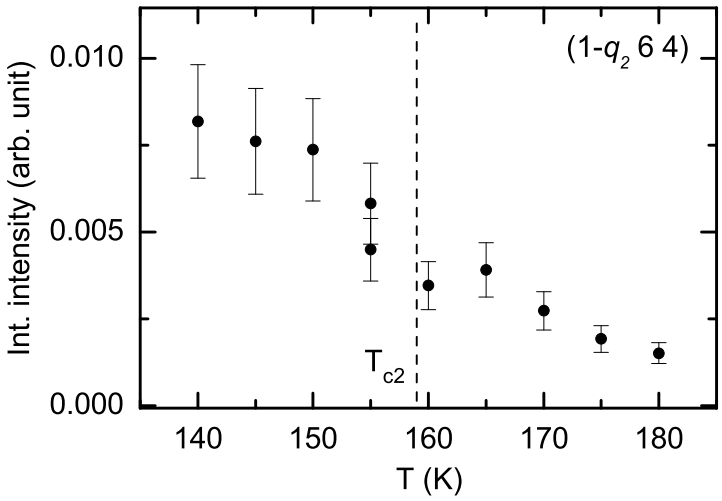

Figure 4.17: Temperature dependence of the integrated intensity of (1-q_2 6 4) for ErTe$_3$.

Using a Ge(111) crystal analyzer, the temperature dependence of the q_2 peak (1-q_2 6 4) was followed from 10 K to 180 K . Shown in Fig. 4.17 is the integrated intensity from 140 K to 180 K. The vertical dashed line is T_{c2}= 159(5) K as obtained from resistivity measurements. The integrated intensity decreases rapidly with increasing temperature across T_{c2}, similar to the behavior of q_1 through T_{c1}. Error bars shown are ± 20%. As in the case for TbTe$_3$ (Fig. 4.8(a)), scattering intensity is observed for several tens of kelvin above T_{c2}, indicative of the presence of substantial fluctuations.

The temperature dependence of the in-plane lattice parameters for ErTe$_3$, shown in Fig. 4.18, was measured using a Ge(111) crystal analyzer. From the available data, it is difficult to determine whether there is any abrupt change in the lattice constants at T_{c2} such as that seen for TbTe$_3$ at T_c. The behavior of the ErTe$_3$ lattice at T_{c1} was not explored.

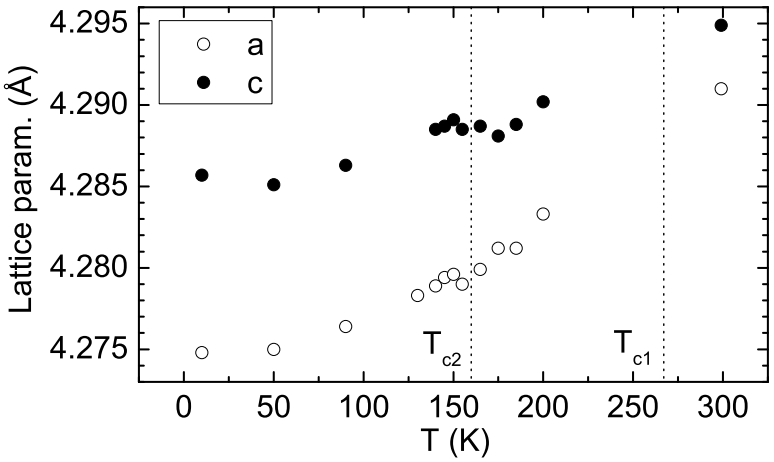

Figure 4.18: Temperature dependence of the ErTe$_3$ in-plane lattice constants.

4.3 Discussion

Here I address the magnitude of T_{c1} for these materials, the origin of the second transition for the heaviest members of the rare earth series, and the variation in T_{c1} and T_{c2} with chemical pressure.

Taking TbTe$_3$ as an example, if the maximum value of the CDW gap as measured by ARPES ($\Delta \sim 240$ meV) [10] is used to estimate a mean-field transition temperature via the familiar BCS expression, one obtains $T_{MF}(max) \sim 1600$ K, over four times greater than the observed T_c of 336 K. However, since the FS of RTe$_3$ is not perfectly nested, the mean field transition temperature will be substantially reduced from this value[33, 34, 35]. Furthermore, the observation of superlattice peaks with rapidly increasing FHWM and decreasing correlation length well above T_{c1} show the presence of substantial fluctuations. These further reduce the critical temperature from the mean field value, as has been previously observed for similar quasi-1D and 2D materials[1].

To gain insight to the variation in the observed CDW transition temperatures, J. Laverock and S. B. Dugdale performed band structure calculations for the unmodulated crystal structure for several members of the rare earth series, using the linear muffin-tin orbital (LMTO) method within the atomic sphere approximation, including combined-correction terms[36]. The 4f-electrons of the rare-earth elements were treated as open-core states. Lattice parameters measured at 300 K were used as input parameters for these calculations. Refined atomic positions in the $Cmcm$ space group as published by Malliakas *et al*[16] were used for compounds for which 300 K is above the CDW transition. The unmodulated $Cmcm$ space group was used for compounds for which 300K is below T_c, but the internal parameter (which defines the y-position of the Te planes in the unit cell) was taken from atomic refinements to the 4-dimensional $C2cm(00\gamma)000$ space group [16] at 300 K.

Typical results illustrating the FS seen in projection down the b^*-axis are shown in Fig. 4.19 for two specific compounds close to the ends of the rare earth series, CeTe_3 and ErTe_3. The calculated Fermi surfaces for these two isoelectronic compounds are, as anticipated, broadly similar, with only subtle differences in topology at the very corners of the diamond-like sheets of FS. Both the bilayer splitting and the dispersion along the b^*-axis (i.e. the thickness of the lines in Fig. 4.19) evolve weakly from CeTe_3 to ErTe_3, by $\sim +4\%$ in the first case, as measured by the separation of the two inner diamond sheets at $k_x = 0.16\ a^*$, and by $\sim +12\%$ in the latter, also measured at the inner diamond sheets at $k_x = 0.16\ a^*$. The overall bandwidth increases from CeTe_3 to ErTe_3, and the density of states at E_F, $n(E_F)$, decreases almost linearly from 21.1 for CeTe_3 to 19.9 states/Ry/cell[5] ErTe_3, a variation of approximately 5% (Fig. 4.20).

Quantitative calculations of the critical temperature are difficult for an imperfectly

[5]The "cell" referred to in these units is the unit cell described in Ref.[5], in which each unit cell is composed of two $R\mathrm{Te}_3$ formula units.

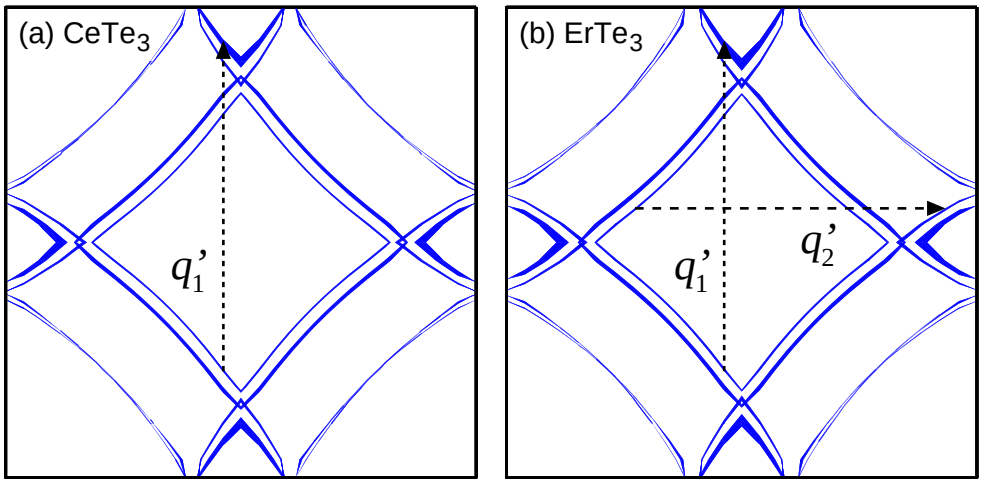

Figure 4.19: Fermi surface of (a) $CeTe_3$ and (b) $ErTe_3$ obtained from LMTO band structure calculations. The Fermi surface is shown in projection down the b^*-axis such that the thickness of the lines is indicative of the b^*-axis dispersion of each of the bands.. The horizontal dimension is k_x in the interval $\pm$ $a^*/2$. The vertical dimension is k_z in the interval $\pm$ $c^*/2$. The wavevectors q_1' and q_2' and corresponding nesting conditions are marked.

nested system, but it is clear that all three effects described above will contribute to the decrease in T_{c1} with decreasing lattice parameter. The subtle variation in the b^* axis dispersion and the bilayer splitting result in poorer nesting conditions, while the reduction in $n(E_F)$ directly affects the mean field transition temperature. In the absence of more detailed calculations we cannot determine the exact extent to which each of these effects contributes to the variation in T_{c1} across the rare earth series. However, given that the mean field transition temperature varies exponentially with $n(E_F)$ it is likely that the variation in $n(E_F)$ plays the dominant role.

The second CDW transition, observed only for the heaviest members of the rare earth series, is particularly intriguing. Specifically, in contrast to most usual CDW transitions, the effect of increasing (chemical) pressure is actually to *increase* T_{c2}. It appears that this unusual behavior is directly linked to the variation in T_{c1}. In

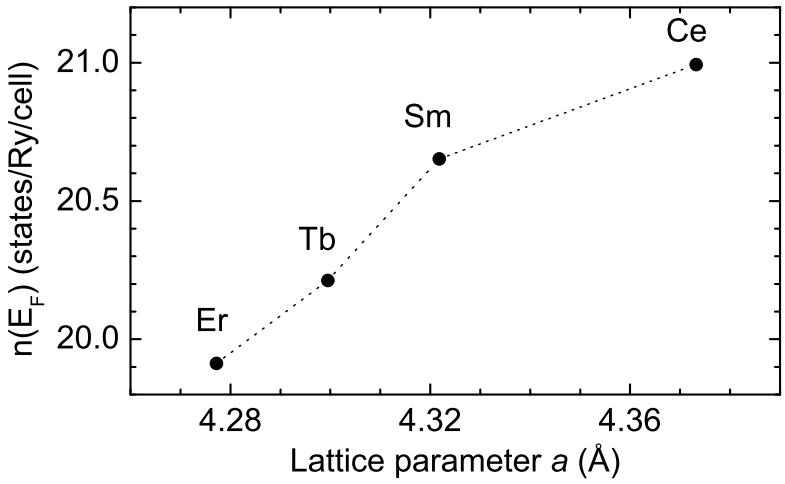

Figure 4.20: Density of states at E_F for representative members of the RTe$_3$ series, as obtained from LMTO band structure calculations, shown as a function of the in-plane lattice parameter a. Dashed lines are drawn between the points to guide the eye. (The lattice parameters are those obtained from Ref.[16], which were those used for LMTO calculations.)

particular, the extent to which the FS is gapped below T_{c1} depends on the maximum size of the CDW gap. A reduction in the maximum gap causes a reduction in the total area of the FS that is gapped precisely because the FS is imperfectly nested. This is borne out by recent ARPES experiments, which reveal that for the compounds with smaller lattice parameters the CDW gap extends a smaller distance around the FS from the tips of the diamond sheets at $k_x = 0$[6][10]. Hence, on traversing the rare earth series from LaTe$_3$ towards TmTe$_3$, progressively more of the FS remains intact below T_{c1}, and as a consequence is available for a subsequent CDW transition at a lower temperature. Having already lost the "tips" of the diamond sections of the FS

[6]ARPES measurements for CeTe$_3$ reveal a maximum gap of 400 meV at the Fermi energy for $k_x = 0$ (i.e. the "tips" of the diamond sheets of the FS that are pointing along the c^* direction - see Fig 8). The gap diminishes in magnitude the further one goes around the FS from this point, reaching zero at approximately $k_x = 0.25\ a^*$. In comparison, for SmTe$_3$, for which the maximum gap is only 280 meV, the gap extends only as far as $k_x = 0.18\ a^*$[10].(See Fig. 1.19)

that point in the c-axis direction at the first transition, the second transition must involve sections of the FS closer to the tips of the diamonds pointing in the transverse a-axis direction. Indeed, these are exactly the regions of the FS that contribute to the competing peak in $\chi(q)$ found at $2/7\ a^*$ in band structure calculations for the unmodulated structure[7]. Preliminary ARPES results for ErTe_3 confirm this picture, revealing additional gaps forming on sections of the FS close to the tips of the diamond sections of the FS pointing in the a^* direction[37]. The corresponding jump in the resistivity at T_{c2}, related to the amount of FS gapped at the transition, is largest for the compound with the largest value of T_{c2} (smallest value of T_{c1}) and smallest area of initial FS gapped at T_{c1}. The resulting "rectangular" CDW state is characterized by orthogonal, independent wave vectors, almost equal in magnitude, but with an order parameter that is developed to a different degree in the two directions.

Yao and coworkers have recently addressed the question of the origin of the unidirectional CDW for the lightest members of the $R\mathrm{Te}_3$ series[11]. Using a simple tight-binding model for a square lattice, and considering only non-interacting Te p_x and p_z bands, they found that for sufficiently high values of the electron-phonon coupling (and consequently T_c) a unidirectional ("stripe") CDW at 45 degrees to the Te-Te bonds is favored over a bidirectional ("checkerboard") state in which p_x and p_z sheets of the FS are individually gapped by orthogonal wave vectors which are oriented at a different angle to the stripe phase. In this model, the stripe phase gaps a sufficient amount of the FS that only one of the two equivalent directions (a and c in the real material) is chosen for the lattice modulation. The weak orthorhombicity

[7]LMTO band structure calculations reveal almost equivalent peaks in $\chi(q)$ at $\approx 2/7\ c^*$ and $\approx 2/7\ a^*$, corresponding to nesting wave vectors between the inner and outer diamond sheets of the FS along the c^* and a^* directions respectively. The peak at $2/7\ c^*$ is slightly larger in magnitude, and hence determines the initial CDW wave vector if we assume a constant electron-phonon coupling. However, the difference is slight, and is only apparent in these calculations when spin-orbit coupling is included[2].

of $R\mathrm{Te}_3$ provides a natural symmetry-breaking between the a and c axes such that for the lightest members of the series the unidirectional CDW is always observed along the c-axis and never along a. It will be intriguing to see whether this insightful toy model can be extended to incorporate the observed "rectangular" CDW phase at a more quantitative level than the qualitative arguments presented above.

Implicit in all of the above discussion has been the assumption that the electron-phonon coupling itself does not have a strong q-dependence and does not vary substantially across the rare earth series, though it is not necessarily immediately obvious that this should be the case. The Te-Te bond-length in $R\mathrm{Te}_3$ is substantially longer than the standard covalent bond-length, implying that the unmodulated high-temperature structure of $R\mathrm{Te}_3$ is inherently unstable, regardless of the low-dimensional electronic structure[15]. The close correspondence between the maxima in $\chi(q)$ and the observed superlattice wave vectors clearly demonstrates that the electronic system plays a pre-eminent role in the lattice modulation in this material. But it is not clear whether it is the *only* driving force for the instability. To determine the relative role played by the lattice will take a substantial computational effort. However, this material appears to be a model system to quantitatively calculate the role played by an incipient lattice instability in CDW formation, something which to date has been lacking for most other CDW systems[2].

4.4 Conclusions

The $R\mathrm{Te}_3$ family of compounds have a remarkable phase diagram. All members of the series exhibit a CDW transition to a state characterized by a simple unidirectional

incommensurate lattice modulation with wave vector $q_1 \approx 2/7\ c^*$. The transition temperature T_{c1} is very sensitive to chemical pressure, varying by over 200 K across the series, principally ascribed to the variation in the density of states at the Fermi level $n(E_F)$. The heaviest members of the series exhibit an additional CDW transition at a lower temperature T_{c2}, with an almost equivalent wavevector oriented perpendicular to the first, along the a^*-axis. The resulting "rectangular" CDW state consists of perpendicular modulation wave vectors almost equal in magnitude, but with independent order parameters, each developed to a different degree at any given temperature. These observations can be understood in terms of the second CDW nesting regions of the original FS that are ungapped by the first CDW. Specifically, on traversing the rare earth series, as T_{c1} decreases, increasingly more of the remaining FS becomes available to drive a second CDW with a modulation wave vector transverse to the first.

Chapter 5

De Haas van Alphen Oscillations

5.1 $LaTe_3$

De Haas van Alphen (dHvA) oscillations are investigated for the CDW state of the diamagnetic compound $LaTe_3$. $LaTe_3$ exhibits just one CDW state with wavevector $q_1 \approx 2/7\ c^*$ with a transition temperature anticipated to be over 400 K. Its reconstructed Fermi surface is expected to be similar to that of $CeTe_3$, which has been investigated by ARPES by collaborators V. Brouet and coworkers[9]. ARPES measurements reveal a partially gapped Fermi surface and tentatively propose a reconstructed Fermi surface with thin extended regions. It is unknown, however, whether these regions are interconnected or whether they are separate small pieces. DHvA oscillations in magnetization, which provide a measure of the area enclosed by the reconstructed FS, are uniquely suited for refining this estimated shape of the reconstructed FS. (An brief background of dHvA is given in the Appendix.) At the time of writing, a manuscript describing these results is in preparation[38].

5.1.1 Results

Measurements of $LaTe_3$ were made using AC susceptibility and cantilever torque techniques as described in Ch. 3. Clear oscillations were observed in the both the susceptibility and torque measurements. At least three distinct frequencies were observed for fields oriented parallel to the b-axis: $\alpha = 0.060$ kT, $\beta = 0.52$ kT, and $\gamma = 1.6$ kT, with the β frequency composed of two or more very closely spaced frequencies.

The magnetic susceptibility was measured in a dilution refrigerator at a base temperature of 10 mK. A $LaTe_3$ crystal was shaped to a weight of 0.7 mg to fit within the susceptometer coils. The magnetic field was swept from 15 to 0.5 T at a rate of 0.025 T/min, with a data density of one point per 0.6 Oe. The susceptibility for fields oriented along the b-axis is shown in Fig. 5.1(a), plotted as a function of inverse field. A third-order polynomial background has been subtracted but the data shown is otherwise unaltered. The predominant frequency seen in the raw data is the β frequency with a beating that arises from its closely split peaks. To emphasize the contribution of β to the total oscillatory content, the envelope of β, derived from the fourier transform of the raw data, is shown in blue. As is characteristic of quantum oscillations, the amplitude of the oscillations in Fig. 5.1(a) increases exponentially with increasing field, with oscillations first becoming noticeable at fields of approximately 1 T.

Fig. 5.1(b) shows a fourier transform of Fig. 5.1(a) over the field range 1.5 to 15 T. A Hamming window was used for the fast fourier transform (FFT). The frequencies α, β, and γ are labeled. The β frequency is larger in amplitude than the others and is composed of a cluster of peaks with frequencies ranging from 511 to 553 T, as shown more clearly in the inset to Fig. 5.1(b). In this fourier transform, the γ peak has some structure, but, unlike β, is not distinctly split into separate peaks. Also labeled in

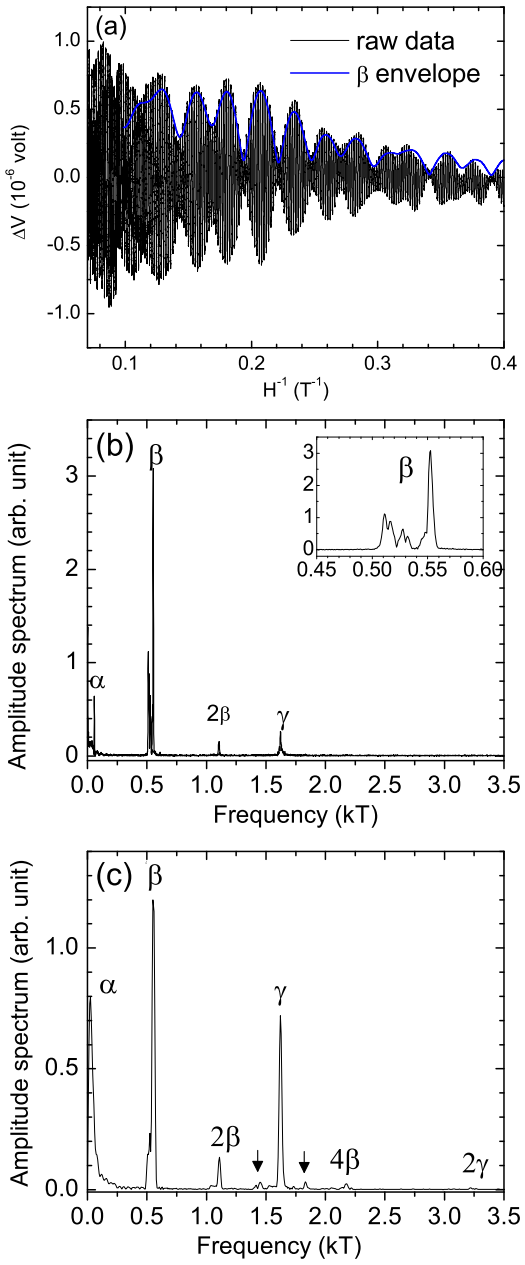

Figure 5.1: (a)The susceptibility of $LaTe_3$ at T = 23 mK showing dHvA oscillations. The envelope of the β frequency is shown in blue. (b) Fourier transform over the field range 1.5 to 15T. (c) Fourier transform over the field range 7 to 15T. The principal frequencies α, β, and γ and higher harmonics are labeled. Arrows indicate additional frequencies as described in the text.

the fourier transform is the second harmonic 2β.

A fourier transform of the data from 7 to 15 T is shown in Fig. 5.1(c), also using a Hamming window. With a shorter field range, the higher frequency components in the data are emphasized. Higher harmonics 4β and 2γ of the fundamental frequencies are clearly visible, as well as small peaks at 1.45 and 1.73 T on either side of γ, which are labeled with arrows. The shortened field range also reduces the fourier transform resolution, partially obscuring the β peak splittings.

Quantum oscillations as measured with a torque magnetometer on a different sample of $LaTe_3$ results in a similar frequency spectrum. Fig. 5.2(a) shows the results of a torque magnetometer measurement performed at 1.9 K with the *b*-axis of the crystal offset from H by 5°. (The offset is necessary as an orientation with H parallel to the *b*-axis would result in zero torque.) A third order polynomial background has been subtracted from the data shown in Fig. 5.2(a). As before, the amplitude of the oscillations increase exponentially with field, with the oscillations first becoming visible at fields of approximately 4T.

The fourier transform of the torque data is shown in Fig. 5.2(b). Again, the predominant frequencies are labeled as α, β, and γ. The spectrum is remarkably similar to that in Fig. 5.1, despite the reduced field range and the higher temperature. Here, the β frequency is clearly split into two, labeled in the inset to Fig. 5.2(b) as β_1 and β_2. Given the smaller field range, sparser point density, and a higher noise floor, higher harmonics above 2 kT were not observed.

These torque measurements were repeated at with the crystal rotating about an in-plane axis. Orientation by x-ray diffraction in a Panalytical X'Pert Diffractometer revealed that the *a*-axis was the axis of rotation i.e. that the field was oriented in the *b*-*c* plane of the crystal. However, $LaTe_3$ is prone to twinning due to the weak

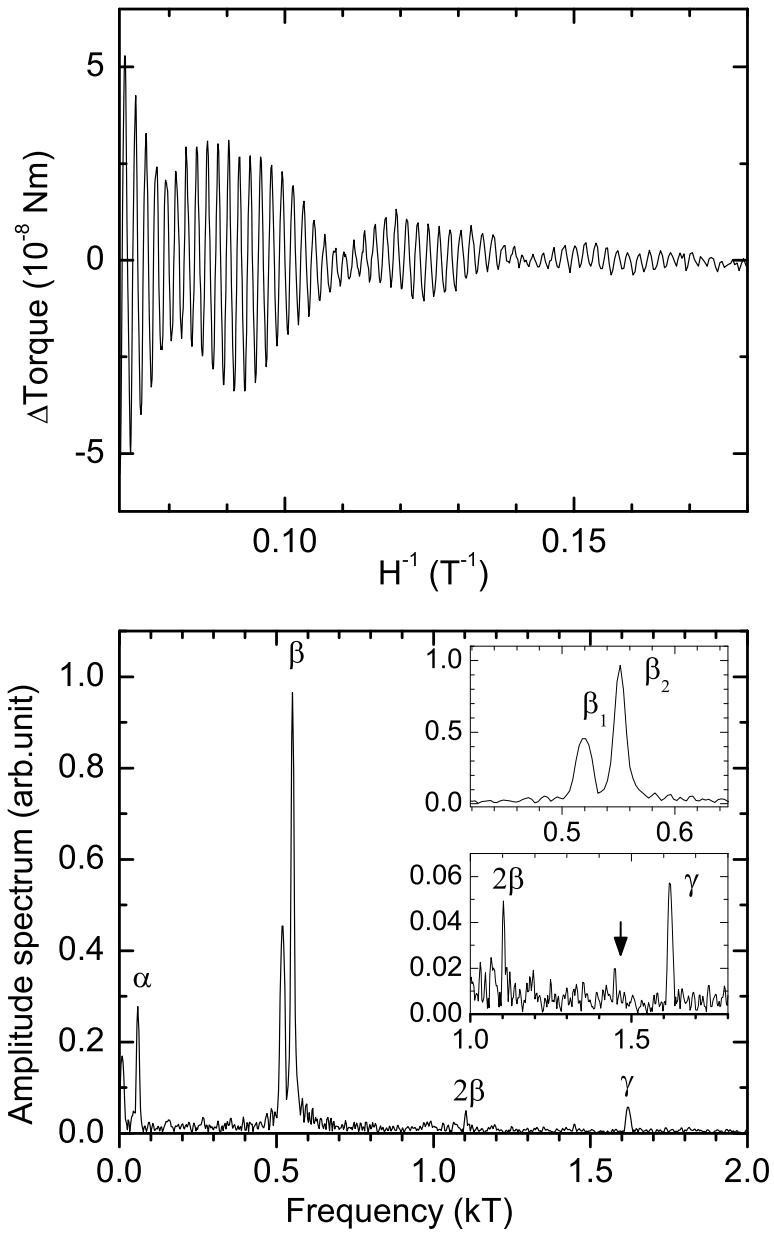

Figure 5.2: (a)Torque data for $LaTe_3$ at T = 2 K with field oriented 5° from the *b*-axis, with polynomial background subtracted. (b) Fourier transform from 4T to 14T. The principal frequencies α, β, and γ and the higher harmonic 2β are labeled. The insets show the double peaks β_1 and β_2, as well as a very small peak at 1.45 kT marked by an arrow.

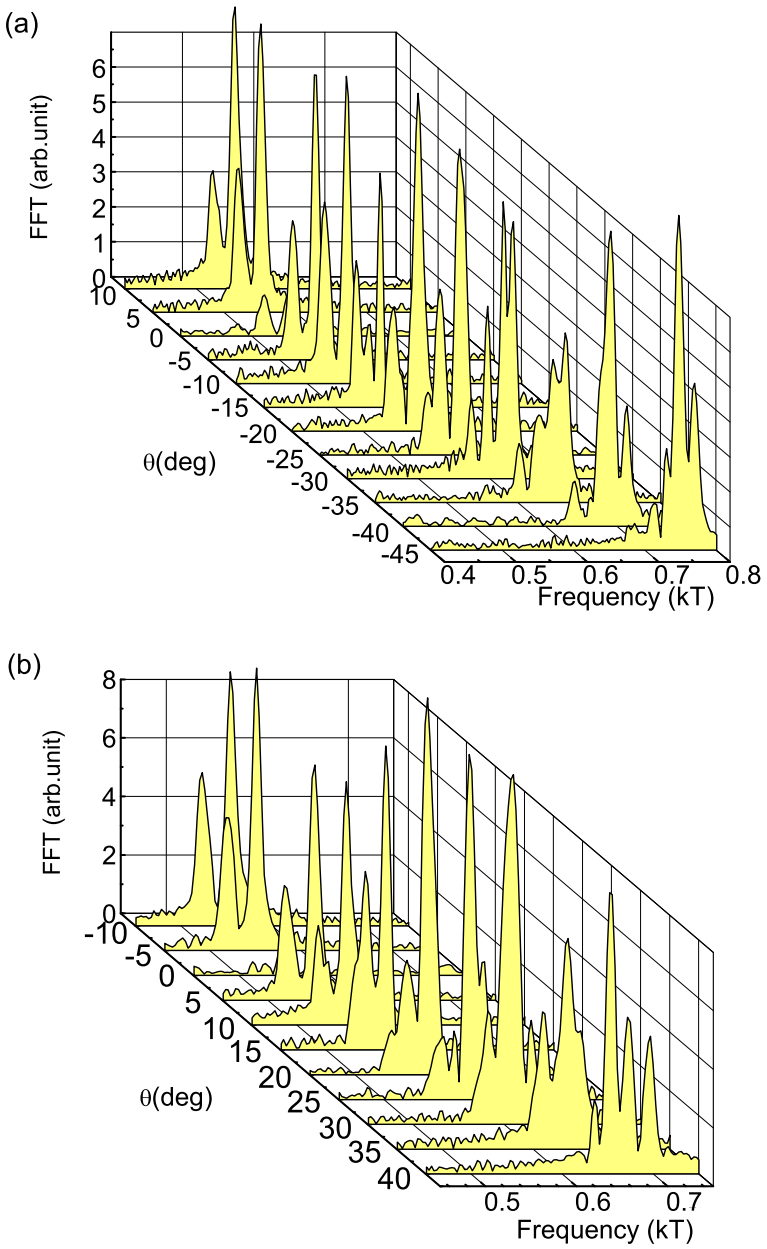

Figure 5.3: Fourier transforms for angle-dependent torque measurements of $LaTe_3$ at 2 K, focussing on the β frequency. The field is oriented in the b-c plane at an angle θ measured with respect to the b-axis. Fourier transforms were taken over the range 4 to 14 T.

Van de Waals bonding between the double Te sheets, and given the short penetration depth of the X'Pert (described in Ch. 2), it is possible that the sample also contained undetected grains for which the c-axis was the axis of rotation.

Torque measurements were performed at 2 K and at increments of 5° from -45° to 40°, where $\theta = 0$ when the field is parallel to the b-axis. Fig. 5.3 shows how the β peak splitting in the fourier transform (over the range 4 to 14 T) varies with θ. While β consists of two peaks at angles near zero, at higher angles it consists of three or four peaks. A close look at the fourier transforms shows how the four peaks emerge from two. For example, in the bottom panel, at 5°, β is two clean peaks. As the angle is increased to 10°, 15°, and 20°, a shoulder begins to form on the leftmost peak, β_1, until at 25°, β_1 is clearly now itself two distinct peaks. Meanwhile, β_2 becomes noticeably broader between 15° and 20° until at 25° a peak splits off from the right side of β_2. While at 25°, four peaks are clearly seen, on increasing to 30° the two central peaks have merged, and for larger angles although four peaks are again observed it is difficult to unambiguously identify the origin of each peak.

This information is consolidated in Fig. 5.4 where the fourier transforms (over the range 4 to 14 T) are shown as a background shading with darker regions representing higher intensities. Overlayed are markers representing peak positions; the total span of the error bars is given by the full-width at half-max (FWHM) of each peak. An effort has been made to identify which peaks merge or split into other peaks as the angles change. As angles increase or decrease from zero, β_1 splits into two peaks β_{1A} and β_{1B}, while β_2 splits into two peaks β_{2A} and β_{2B}. The function $1/\cos\theta$, which represents the angle dependence of a FS sheet with no b-axis dispersion, is shown as solid curves. The close correspondence to $1/\cos\theta$ indicates that the FS sheets are indeed quasi-2D with minimal b-axis dispersion, as indicated by band structure

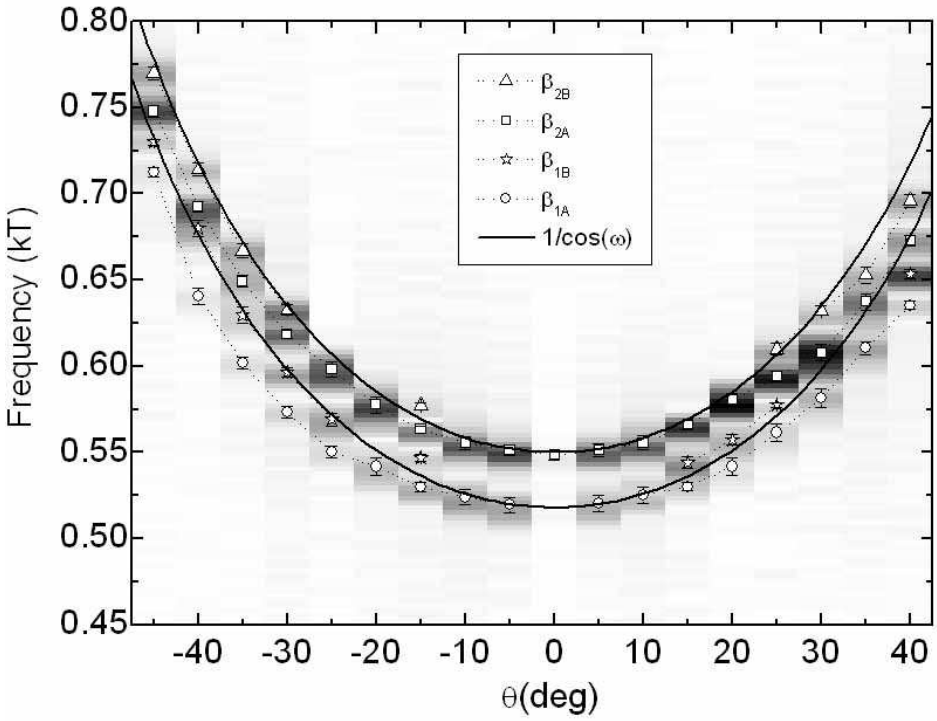

Figure 5.4: An overhead view of the fourier transforms of Fig. 5.3. Fourier transforms for each angle are marked by background shadings. Data markers are positioned at the center of each peak, with error bars representing the full width at half max. Solid curves represent $1/\cos\theta$.

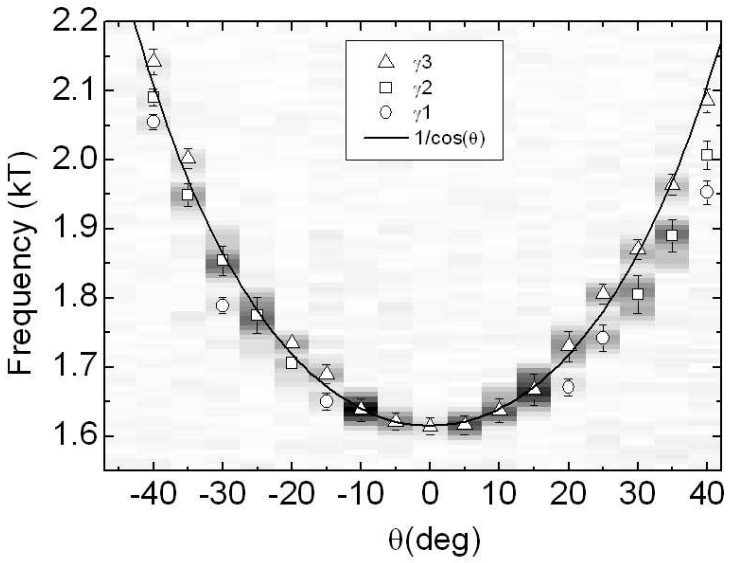

Figure 5.5: Fourier transforms for the torque measurements of $LaTe_3$ at 2 K, focussing on the γ frequency. The field is oriented in the b-c plane with an angle θ measured with respect to the b-axis. Fourier transforms for each angle are marked by background shadings. Data markers are positioned at the center of each peak, with error bars representing the FWHM. Solid curves represent $1/\cos\theta$.

calculations[5]. There are small deviations from $1/\cos\theta$: β_{1B} and β_{2B} seem to follow $1/\cos\theta$, while β_{1A} and β_{2A} are "shallower" than $1/\cos\theta$. This implies that the latter two frequencies result from FS maxima.

Fig. 5.5 shows a similar plot for the γ frequency. Again, the fourier transform data (over the range 7 to 14 T) is shown as a background shading, while the markers denote the peak positions. The total span of the error bars is given by the FWHM of each peak. While γ is a single peak close to $\theta = 0$, it soon splits into two and three peaks at higher angles. An attempt was made to identify γ_1, γ_2, and γ_3, as they split and merge with increasing θ. The frequency γ_3 seems to follow the $1/\cos\theta$ dependence very closely, while γ_1, and γ_2 are shallower than $1/\cos\theta$.

Fig. 5.6 shows the results of angle-dependent measurements for the frequencies

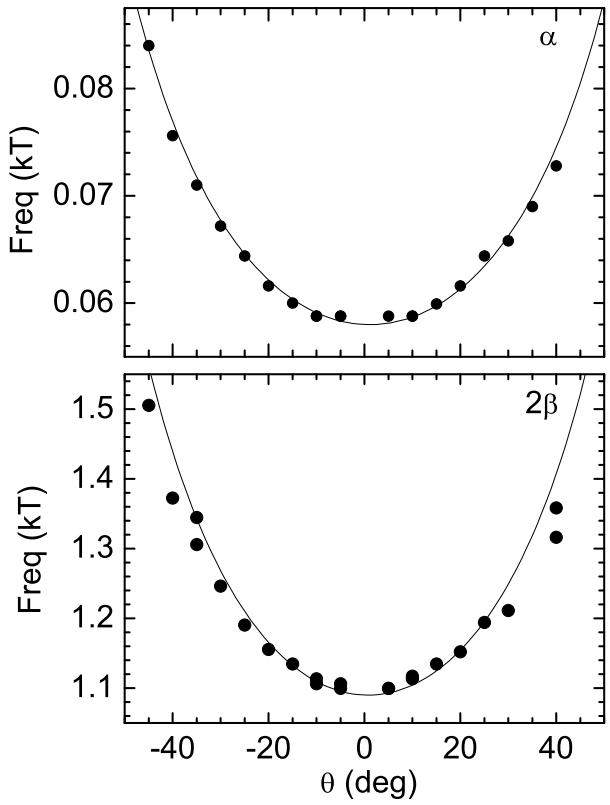

Figure 5.6: The (a)α and (b)2β frequency peaks in the fourier transform for the torque measurements of $LaTe_3$ at 2 K. The field is oriented in the b-c plane with an angle θ measured with respect to the b-axis. Solid curves represent $1/\cos\theta$.

Symbol	Suscep. F(kT)	Torque F(kT)	Area(%BZ)	Mass (m_0)
α	0.060	0.060	0.28	0.17
β	0.511-0.553			
β_1		0.52	2.44	0.175
β_2		0.55	2.59	0.184
2β	1.1	1.1	5.18	0.31
γ	1.6	1.6	7.61	0.39

Table 5.1: Fundamental dHvA frequencies obtained from susceptibility and torque measurements of $LaTe_3$, corresponding fractional areas of the FS, and the associated cyclotron masses as obtained from Lifshitz-Kosevitz fits to the temperature-dependent torque data.

(a)α and (b)2β. In each figure, a line is plotted representing $1/\cos\theta$. As before, there is a close correspondence to $1/\cos\theta$ indicating that the FS sheets are indeed quasi-2D. It is especially not surprising that the harmonic 2β shows quasi-2D behavior, as its angle-dependence should be the same as that of its fundamental. 2β splits into two at higher angles, but the peak is too weak to show the detailed structure that was seen in the fourier transform of its fundamental, β.

The same crystal was used for temperature-dependent measurements from 1.9 to 25 K with the torque magnetometer, and with a field range of 4 to 14 T. The crystal was mounted with the magnetic field offset from the b-axis by 5°. The amplitudes of each frequency as derived from the fourier transforms are shown in Fig. 5.7 for (a)α, (b)β_1 and β_2, (c)2β and (d)γ. The field ranges for each set of fourier transforms is indicated in each panel. The amplitudes decrease as temperature is increased. Fits to the Lifshitz-Kosevich expression result in values for the masses, which are shown in Table 5.1. The amplitudes for the small unnamed frequency at 1.45 T is also shown in Fig. 5.7(c) although the frequency was very weak, and not enough points were obtained to result in a reliable estimate of the mass for this frequency.

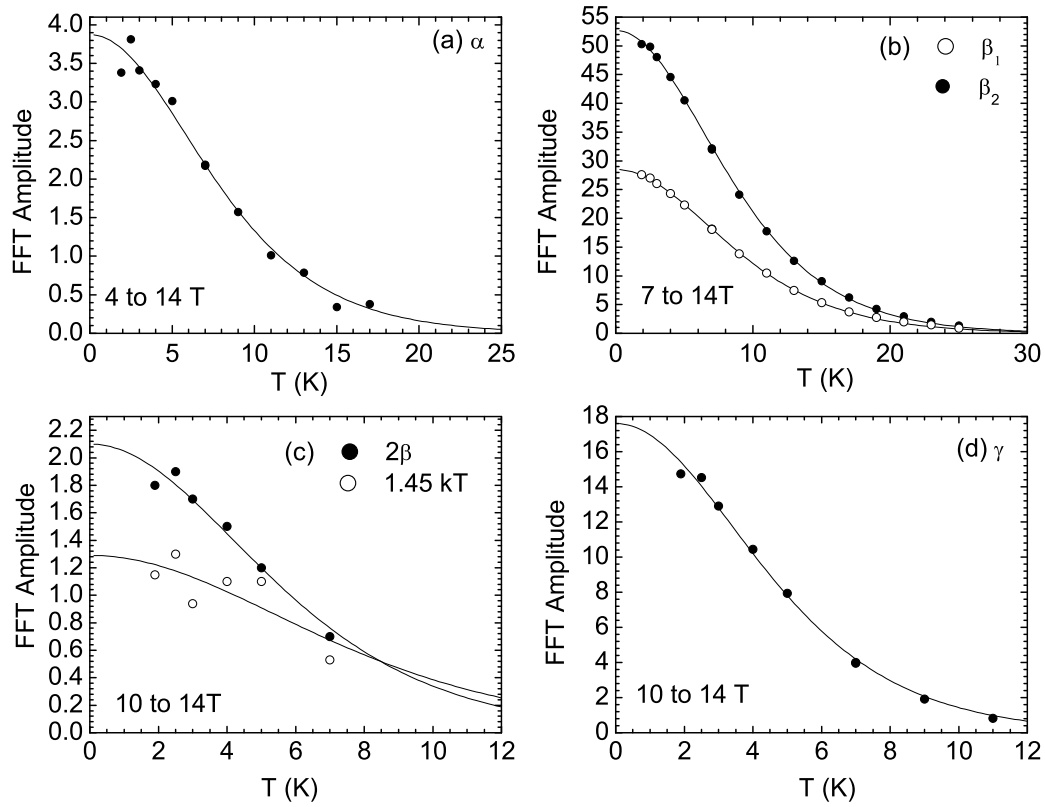

Figure 5.7: The temperature-dependent frequency amplitudes for $LaTe_3$, from torque measurements with field oriented 5° from the b-axis. a)α (0.060 kT), (b)β_1 (0.52 kT) and β_2 (0.55 kT), (c)2β (1.1 kT), and (d)γ (1.6 kT). Additional data for the weak 1.45 kT frequency are shown in panel(c). Solid lines show fits to the Lifshitz-Kosevich relation, as described in the text. The field range used for each set of fourier transforms is indicated in each panel.

5.1.2 Discussion

The two sets of measurements shown for fields oriented $H\|b$ (or close to $H\|b$ for the torque measurement) differ primarily in the number of split peaks observed in the β frequencies, with up to six observed in the susceptibility measurement in Fig. 5.1, and two observed in the torque measurement in Fig. 5.2. The difference is unlikely to be due to the lower temperature of the susceptibility measurement as there are only minimal changes in the oscillation amplitudes for temperatures below 2 K, which can be seen from the Lifshitz-Kosevitz curves in Fig. 5.7. However, multiple peaks can arise if a sample contains multiple crystallites oriented at subtlety different angles. The fewer split peaks observed in the torque measurements, as well as the angle dependent measurements that show symmetry about $\theta = 0$, imply that any influence from secondary misoriented crystallites in the torque sample is small. As a result, further analysis of the β frequency is based on the torque results.

The frequencies α, β, and γ correspond to closed orbits with cross-sectional areas that can be expressed in terms of Brillouin zone (BZ) area, defined by $a^* \times c^* = 2.027(\mathring{A})^{-2}$, where $a = 4.4045\mathring{A}$ and $c = 4.421\mathring{A}$ from Table 4.2. As shown in Table 5.1, the smallest frequency, α, corresponds to a 0.25% of the BZ. The two peaks β_1 and β_2 correspond to 2.44% and 2.59% of the BZ, respectively. The largest frequency γ corresponds to 7.6% of the BZ.

As indicated by ARPES[9], the X pockets may remain unmodified in the presence of the CDW. For the FS of $CeTe_3$ as shown in Fig. 4.19(a), the inner X pocket has minimal and maximal FS areas of 2.082% and 2.641%, while the outer X pocket has minimal and maximal areas of 3.596% and 4.131%. These are similar to the measured values of β. In principle, four distinct frequencies are anticipated from the X sheets at $\theta = 0$, corresponding to "neck" and "belly" orbits of each of the

two bilayer-split sheets. In practice, the finite fourier transform resolution for the experimental conditions results in just two distinct frequencies at θ near zero. As shown in Fig. 4.19(a) for $CeTe_3$, LMTO band structure calculations indicate that the bilayer splitting is larger than the b^*-axis dispersion for both sheets and β_1 and β_2 are tentatively assigned to the inner and outer X pockets respectively.

It is tempting to ascribe the split peaks β_{1A} and β_{1B} to the neck and belly frequencies of the inner X pocket, and similarly for β_{2A} and β_{2B} to the neck and belly frequencies of the outer X pocket. But a simple sinusoidal b-axis dispersion should give neck and belly frequencies that are distinct at $\theta = 0$ but then converge with increasing θ before meeting at a Yamaji angle[39, 40]. The divergent behaviors of β_{1A} and β_{1B}, and β_{2A} and β_{2B}, could reflect deviations from a simple sinusoidal b^*-axis dispersion. But perhaps a more likely explanation is that there are grains in the sample that are misoriented within the plane by 90°, so that as θ increases some grains could be rotating around the a-axis while other grains are rotating around the c-axis. If these different rotation directions have different angle-dependencies, then this could cause single peaks near $\theta = 0$ to split into multiple peaks at higher angles.

The LMTO calculations from the average structure do not reveal any FS sheets with areas close to those given by the α and γ frequencies. The α and γ frequencies must therefore be ascribed to portions of the reconstructed FS. Indeed, as described by Brouet and coworkers[10], the X pocket should be the only original FS sheet that is unmodified by the CDW. These dHvA measurements show that the reconstructed FS is quasi-2D with minimal b-axis dispersion. However, given the complexity of the original FS, it is difficult to ascribe these frequencies to particular FS sheets. Fig. 5.9 shows the FS of $CeTe_3$ (from Fig. 4.19(a)) translated by $q \approx \pm 2/7c^*$. Black lines indicate the portions of the ungapped FS that remain in the reconstructed FS. This

can be compared with Fig. 1.17(b) where the reconstructed FS is drawn for the tight-binding bands by Brouet *et al.* In comparison to the tight-binding FS, the LMTO FS shows additional complexity due to bilayer splitting and the same is true for their respective CDW-reconstructed Fermis surfaces.

The susceptibility data, with its low noise floor and high data density, is sensitive to high frequencies that might be obscured in the torque data. Given that no frequencies higher than γ were observed, apart from higher order harmonics, γ is mostly likely the largest sheet of the reconstructed FS. The splitting of γ from one peak to three peaks at higher angles, like the splitting of β_1 and β_2, can be attributed to either a complex b^*-axis dispersion or to crystal twinning.

The field dependence of each frequency can be extracted from the raw data by filtering the fourier transform. The torque data from Fig. 5.2 shown again in green in Fig. 5.8. The frequencies α, β and γ are individually extracted by filtering the fourier transform. A gaussian filter is centered around the desired frequency in the fourier transform, and a subsequent reverse fourier transform results in the filtered oscillations shown in Fig. 5.8. The raw data is predominantly characterized by the frequency β with its beating. The extracted α and γ show no beating, and their amplitude rises smoothly with an exponential dependence.

The mean-free path can be estimated by analyzing the exponential dependence of the oscillation amplitude with field. The exponent is proportional to C_F/l where C_F is the circumference of the orbit in k-space and l is the mean-free path. To solve for this exponent, the extracted β oscillations are fit to $A_0 e^{B_D/H}(A_1 \sin(\beta_1/H + \phi_1) + A_2 \sin(\beta_2/H + \phi_2))$ where A_1 and A_2 are the relative amplitudes of the β_1 and β_2 peaks in the fourier transform, respectively. A_0 is a constant, and B_D is the exponent of interest. The factors A_0 and B_D are allowed to vary alternately with the factors ϕ_1

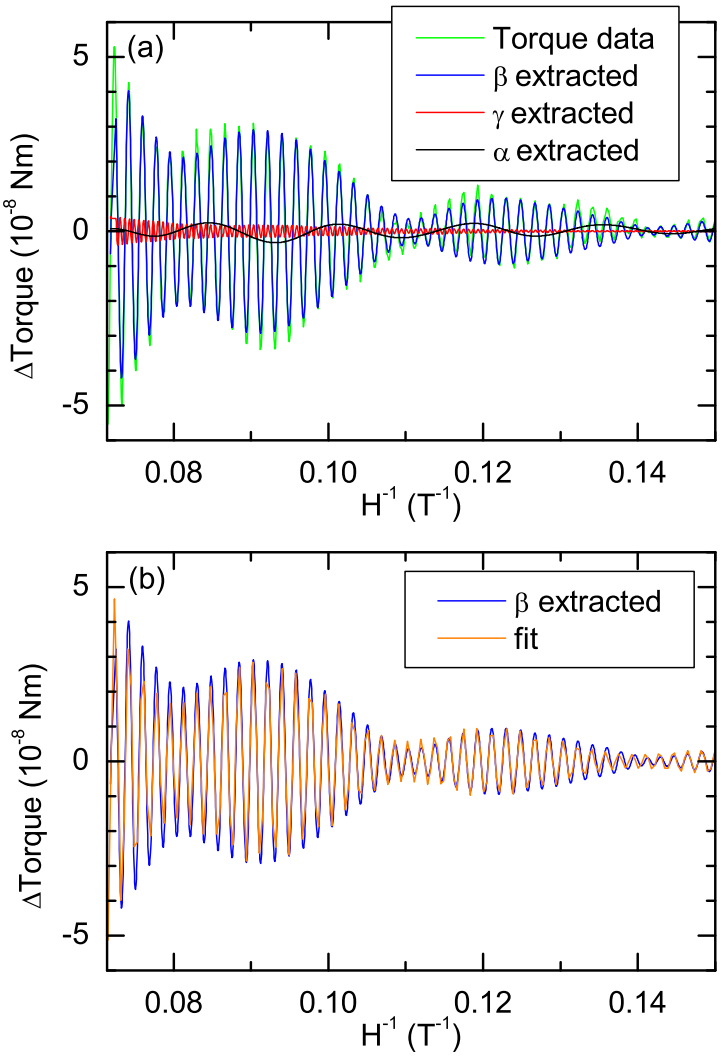

Figure 5.8: Individual frequencies extracted from the filtered fourier transform of a torque measurement of $LaTe_3$ at 2 K. (a) The extracted frequencies β (blue), γ (red), and α (black) plotted against the raw data (green). (b) The extracted frequency β oscillations (blue) and a fit to the oscillations (orange) as described in the text.

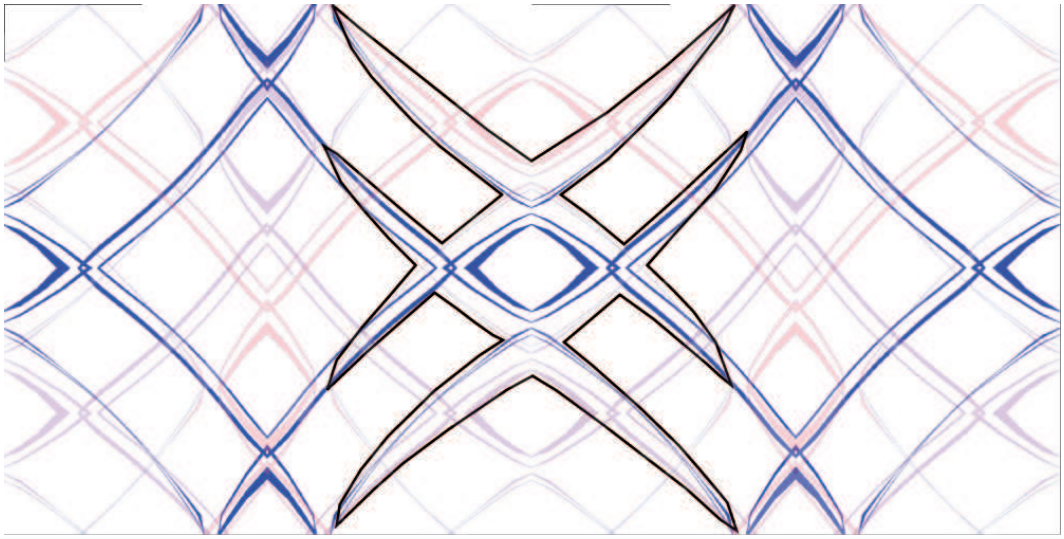

Figure 5.9: Two Brillouin zones of the FS for $CeTe_3$ as calculated by LMTO (from Fig. 4.19(a)). Each FS is translated by $q \approx \pm 2/7c^*$ (the c^* direction is vertical). The black lines indicate regions of the ungapped FS that contribute to the reconstructed FS.

and ϕ_2. Fig. 5.8 shows the extracted β oscillations along with the results of the fit, shown in orange. The extracted oscillations are well-characterized by this expression. From this fit, performed on several data sets for this sample, a exponent of $B_D = 39(3)$ T is obtained.

If β corresponds to the small oval pockets at X that are unmodified by CDW formation, the circumference of this orbit can be estimated from the area and the shape of this pocket. To estimate the circumference, X pocket is approximated as a diamond with the area as measured from dHvA. The resulting mean free path is 80±10 nm. Assuming that all sheets are characterized by the same mean free path, this value can in turn be used to estimate the C_F for γ orbit. The ratio of the estimated C_F (1.17 $(\mathring{A})^{-1}$) to the FS area (0.154 $(\mathring{A})^{-2}$) obtained from dHvA indicates that the γ orbit resembles a circle and does not have thin extended regions.

5.1.3 Conclusions

De Haas van Alphen measurements on $LaTe_3$ show three fundamental frequencies. A pair of frequencies β_1 and β_2 representing areas of 2.44% and 2.59% of the Brillouin zone, respectively, can be correlated with the unmodified X pocket of the FS from the average structure, a bilayer-split pocket which has been confirmed by ARPES to exist in the CDW state. The other frequencies—α, corresponding to 0.28% of the BZ and γ corresponding to 7.6% of the BZ—must result from FS sheets reconstructed by the CDW wavevector. These reconstructed FS sheets are quasi-2D and show very little b-axis dispersion.

5.2 Postscript: YTe_3

Preliminary measurements of YTe_3 in the MPMS also revealed quantum oscillations. The results are described here and implications for future experiments are discussed.

Fig. 5.10 shows the raw data of a YTe_3 crystal weighing 23.3 mg mounted on a plastic disk as described in Ch. 3. Data for increasing fields are shown in closed circles, while open circles indicate data taken for decreasing fields. A clear oscillatory signal is seen beginning at 1T, with higher frequencies becoming visible at 3T.

The fourier transform is shown in Fig. 5.11. The lowest frequency peak observed in the spectrum is at 6 T, which is the frequency of long wavelength oscillation seen in the raw data beginning at 1T. Other frequencies observed are at 27 and 71 T.

In Figure 5.12, a section of the data from 3–5 T is shown plotted versus inverse field. A polynomial background has been subtracted. At these fields, the 27 T frequency can be observed as a ripple over the longer wavelength 6 T frequency.

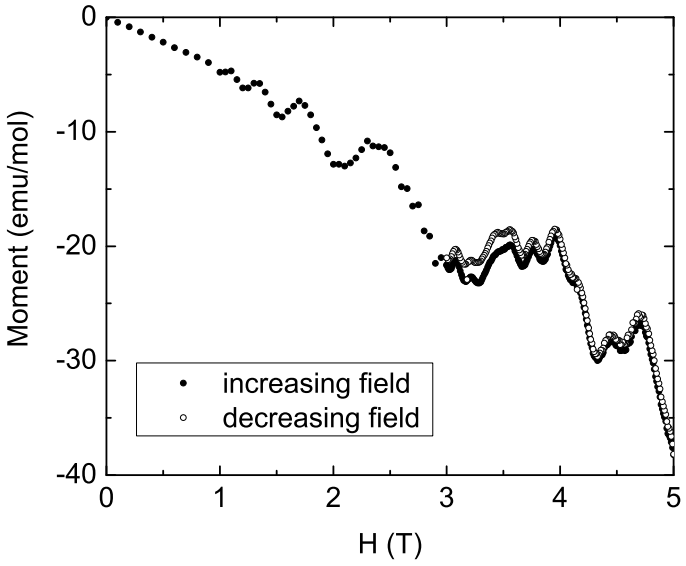

Figure 5.10: The susceptibility of YTe_3 showing dHvA oscillations. Data taken for increasing and decreasing fields.

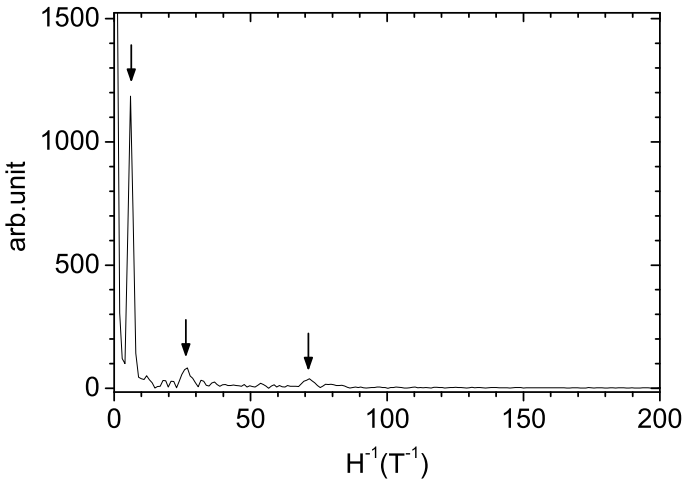

Figure 5.11: Fourier transform of YTe_3 susceptibility. Peaks in the fourier transform are at frequencies of 6T, 27T, and 71T.

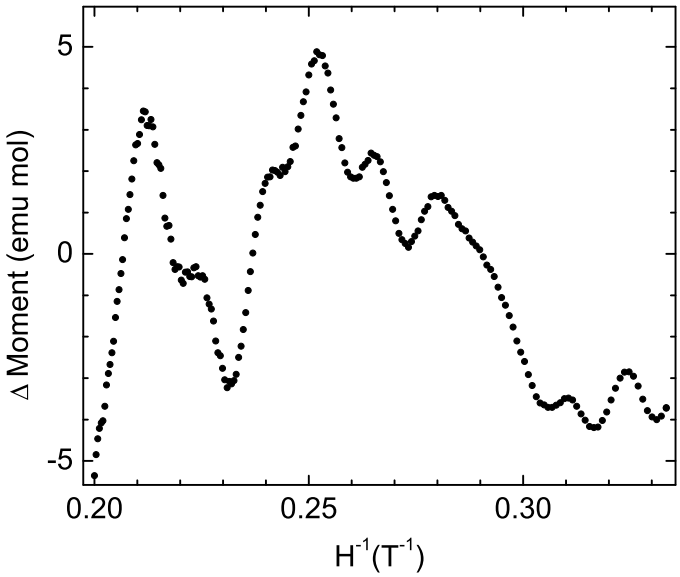

Figure 5.12: Susceptibility of YTe_3 with background subtracted, plotted as a function of inverse field.

DHva measurements of YTe_3 at higher fields could reveal higher frequency oscillations heretofore unseen in these preliminary measurements at 5T. The CDW transition temperature for YTe_3 (Fig. 4.4) is lower than that of $LaTe_3$ or $CeTe_3$, and ARPES measurements[10] correspondingly reveal that less of the Fermi surface is gapped than in $CeTe_3$. Areas for the reconstructed FS are expected to be quite different from those in $LaTe_3$. The X pocket for YTe_3 is also expected to be undisturbed by CDW formation. A detailed study of quantum oscillations in YTe_3 could highlight how FS reconstruction is affected by changes in chemical pressure and strength of CDW order parameter.

Chapter 6

Magnetic Properties

Thermodynamic and transport measurements show magnetic ordering of the rare earth ions in $R\mathrm{Te}_3$ at temperatures below approximately 12 K. These temperatures are much lower than those of the CDW transitions, and can, in general, be thought of as independent of the CDW ordering. However, results from high pressure experiments[41, 42, 43] show that the CDW transition temperatures in $R\mathrm{Te}_3$ can be suppressed upon application of external pressure, suggesting that the transitions could potentially be suppressed to be on the same energy scale as that of the magnetic ordering. The interplay (even competition) between these phases would be very interesting, motivating an initial study of the magnetic properties of $R\mathrm{Te}_3$ at ambient pressure. In this chapter I present a brief survey of the magnetic properties of $R\mathrm{Te}_3$.

Magnetization measurements for the nonmagnetic YTe_3 and LaTe_3 are presented, followed by results for the magnetic compounds R = Ce, Nd, Sm, Gd, Tb, Dy, Ho, Er. For each of the magnetic compounds, susceptibility and heat capacity measurements are presented illustrating antiferromagnetic order. Resistivity curves are presented for those compounds that show features near the Néel temperature T_N. The resistivity

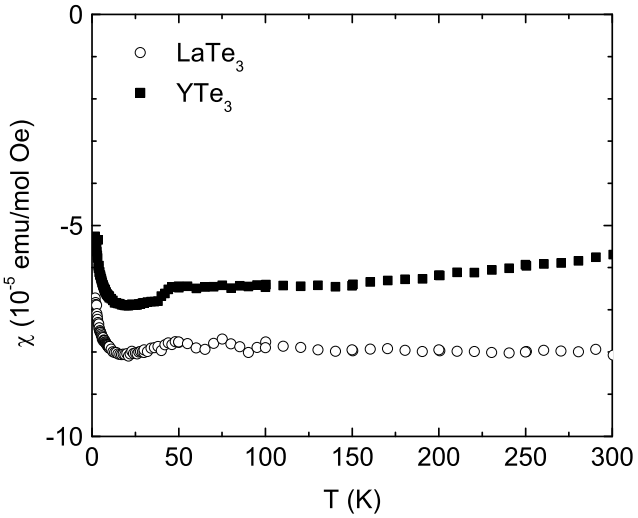

Figure 6.1: Magnetic susceptibility of YTe_3 and $LaTe_3$ for fields oriented in the *ac*-plane.

for $SmTe_3$ and $TbTe_3$ show a loss of spin-disorder scattering at T_N, while that for $DyTe_3$ shows evidence of superzone gapping. The resistivity for $CeTe_3$ shows Kondo behavior at low temperatures. The results for YTe_3, $LaTe_3$, and $CeTe_3$ are published in Ref. [23]. At the time of writing, a manuscript describing results for R = Y, Nd, Sm, Gd, Tb, Dy, and Ho is in preparation[44].

6.1 Nonmagnetic YTe_3 and $LaTe_3$

Susceptibilities for the nonmagnetic compounds YTe_3 and $LaTe_3$ were measured with a magnetic field oriented in the *ac*-plane. The magnetization of YTe_3 was measured using a 29.9 mg sample in a field of 5000 Oe, and that of $LaTe_3$ was measured using a 47.8 mg sample in a field of 1000 Oe. The resulting susceptibilities are shown in

Fig. 6.1 over the temperature range 1.8 to 300 K. These susceptibilities are diamagnetic and largely temperature-independent. Uncertainty in the measured value of the susceptibility, combined with uncertainty in the calculated contribution from core states, means that the Pauli paramagnetic contribution to the susceptibility cannot be reliably extracted from these measurements. However, the Pauli contribution is small enough so that the overall susceptibility remains diamagnetic, which consistent with the small density of states obtained from heat capacity measurements described in Sec. 1.2.7.

A weak contribution from magnetic impurities is observed at low temperatures, consistent with the starting purities of the rare earth elements (99.5%). The small feature at 50 K corresponds to trapped oxygen.

The magnetization measurement for YTe_3 was extended to 400 K for a 62 mg sample in a field of 5000 Oe lying in the *ac*-plane. The susceptibility is plotted in Fig. 6.2(b) along with (a) the resistivity curves in the same temperature range. (Full resistivity curves for YTe_3 shown in Fig. 4.4. The susceptibility of YTe_3 is less negative above the CDW transition than below, indicating that the larger density of states from the ungapped FS above the CDW transition leads to a greater Pauli paramagnetic contribution to the susceptibility. For the magnetic rare earths, these features is overwhelmed by the Curie susceptibility, described in Ch. 6.

6.2 Magnetic $R\mathbf{Te}_3$

Heat capacity and susceptibility measurements for R = Ce, Nd, Sm, Gd, Tb, Dy, Ho, Er are presented. Magnetic ordering is observed in each of these compounds, excepting $ErTe_3$, for which no transition was observed down to 1.8 K. Susceptibility

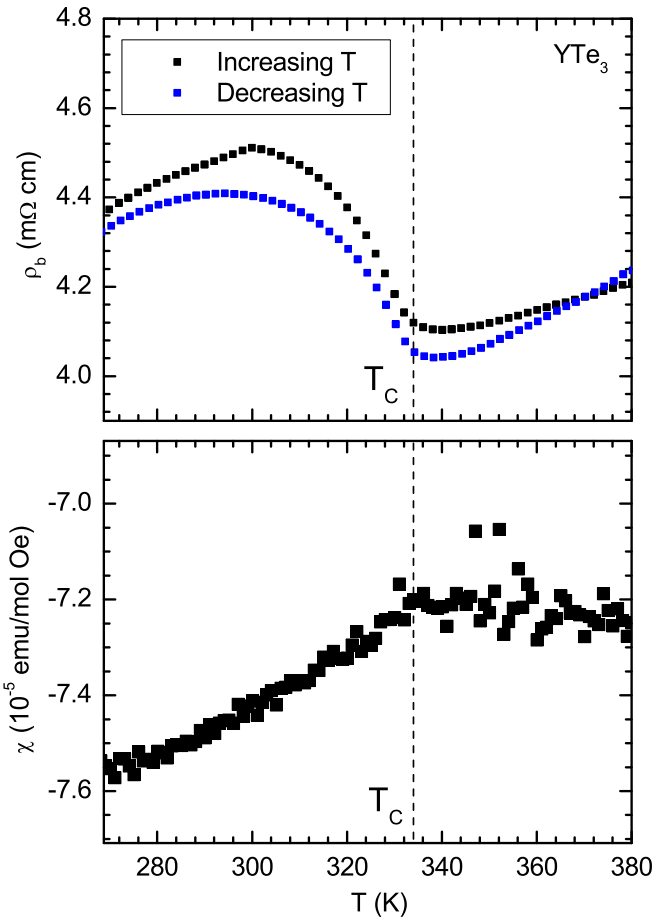

Figure 6.2: CDW transition in YTe_3 observed via (a) resistivity with currents aligned with the b-axis and (b) susceptibility with $H \| ac$. (Susceptibility data courtesy of Jiun-Haw Chu)

R	T_N	$\theta^{\|\|}$	$\theta^{\perp}$	θ^{poly}	$p_{eff}^{\|\|}$	$p_{eff}^{\perp}$	p_{eff}^{poly}	$p_{R^{3+}}$
Ce	3.0	-30.0	1.58	-6.77	2.46	2.39	2.41	2.54
Pr	–	(-23.7)	(-12.0)		(3.68)	(3.67)		3.58
Nd	2.57, 2.64	-21.3	-3.01	-8.26	3.59	3.54	3.56	3.62
Sm	2.18, 2.6	-29.2	-7.92	-11.9	1.00	0.50	0.76	0.85
Gd	9.7, 11.3	-15.3	-15.3	-15.3	7.77	7.77	7.77	7.94
Tb	5.32, 5.51, 5.75	-24.0	-5.32	-9.66	10.1	9.83	9.88	9.72
Dy	3.44, 3.6	-6.60	-5.26	-5.26	10.8	10.5	10.6	10.63
Ho	2.92, 3.25	-0.64	7.84	-4.13	10.3	10.1	10.2	10.60
Er	< 1.8	-3.33	-0.19	-1.2	9.38	9.17	9.24	9.59

Table 6.1: Magnetic order in $R\mathrm{Te}_3$. Néel temperatures are from heat capacity measurements. In cases where multiples transitions were observed, each distinct peak is listed. Weiss temperatures θ and effective moments p_{eff} from Curie-Weiss fits are shown for orientations H $||b$ and H $\|ac$ plane, and for the polycrystalline average. Values for Pr are reproduced from Ref. [22]. The calculated value of $p = \mu_{eff}/\mu_B = g_J[J(J+1)]^{1/2}$ for each rare earth ion R^{3+} is shown in the last column for comparison.

results are fit to the Curie-Weiss model. Resistivity measurements are presented for R = Ce, Sm and Tb which show a loss of spin-disorder scattering at T_N, and for R = Dy which is indicative of superzone gapping. The low-temperature resistivity for CeTe_3 also shows Kondo behavior.

6.2.1 Results

Features indicative of magnetic ordering were observed in susceptibility and heat capacity measurements, with many of the compounds showing a cascade of phase transitions at T_N. Values for T_N listed in Table 6.1 are those as obtained from heat capacity measurements for which the multiple phase transitions are more clearly observed. The transition temperatures range from a maximum of 11.3 K for GdTe_3 down to 2.18 K for SmTe_3. No transitions were observed for ErTe_3 down to 1.8 K. Measurements by Iyeiri *et al.* report that PrTe_3 has a nonmagnetic singlet ground state due to the crystal electric field (CEF).[22].

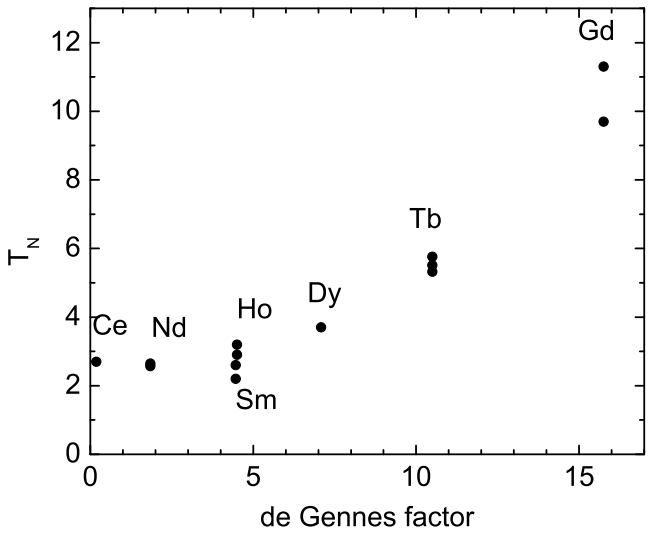

Figure 6.3: The Néel temperatures are plotted against the de Gennes factor $(g_J - 1)^2 J(J+1)$.

Néel temperatures for the compounds that exhibit a transition above 1.8 K are plotted in Fig. 6.3 against the de Gennes factor, $(g_J - 1)^2 J(J+1)$ where g_J is the Landé g-factor. Where multiple transitions were found, each transition temperature is plotted separately. The departure of T_N from a linear dependence on the de Gennes factor can be attributed to the effects of crystal field (CEF) on the Hund's rule multiplet. No measurements were made for $TmTe_3$, but as the de Gennes factor of Tm^{3+} is 1.17, its T_N is expected to near those of $CeTe_3$ and $NdTe_3$.

The susceptibility of each compound was measured in an applied field of 1000 Oe from 0 to 300 K. Data was taken in two magnetic field orientations - $H \| b$ and H along an arbitrary direction in the *ac*-plane. The polycrystalline average, given by $\chi_{poly} = (\chi_b + 2\chi_{ac})/3$, was also calculated for each compound.

The inverse susceptibility is plotted for R = Ce, Nd, Sm, Gd, Tb, Dy, Ho, and

Er in panels (a) of Figs. 6.4-6.11. Data are shown for each field orientation and for the polycrystalline average. Above the Néel transition, a linear fit is performed to the Curie-Weiss model. The values for the Weiss temperature θ and the effective moment p_{eff} derived from these fits are shown in Table 6.1. (Values for $PrTe_3$ shown in Table 6.1 are those from Ref. [22].) For each compound, the data is fit over the range 100 - 300 K the Curie-Weiss law, except in the cases of $CeTe_3$ (fit over the range 150-300 K) and $SmTe_3$ (described below). The effective moments p_{eff} are fairly close to the calculated values $p_{R^{3+}}$ for the rare earth ions, also shown in Table 6.1. Weiss temperature are generally negative, indicating predominantly antiferromagnetic interactions.

Unlike for other rare earths, the inverse susceptibility of $SmTe_3$ (Fig. 6.6)(a) is nonlinear. In Sm the energy between the ground state J multiplet ($J = 5/2$) and the first excited state ($J = 7/2$) is smaller than that for other rare earths[7] and thermal population of this excited Hund's rule state leads to departures from Curie-Weiss behavior. Nevertheless, the fit to Curie-Weiss parameters at low temperature (6 to 15 K) can be used to estimate the effective moment. The resulting $p_{eff} = 0.76$ for the polycrystalline average is still quite close to the calculated $p = 0.85$ for Sm.

Nearly all the compounds exhibit anisotropy between the two orientations as observed in the values for p_{eff} and θ, which can be attributed to CEF, excepting $GdTe_3$. There is no CEF splitting of the Hund's rule ground state for $GdTe_3$ as $L = 0$ for Gd.

The magnetization of each compound was measured at 1.8 K in an applied field of 0 to 5 T for both in the in-plane and out of plane orientations. The results of these measurements for R = Ce, Nd, Sm, Gd, Tb, Dy, Ho, and Er are shown in panels (b) of Figs. 6.4-6.11. For most of the compounds, there is slight anisotropy between the two orientations, which is attributed to the influence of CEF. The orientation with

the larger valued moment, also known as the easy axis, is in the in-plane direction for all measured compounds. Many of the compounds show metamagnetic transitions - $NdTe_3$ at 2.5 T for $H\|ac$, $GdTe_3$ at 2 T for $H\|\|b$, $TbTe_3$ at 2 T for $H\|ac$, and $DyTe_3$ at 1 T for both orientations.

Heat capacity measurements are shown for $R =$ Ce, Nd, Sm, Gd, Tb, Dy, and Ho in panels (c) of Figs. 6.4-6.10. The heat capacity is plotted in filled circles and referenced to the left axis. For comparison, the heat capacity data for the non-magnetic analogue $LaTe_3$ is plotted alongside, in open circles, to show the phonon contribution to the heat capacity. The magnetic ordering is clearly seen as a second-order transition rising above the phonon background. The Néel transition often consists of multiple distinct peaks. For $NdTe_3$ and $DyTe_3$, just above the Néel transition is a gentle rise from a Schottky anomaly associated with CEF splitting of the Hund's rule multiplet.

The magnetic contribution to the entropy, S_{mag}, can be estimated by subtracting the heat capacity of $LaTe_3$, and then integrating C_p/T over temperature. S_{mag} is plotted in each figure as a solid line, referenced to the right axis. For reference, Rln(2J+1), the entropy for free spins of magnitude J, is shown as a dotted line (right axis). Values of J for the Hund's rule groundstate are shown in Table 1.1. For all of the compounds excepting $GdTe_3$, S_{mag} falls short of this value, indicating the presence of additional CEF splitting on a temperature scale greater than 30 K. For $GdTe_3$, there is no CEF splitting of the Hund's rule ground state, and as a result S_{mag} rises to the full value of $R\ln(2J+1)$. The magnetic entropy for $CeTe_3$ rises to $R\ln 2 =$ 5.76 J/molK just above T_N, indicating a doublet ground state, as previously proposed by Iyeiri and co-workers to account for their susceptibility data [22] and commonly found for Ce in a low point symmetry.

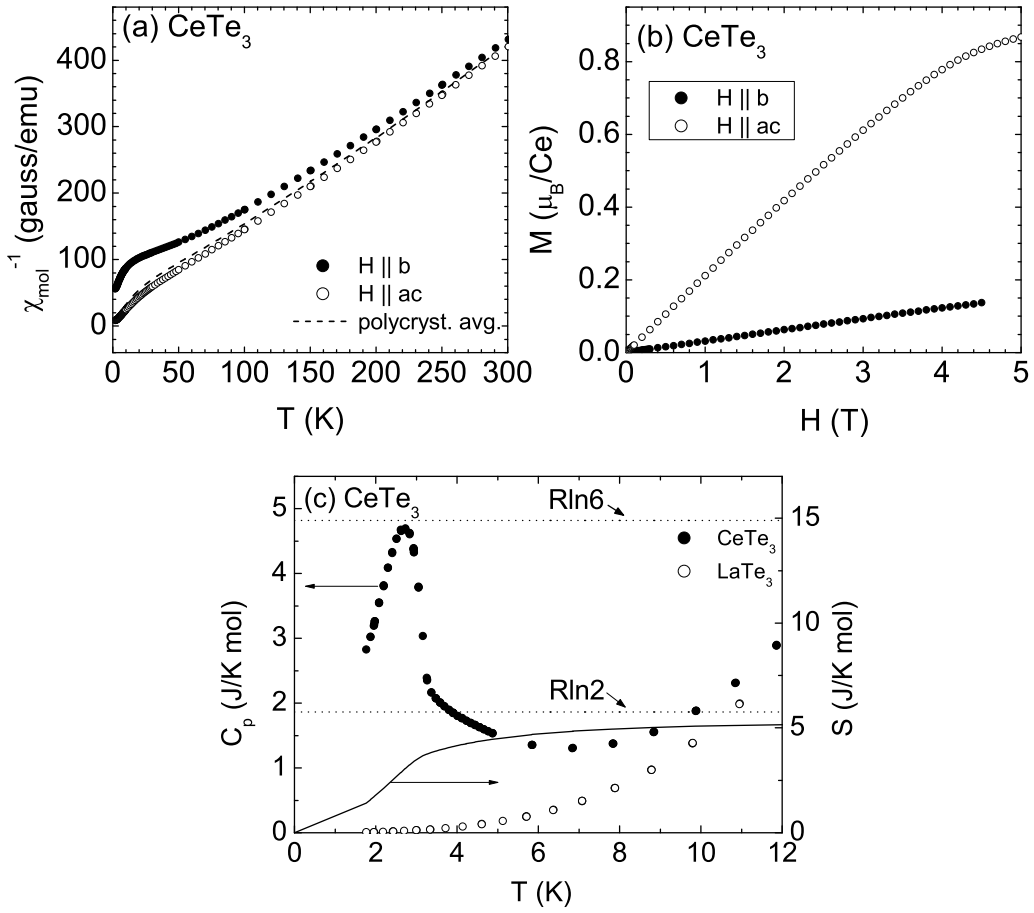

Figure 6.4: $CeTe_3$. (a)The inverse susceptibility of $CeTe_3$ in an applied field of 1000 Oe is shown for $H||b$-axis (filled circles) and for H lying in an arbitrary direction in the ac plane (open circles). The dashed line shows the polycrystalline average. (b) The magnetization of $CeTe_3$ at 1.8 K is plotted as a function of field for $H||b$ (filled circles) and $H\|ac$ (open circles). (c) The magnetic contribution to the heat capacity of $CeTe_3$ (filled circles left axis) and that of the non-magnetic analogue $LaTe_3$ (open circles, right axis), and the magnetic entropy (right axis). Dashed lines show $Rln6$ and $Rln2$ (right axis).

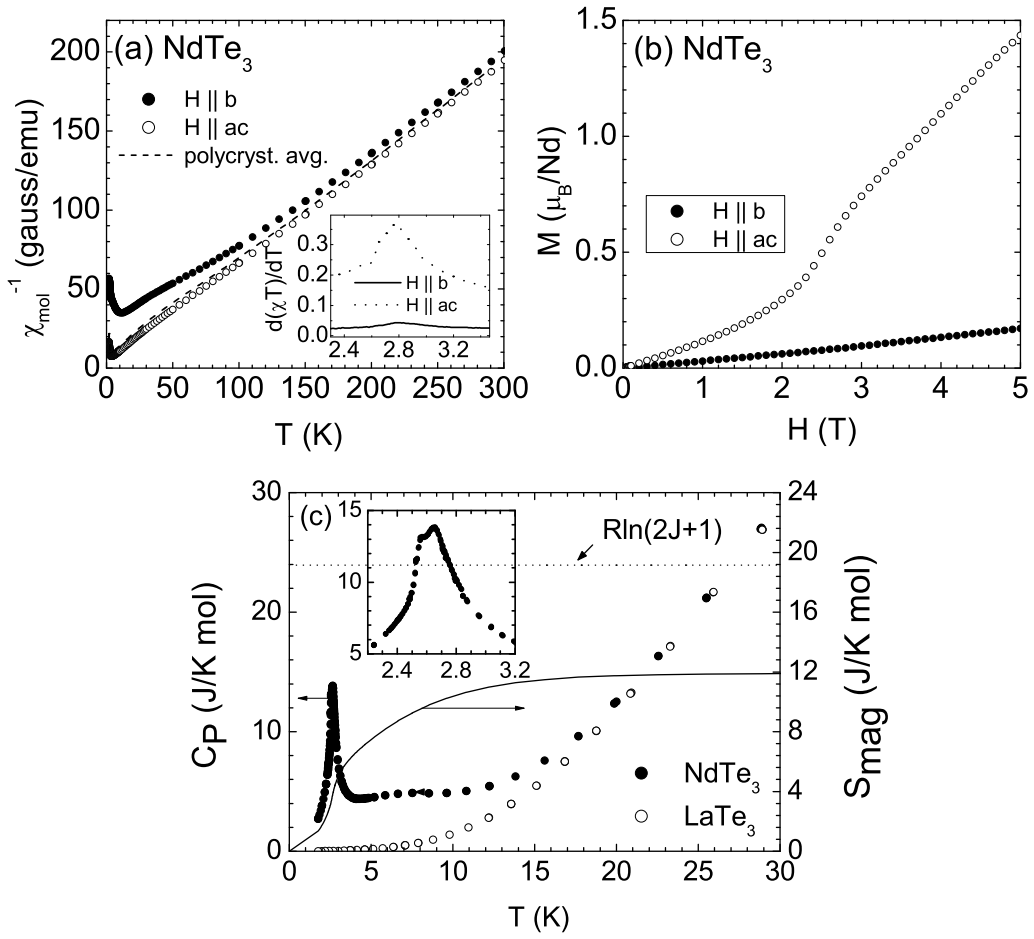

Figure 6.5: $NdTe_3$. (a)The inverse susceptibility of $NdTe_3$ in an applied field of 1000 Oe is shown for $H||b$-axis (filled circles) and for H lying in an arbitrary direction in the ac plane (open circles). The dashed line shows the polycrystalline average. (b) The magnetization of $NdTe_3$ at 1.8 K is plotted as a function of field for $H||b$ (filled circles) and $H\|ac$ (open circles). (c)Specific heat for $NdTe_3$ (filled circles, left axis) and that of the non-magnetic analogue $LaTe_3$ (open circles, left axis). The magnetic entropy S_{mag} (solid line) and Rln(2J+1) (dashed line) are shown (right axis).

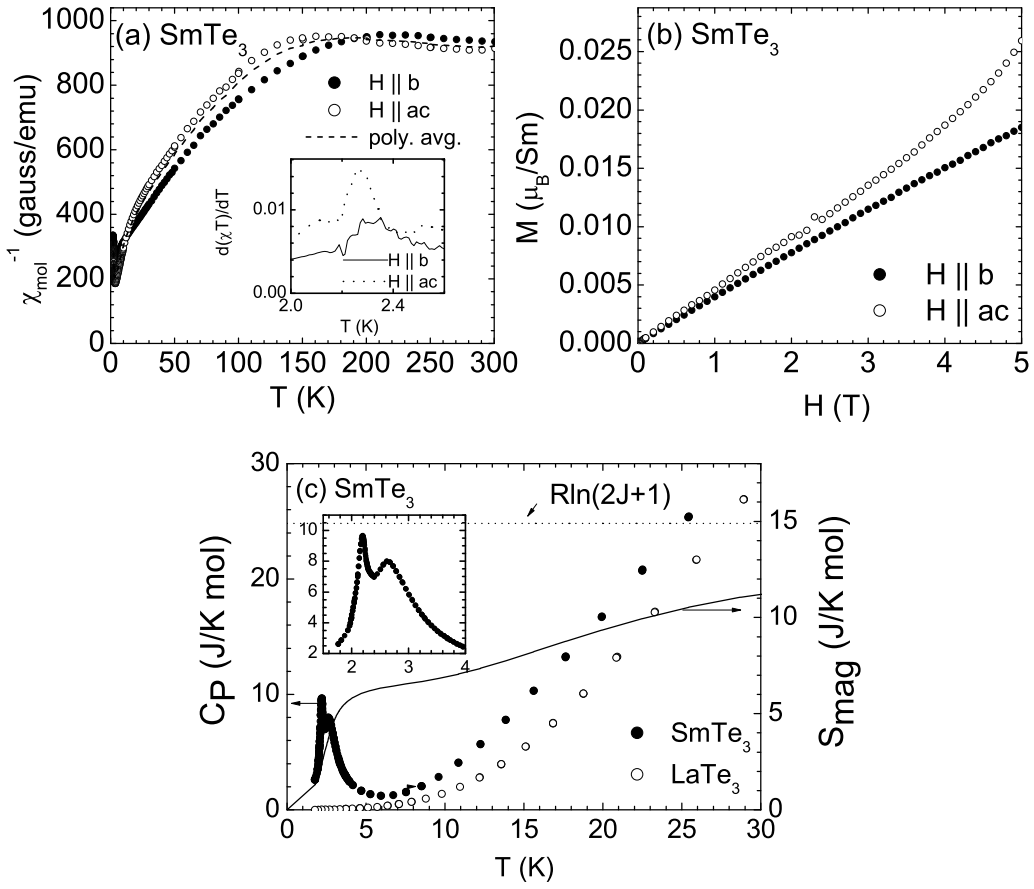

Figure 6.6: $SmTe_3$. (a)The inverse susceptibility of $SmTe_3$ in an applied field of 1000 Oe is shown for $H||b$-axis (filled circles) and for H lying in an arbitrary direction in the ac plane (open circles). The dashed line shows the polycrystalline average. (b) The magnetization of $SmTe_3$ at 1.8 K is plotted as a function of field for $H||b$ (filled circles) and $H\|ac$ (open circles). (c)Specific heat for $SmTe_3$ (filled circles) and that of the non-magnetic analogue $LaTe_3$ (open circles) are shown referenced to the left axis. The magnetic entropy S_{mag} (solid line) and Rln(2J+1) (dashed line) are shown referenced to the right axis.

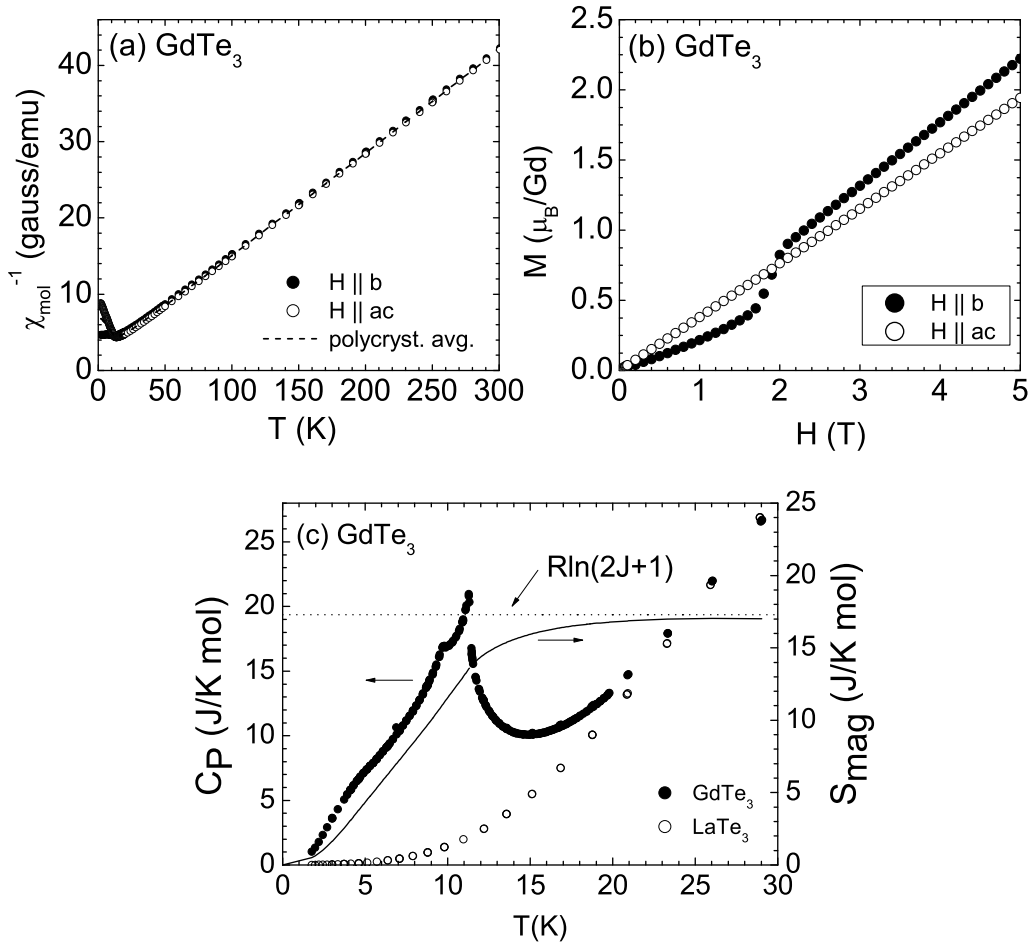

Figure 6.7: $GdTe_3$.(a)The inverse susceptibility of $GdTe_3$ in an applied field of 1000 Oe is shown for $H||b$-axis (filled circles) and for H lying in an arbitrary direction in the ac plane (open circles). The dashed line shows the polycrystalline average. (b) The magnetization of $GdTe_3$ at 1.8 K is plotted as a function of field for $H||b$ (filled circles) and $H\|ac$ (open circles) (c) Specific heat for $GdTe_3$ (filled circles) and that of the non-magnetic analogue $LaTe_3$ (open circles) are shown referenced to the left axis. The magnetic entropy S_{mag} (solid line) and Rln(2J+1) (dashed line) are shown referenced to the right axis.

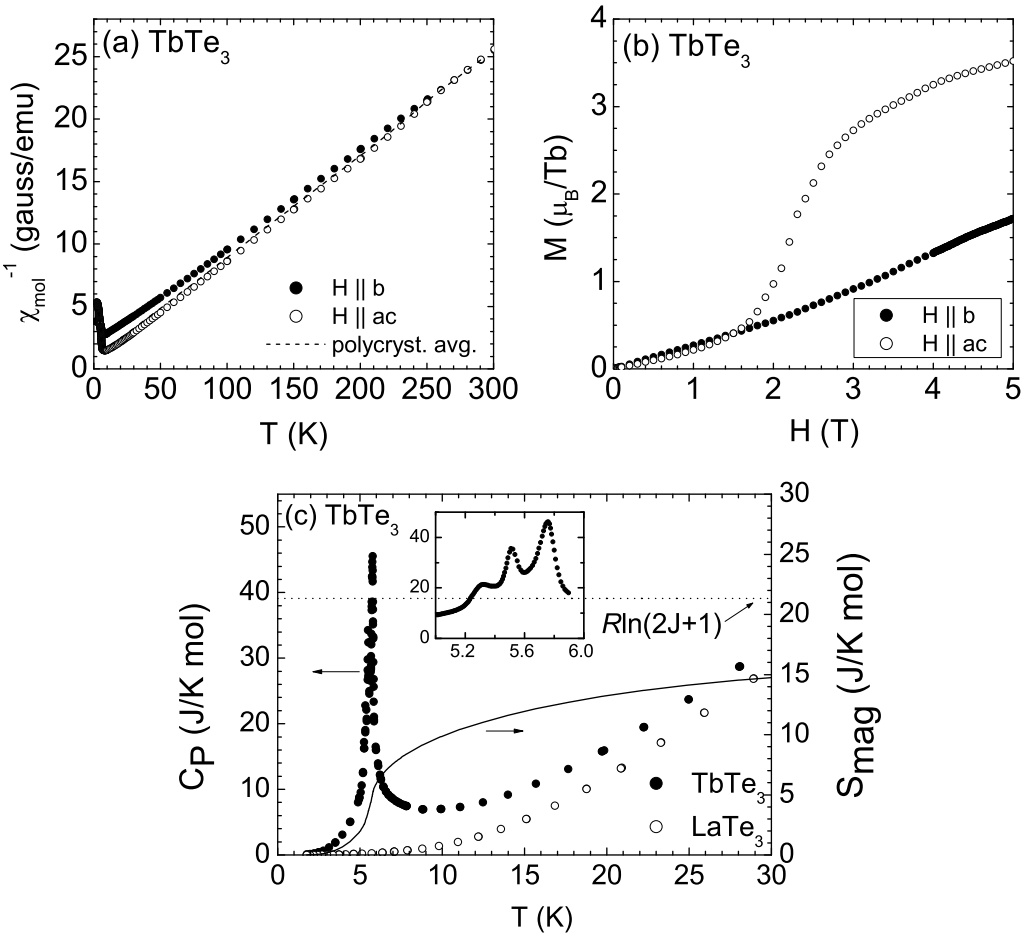

Figure 6.8: $TbTe_3$. (a)The inverse susceptibility of $TbTe_3$ in an applied field of 1000 Oe is shown for $H||b$-axis (filled circles) and for H lying in an arbitrary direction in the ac plane (open circles). The dashed line shows the polycrystalline average. (b) The magnetization of $TbTe_3$ at 1.8 K is plotted as a function of field for $H||b$ (filled circles) and $H\|ac$ (open circles). (c)Specific heat for $TbTe_3$ (filled circles) and that of the non-magnetic analogue $LaTe_3$ (open circles) are shown referenced to the left axis. The magnetic entropy S_{mag} (solid line) and Rln(2J+1) (dashed line) are shown referenced to the right axis.

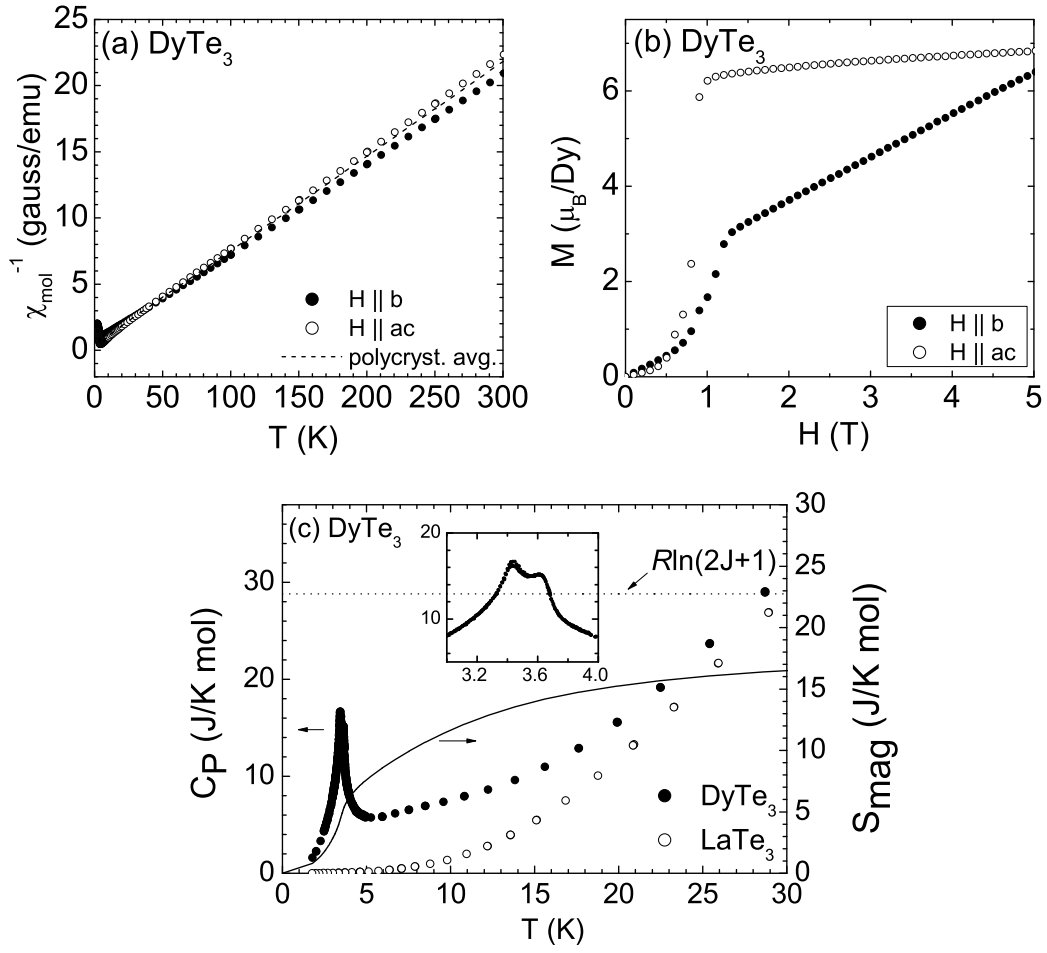

Figure 6.9: $DyTe_3$. (a)The inverse susceptibility of $DyTe_3$ in an applied field of 1000 Oe is shown for $H||b$-axis (filled circles) and for H lying in an arbitrary direction in the ac plane (open circles). The dashed line shows the polycrystalline average. (b) The magnetization of $DyTe_3$ at 1.8 K is plotted as a function of field for $H||b$ (filled circles) and $H\|ac$ (open circles). (c)Specific heat for $DyTe_3$ (filled circles) and that of the non-magnetic analogue $LaTe_3$ (open circles) are shown referenced to the left axis. The magnetic entropy S_{mag} (solid line) and Rln(2J+1) (dashed line) are shown referenced to the right axis.

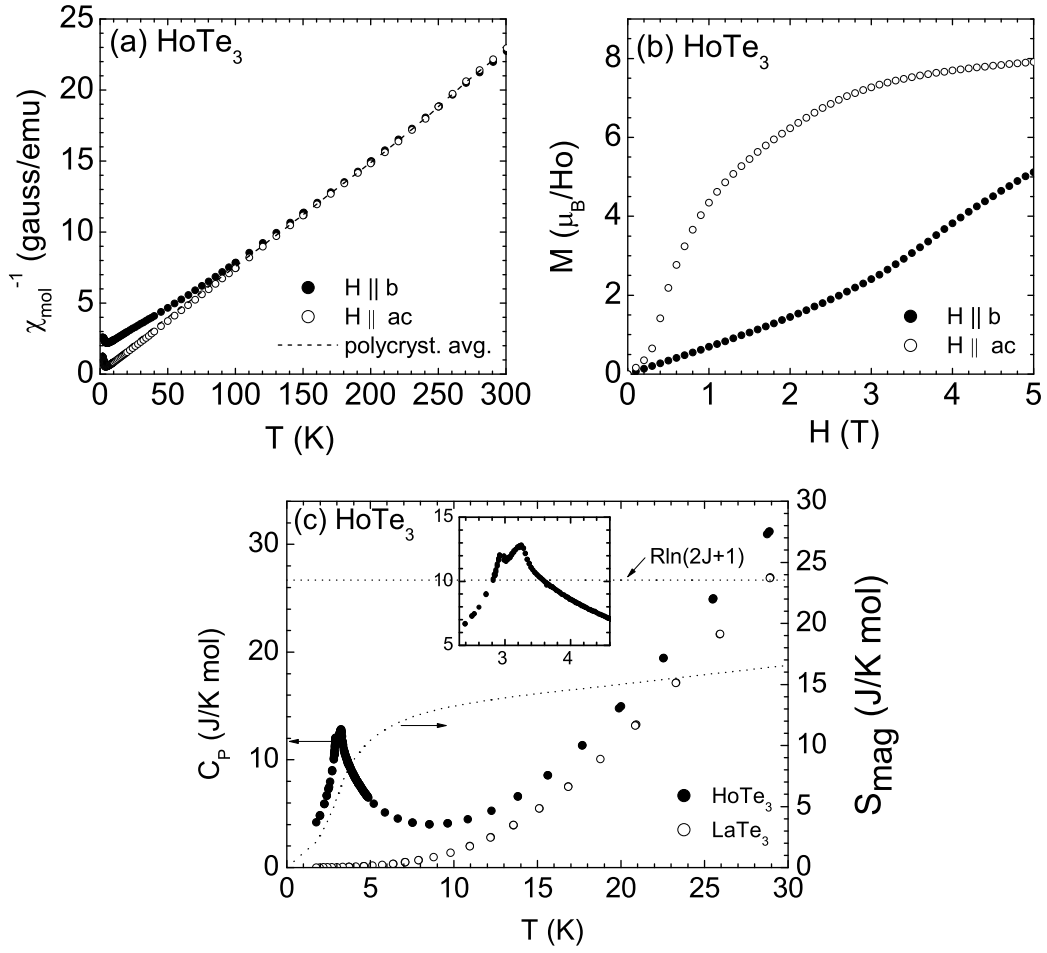

Figure 6.10: $HoTe_3$.(a)The inverse susceptibility of $HoTe_3$ in an applied field of 1000 Oe is shown for $H||b$-axis (filled circles) and for H lying in an arbitrary direction in the ac plane (open circles). The dashed line shows the polycrystalline average. (b) The magnetization of $HoTe_3$ at 1.8 K is plotted as a function of field for $H||b$ (filled circles) and $H\|ac$ (open circles). (c)Specific heat for $HoTe_3$ (filled circles) and that of the non-magnetic analogue $LaTe_3$ (open circles) are shown referenced to the left axis. The magnetic entropy S_{mag} (solid line) and Rln(2J+1) (dashed line) are shown referenced to the right axis.

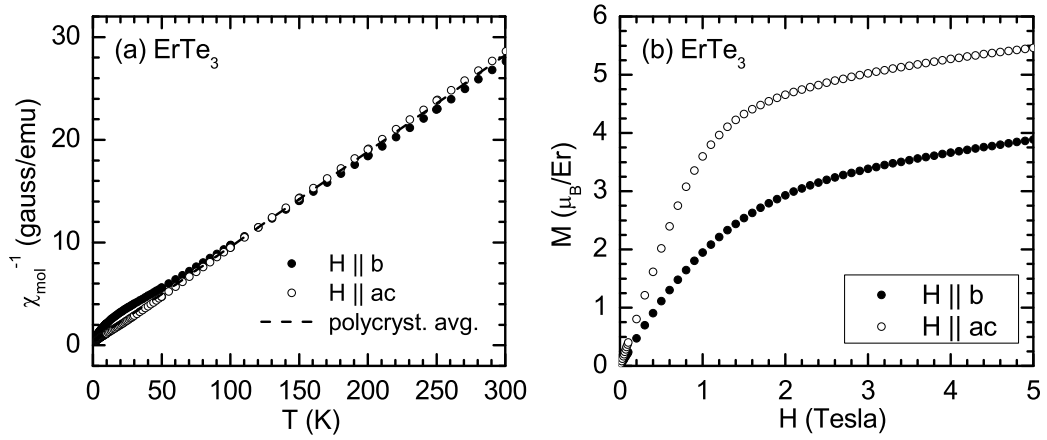

Figure 6.11: $ErTe_3$.(a)The inverse susceptibility of $ErTe_3$ in an applied field of 1000 Oe is shown for $H||b$-axis (filled circles) and for H lying in an arbitrary direction in the ac plane (open circles). The dashed line shows the polycrystalline average. (b) The magnetization of $ErTe_3$ at 1.8 K is plotted as a function of field for $H||b$ (filled circles) and $H\|ac$ (open circles)

The Néel transition as observed in resistivity

The resistivity for $CeTe_3$ is shown in Figure 6.12. No CDW transitions were observed up to 300 K. For currents flowing in the ac-plane, the resistivity has a weak minimum centered at approximately 10 K. As the temperature is reduced from this value the resistivity rises to a broad maximum centered at approximately 6 K, before gradually decreasing in magnitude again. Finally, at 2.8 K there is a sharp drop in the resistivity associated with the loss of spin-disorder scattering at T_N. This feature is seen more clearly in the derivative $d\rho/dT$, which is plotted in the inset to Figure 6.12 along with the derivative of the susceptibility $d\chi T/dT$. Similar data for currents flowing in the b-axis direction also show the loss of spin-disorder scattering at T_N but otherwise appear to have a weaker temperature dependence below 10 K, such that the resistivity

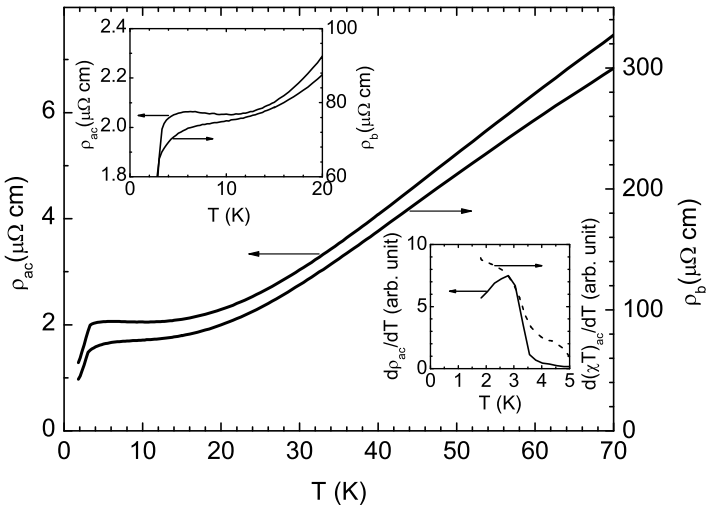

Figure 6.12: Representative resistivity data for $CeTe_3$ for currents flowing in the ac-plane (left axis) and along the b-axis (right-axis). Insets show (top) low-temperature behavior and (bottom) the Néel transition as seen in $d\rho/dT$ and $d\chi T/dT$.

exhibits more of a change in downward slope than a true upturn.

Below 10 K the resistivity of $CeTe_3$ shows a mild upturn is suggestive of weak Kondo behavior. In this case, the broad maximum in the resistivity centered at approximately 6 K is associated with a coherence temperature of the Kondo lattice. ARPES data [10, 18] show a non-dispersing feature 0.3 eV below E_F associated with the Ce $4f$ levels, consistent with such a scenario. Given the low value of T_N it is difficult to say whether there is any enhanced electronic contribution to the heat capacity at low temperatures, but the smallness of the resistivity anomaly suggests there will be minimal effect.

The full resistivity curve for $SmTe_3$ showing the CDW transition was shown in Fig. 4.1. Here, in Fig. 6.13, the closeup of the in-plane resistivity at low temperatures shows a loss of spin-disorder scattering at the Néel temperature. The heat capacity

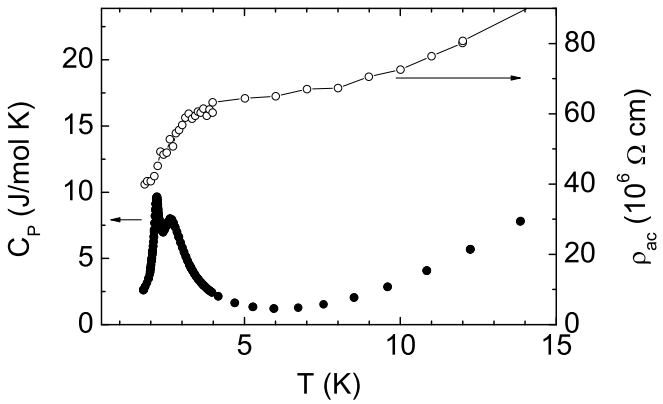

Figure 6.13: The in-plane resistivity for $SmTe_3$ (right axis, open circles) shows a loss of spin-disorder scattering T_N. The specific heat is plotted alongside (left axis, closed circles) for comparison.

curve for $SmTe_3$ is plotted alongside to highlight T_N.

The three transitions in $TbTe_3$ are highlighted in Fig 6.14. The magnetic contribution to the specific heat, C_{mag}, is plotted in filled circles, referenced to the left axis. These peaks are also clearly seen in the derivative $d\chi/dT$ of the susceptibility, which is shown for two orientations, referenced to the right axis. The dotted line shows H $\parallel$ b, and the solid line shows H lying in an arbitrary direction in the ac plane. There is a very slight (0.3 K) difference between the two measurements which most likely reflects systematic error in the thermometry. The resistivity of $TbTe_3$ for currents along the b-axis is shown in Fig 6.14(b)(left axis). The resistivity drops as the temperature is lowered through the Néel transition, which can be attributed to a loss of spin-disorder scattering. The triple peaks are subtle corrugations that are seen more clearly in the derivative $d\rho/dT$, which is shown as a line referenced to the right axis.

In contrast, the resistivity of $DyTe_3$ for currents along the b axis shows an upturn

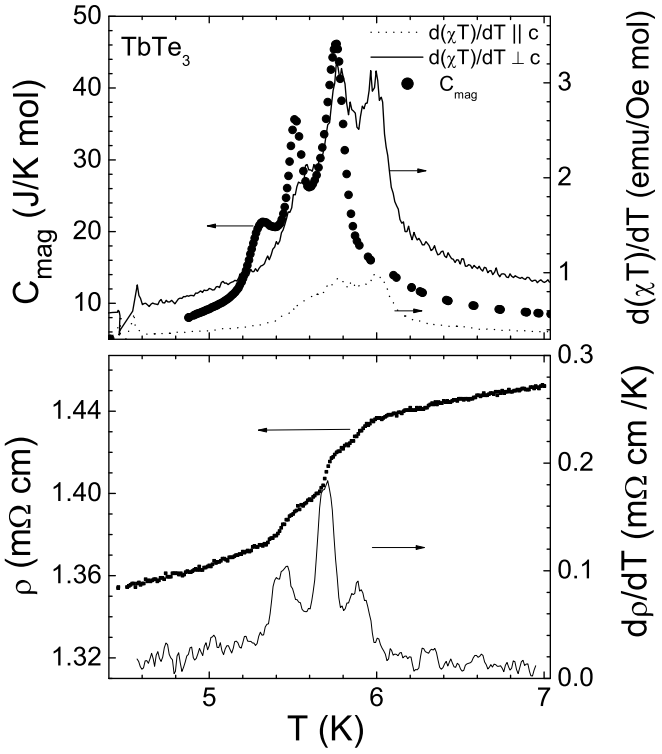

Figure 6.14: $TbTe_3$. (a) The magnetic contribution to head capacity (left, and the derivative of the susceptibility d(χ)/dT (right.) (b) The resistivity along the *b*-axis (left), with its derivative dρ/dT(right).

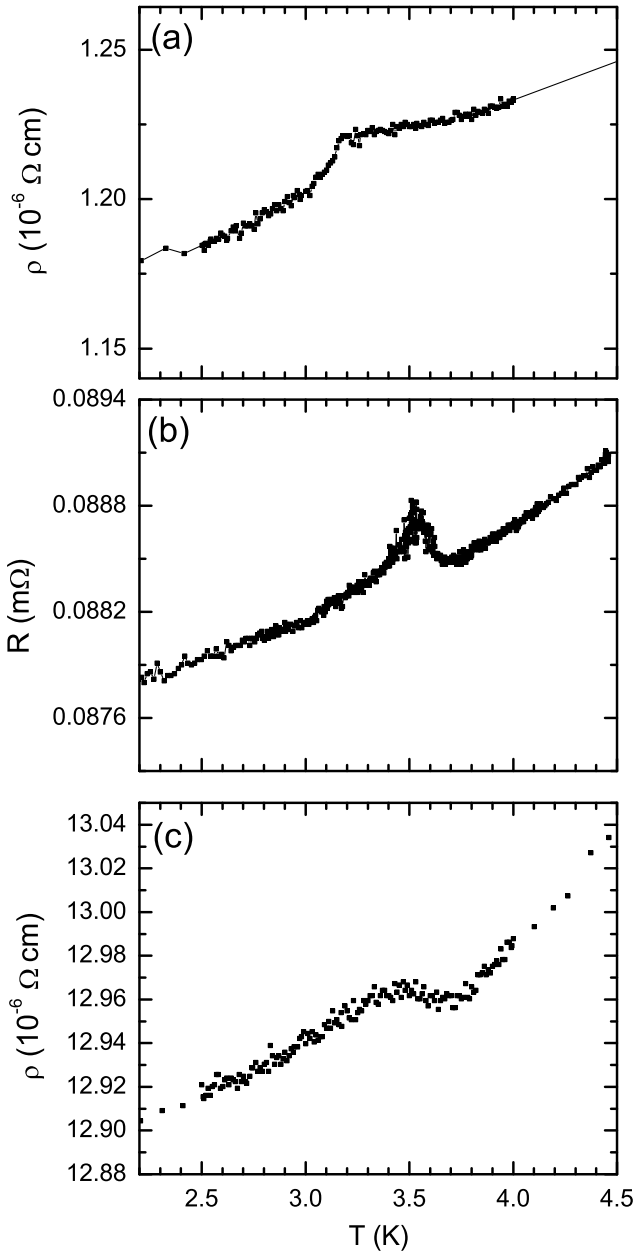

Figure 6.15: The resistivity of $DyTe_3$ for three different crystals showing evidence of superzone gap formation at the Néel temperature. Currents are oriented along the b-axis. ($T_N \sim 3.44$ and 3.6 K as observed for heat capacity measurements.) Data in (b) courtesy of D. Mann.

at the Néel temperature, as shown in Figure 6.15. This is evidence of the formation of a superzone gap, in which the magnetic ordering wavevector gaps parts of the Fermi surface and increasing the resistivity. As the Fermi surface at this temperature has already been gapped twice by two CDW wavevectors, this magnetic ordering constitutes a third nesting of the Fermi surface. Experiments to determine the magnetic ordering wavevector are underway.

Chapter 7

Conclusions and Future Directions

While many of the $R\mathrm{Te}_3$ compounds have been known to form a CDW with wave vector $q_1 \approx 2/7\ c^*$[12, 16], the transition temperatures had not yet been investigated. In this thesis, I present results for the CDW transition temperatures across the $R\mathrm{Te}_3$ series, and show that these compounds possess a remarkable phase diagram that is sensitive to small changes in chemical pressure.

Indications of the CDW transitions were first seen in the resistivity data, where compounds R = Y, Sm, Gd, and Tb were found to have a single CDW-like feature whereas the compounds with R = Dy, Ho, Er, and Tm were found to have two such features. High-resolution x-ray measurements were performed for TbTe_3 as a representative of compounds with one transition, and by following the q_1 superlattice modulation as a function of temperature these measurements show that the feature observed in the resistivity data is indeed the CDW transition temperature T_{c1}. High resolution x-ray measurements for ErTe_3, a compound with two features in resistivity, show that the higher temperature feature corresponds with the CDW transition temperature T_{c1} with wavevector q_1, while the lower feature at T_{c2} corresponds to the

onset of a second CDW with wavevector $q_2 \approx 1/3\ a^*$, in the in-plane direction perpendicular to q_1. Preliminary x-ray measurements for $HoTe_3$ also show a superlattice wavevector along a^* for temperatures below T_{c2}[29]. Given the known similarities of the q_1 CDW state for the various $R\mathrm{Te}_3$ compounds, and the monotonic dependence of T_{c1} and T_{c2} across the series, it can be extrapolated that the resistivity features observed for the other compounds also correspond to the CDW transition temperatures T_{c1} and T_{c2}.

As the electronic structure is very similar across the $R\mathrm{Te}_3$ series, it is surprising that such large variance is observed in the CDW transition temperatures. The transition temperature T_{c1} varies by over 200 K across the series, while the second transition temperature T_{c2} rises from nonexistent to 185 K. The large variation in T_{c1} is principally ascribed to the variation in the density of states at the Fermi level $n(E_F)$ due to the effect of chemical pressure via rare earth substitution. As T_{c1} decreases, increasingly more of the remaining FS becomes available to drive a second CDW with a modulation wave vector transverse to the first.

The resulting "rectangular" CDW state consists of perpendicular modulation wave vectors almost equal in magnitude, but with independent order parameters, each developed to a different degree at any given temperature. This exquisite degree of control of a physical parameter directly affecting the transition temperature, in conjunction with the remarkable simplicity of the "stripe" and "rectangular" CDW states, mark the rare earth tritellurides as a model system for studying the effects of imperfect FS nesting on CDW formation.

By preparing samples with a continuous solid solution between adjacent rare earths in the lanthanide series it would be possible to continuously tune the lattice parameter from that of $LaTe_3$ to that of $TmTe_3$ while retaining the same band

filling. Alloying between $DyTe_3$ and $TbTe_3$ could suppress the CDW to the Néel temperatures with the result of possible competition between CDW and magnetic order. Alloying in the direction of Yb and Lu and could decrease T_{c1} and increase T_{c2} until the two transition temperature converge, at which point both lattice modulations would occur simultaneously at the same critical temperature. This would result in a CDW state with checkerboard symmetry, albeit one with wavevectors different than those postulated by Yao et al[11].

Additionally, while chemical pressure can act similarly to external pressure, as has been observed for optical conductivity measurements[41], there are subtle ways in which these two tuning parameters may not be entirely equivalent for the $R\mathrm{Te}_3$ system. Rare-earth substitution would be expected to have a larger effect on expanding the R-Te block layer than on increasing the separation between the double Te planes. This may have subtle effects on the bilayer splitting of the FS of the unmodulated structure, and on the degree to which it can be nested by CDW wavevectors. The extent to which chemical and external pressure are equivalent can be explored with further high pressure experiments. Preliminary studies in resistivity[42] and x-ray diffraction[43] show that the transition temperature for the first CDW can be suppressed on the application of external pressure, leading to the postulate that external pressure can be used in conjunction with chemical pressure to compress the system to the proposed checkerboard state. The application of external pressure could also result in the complete suppression of the CDW state, potentially leading to other interesting ground states such as superconductivity.

This thesis presents quantum oscillation results for the CDW state of $LaTe_3$. Frequencies of $\beta \approx 0.52$ kT were found that could be ascribed to FS sheets that are unmodified by CDW formation. Other frequencies $\alpha \approx 0.060$ kT and $\gamma \approx 1.6$

kT were also observed that are attributed to the CDW-reconstructed FS. Given the clear quantum oscillations that have been seen in $LaTe_3$, the possibility is open for quantum oscillation studies for the other compounds in the series. Preliminary dHvA results for YTe_3, as presented here, reveal frequencies that are distinct than those for $LaTe_3$, which can be ascribed to different proportions of FS being gapped in YTe_3 as indicated by ARPES[10]. Measurements of YTe_3 can be easily extended to higher fields. The magnetic RTe_3 can be studied via Shubnikov de Haas oscillations in resistivity. In particular, a study of $TbTe_3$ at low temperatures can show whether or not it has a previously undetected second CDW transition. Such a systematic study of the quantum oscillations across the rare earth series can reveal trends in FS nesting across the series.

My thesis work, by illuminating the effect chemical pressure has on the multiple CDW transitions in RTe_3, sets the stage for a wealth of future investigations on this model system.

Appendix A

X-ray diffraction of modulated structures

A tutorial is presented for how superlattice peaks arise in modulated structures, and results are shown for a simple 1D model that qualitatively describes features in the $R\mathrm{Te}_3$ diffraction spectrum.

A.1 Origin of superlattice peaks

A crystal with atomic positions modulated by sinusoidal wave of wavevector q will produce an x-ray diffraction pattern with a pair of superlattice reflections spaced at $\pm q$ away from each original Bragg reflection. (These original Bragg reflections are now referred to average lattice reflections.)

As shown in Ch. 7 of *X-Ray Diffraction* by A. Guinier[45], a sinusoidal displacement $\mathbf{A}\sin(\mathbf{qx})$ results superlattice reflections I_1 with intensity

$$I_1 = \pi^2 (As\cos\alpha)^2 I_{orig} \tag{A.1}$$

Here, $\mathbf{s}$= ha^*+kb^*+lc^* is the reciprocal lattice vector and α is the angle between $\mathbf{A}$ and s. I_{Bragg} is the intensity of the original Bragg reflection. The average lattice reflections I_0 will in turn have their intensities reduced so that

$$I_0 = (1 - 2\pi^2(As\cos\alpha)^2)I_{orig} \tag{A.2}$$

such that the total intensity in each reciprocal unit cell remains the same. As s increases, the intensities of the superlattice reflections increase relative to the average lattice reflections, so that superlattice reflections are more easily observed away from the zone center.

When higher order terms are taken into account, higher harmonics are observed spaced $\pm 2q$, $\pm 3q$... $\pm nq$ on either side of the average lattice reflections. A rigorous treatment for a one-dimensional model[32] (here α= 0) shows that the intensities of the reflections are proportional to the square of Bessel functions such that

$$\begin{aligned} I_0 &= J_0^2(2\pi As)\cdot I_{orig} \\ I_1 &= J_1^2(2\pi As)\cdot I_{orig} \\ &\vdots \\ I_n &= J_n^2(2\pi As)\cdot I_{orig} \end{aligned}$$

Since $J_0^2 + 2J_1^2 + 2J_2^2 + ... = 1$, the total intensity sums to that of the original Bragg reflection I_{orig}. To first order in the Bessel functions, the first harmonic I_1 is proportional to A^2, and the second harmonic is proportional to A^4. Notice that these higher order components will arise for a purely sinusoidal modulation.

For CDWs, the order parameter $|\Delta_q|$ is proportional to the amplitude A of the corresponding sinusoidal modulation with wavevector q[1]. Yet Yao *et al.*[11] show

that for $R\mathrm{Te}_3$, higher orders of the order parameter exist such that $\Delta_{nq} \sim \Delta q^n$. These higher order terms Δ_{nq} correspond to sinusoidal modulations with wavevectors nq. The total modulation will thus contain not only the principal modulation$A\sin(qx)$ but also its higher harmonics $A_n \sin(nqx)$ such that $A_n \sim A^n$.

As a result both the second order diffraction harmonic and a sinusoidal modulation with wavevector $2q$ would create reflections at $\pm 2q$ with intensity proportional to $|\Delta|^4$. In Section 4.2.2, the second harmonic superlattice peak in ErTe_3 is discussed in this context.

A.2 Qualitative aspects of the $R\mathrm{Te}_3$ diffraction pattern

In this section, some aspects of the CDW in $R\mathrm{Te}_3$ are explored using simple one-dimensional models. In the first model, a unit cell of length a contains one atom per unit cell. The incommensurate wavevector q_1 is approximated as the commensurate value $q = 2/7a$, and a new unit cell is drawn that is composed of seven of the original unit cells. The structure factor can now be easily calculated, and the results are shown in Fig. A.1 for a modulation $A\sin(qx)$ where $A = 0.06\ a$.

Many traits of modulated structures can be seen with this simple model. Pairs of superlattice peaks are located $\pm q$ from the average lattice peaks. As H increases, the intensity of the average lattice peaks decreases and that of the superlattice increases. Also note that second harmonic superlattice peaks are present despite a being purely sinusoidal modulation.

Using the model, wavevectors of $q = 2/7a^*$ and $q' = 5/7a^*$ result in identical structure factors. This because q' lies outside the first Brillouin zone. As seen in seen

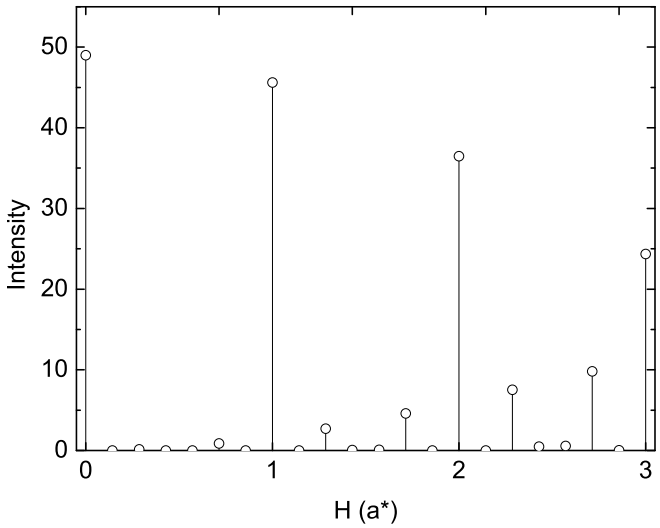

Figure A.1: The structure factor for one atom per unit cell, modulated by $A\sin(qx)$ where $q = 2/7a^*$.

in Fig. A.2, the functions $\sin(2\pi qx)$ and $-sin(2\pi q'x)$ are identical when sampled at integer values.

Now, a second atom is placed midway along the unit cell, and is assigned an arbitrary form factor which is 1/5 that of the first atom. Again a modulation $A\sin(qx)$ is applied where $q = 2/7a^*$. Here, a smaller amplitude $A = 0.01a$ is used. The results are shown Fig. A.3 plotted in open circles. The average lattice peaks alternate in intensity, very similar to that seen in scans along the c^* direction for $TbTe_3$ in Figs. 4.6 and 4.7, which is attributed to the two inequivalent Te atoms in the planes (and also two inequivalent sets of R-Te in the block layer). The superlattice peaks also alternate in intensity.

Plotted in closed circles Fig. A.3is the same model using a modulation of $q' = 5/7a^*$. Interestingly, it is not identical to that of $q = 2/7a^*$. The two wavevectors are no longer equivalent when there are two atoms per unit cell. It can be seen in

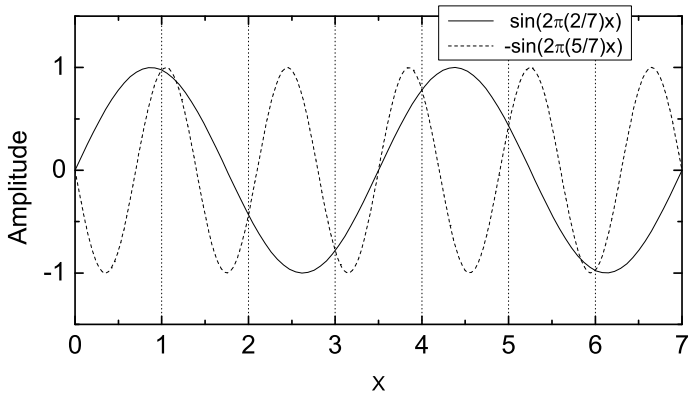

Figure A.2: The two function $\sin(2\pi(2/7)x)$ and $-\sin(2\pi(5/7)x)$ are equivalent when sampled at integer values.

Fig. A.2 that these two functions are no longer equivalent when they are sampled in half-integer increments. The alternating pattern of the superlattice peaks different for the two wavevectors. For the wavevector $q = 2/7a^*$, each of the taller average lattice peaks (i.e. every other average lattice peak) has correspondingly taller CDW peaks located adjacent to it at $\pm q$. For the wavevector $q = 2/7a^*$, each of the taller average lattice peaks has shorter CDW peaks immediately adjacent to it, with taller CDW peaks located at $\pm q'$.

This pattern can be compared with the diffraction patterns for $TbTe_3$ as shown in Figs. 4.6 and 4.7. The diffraction patterns for $TbTe_3$ also have alternating intensities. Most of these alternating patterns more closely resemble the q' model with more intense CDW peaks located at $\pm 5/7$ away from the more intense average lattice peaks. However, other data sets, such as for Fig. 4.7(b)(2 2 L), more closely resemble the q model with more intense superlattice peaks located $\pm 2/7$ away from the more intense average lattice peaks. The behavior of the second harmonics in the data is not well-described by either of the models, but this is not surprising as the model does

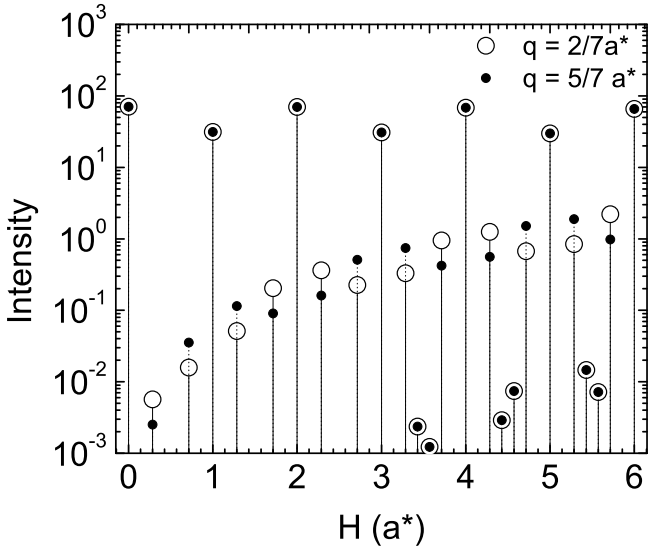

Figure A.3: The structure factor for two inequivalent atoms per unit cell, modulated by $A\sin(qx)$ where q is either $2/7a^*$ (open circles) or $5/7a^*$ (filled circles).

not incorporate higher order non-sinusoidal components. Given that the structure factor for the entire $R\mathrm{Te}_3$ crystal structure is much more complicated than the 1D model, it is interesting that such a simple one-dimensional model can mimic many of the qualitative features of TbTe_3 diffraction patterns.

When the modulation is purely incommensurate, the crystal structure is no longer periodic and it is difficult to describe the resulting unit cell. In such a case, superlattice reflections can be described as the projections of four-dimensional lattice points onto three-dimensional reciprocal space[46, 47]. The four-dimensional space group for $R\mathrm{Te}_3$ has been indexed by Malliakas *et al*[15, 16].

Appendix B

De Haas van Alphen oscillations

A very brief overview of the properties de Haas van Alphen (dHvA) oscillations is presented here. For a more thorough description, the reader is directed to *Magnetic Oscillations in Metals* by D. Shoenberg[48], or to review articles such as those by C. Bergemann *et* al[39, 49].

On the application of a field **B**, a free electron gas will quantize into concentric cylinders in k-space called Landau tubes. As **B** increases, the Landau tubes expand and cross the Fermi surface one by one, leading to an oscillatory behavior in the density of states at the Fermi energy, which results in corresponding oscillations in various thermodynamic and transport properties, collectively called quantum oscillations. De Haas van Alphen oscillations are those oscillations in magnetization.

These oscillations are periodic with inverse field with frequencies are proportional to Fermi surface(FS) areas. This proportionality is given by

$$F = \frac{\hbar A_F}{2\pi e} \tag{B.1}$$

where F is the frequency in units of field and A_F is the FS area. These FS areas

correspond to either maxima or minima cross-sections of the FS, where the cross-sections are taken perpendicular to **B**.

Smearing of the Fermi surface by thermal energy results in oscillations that are damped at higher temperatures. Oscillation amplitudes follow the Lifshitz-Kosevich relation

$$R_T = \frac{X}{\sinh X} \quad \text{where} \quad X = \frac{2\pi^2 k_B T m^*}{e\hbar B} \tag{B.2}$$

where m^* is the cyclotron mass.

Oscillations are also damped by impurities, leading to a Dingle reduction factor

$$R_D = \exp(-B_D/B) \quad \text{where} \quad B_D = \frac{\hbar}{2e}\frac{C_F}{l} \tag{B.3}$$

Here, C_F is the circumference of the orbit in k-space, and l is the mean-free path.

If a cylindrical FS is placed in a field **B** parallel to its axis, and is rotated such that the angle θ between its axis and **B** increases from zero, the cross-sectional area perpendicular to **B** will also increase. This cross-sectional area, and correspondingly its frequency as measured by dHvA, is proportional to $1/\cos\theta$, which is a U-shaped curve that goes to infinity as $\theta \to 90°$. (See Ch. 5 for $1/\cos\theta$ as drawn over experimental data.)

If the cylindrical FS is given a slight sinusoidal dispersion, two frequencies will be seen, one from the minimum of the FS cross-sectional area (the neck), and another from the maximum (the belly). These two frequencies will now have different angle dependencies. As θ increase for the neck orbital, its cross-sectional area will increase faster than that of the original cylindrical FS and will have an angle dependence that is "steeper" than $1/\cos\theta$. The belly orbital will increase slower with increasing θ and its curve will be "shallower" than $1/\cos\theta$.

As the angle increases, the frequency from the neck orbital will "catch up" with that of the belly orbital. This occurs at a particular "Yamaji" angle[40], which is further discussed and illustrated by C. Bergemann *et al.* in Ref.[39].

Bibliography

[1] G. Gruner, *Density Waves in Solids.* (Perseus Publishing, Cambridge, MA, 1994).

[2] M. D. Johannes and I. I. Mazin, arXiv:0708.1744 .

[3] T. C. Ozawa and S. J. Kang, J. Appl. Cryst. **37**, 679 (2004).

[4] B. K. Norling and H. Steinfink, Inorg. Chem **5**, 1488 (1966).

[5] J. Laverock, S. B. Dugdale, Z. Major, M. A. Alam, N. Ru, I. R. Fisher, G. Santi, and E. Bruno, Phys. Rev. B **71**, 085114 (2005).

[6] K. Y. Shin, V. Brouet, N. Ru, Z. X. Shen, and I. R. Fisher, Phys. Rev. B **72**, 85132 (2005).

[7] K. N. R. Taylor and M. I. Darby, *Physics of Rare Earth Solids* (Chapman and Hall LTD, London, 1972).

[8] S. Blundell, *Magnetism in Condensed Matter*, *Oxford master series in condensed matter physics* (Oxford University Press, New York, 2001).

[9] V. Brouet, W. L. Yang, X. J. Zhou, Z. Hussain, N. Ru, K. Y. Shin, I. R. Fisher, and Z. X. Shen, Phys. Rev. Lett. **93**, 126405 (2004).

[10] V. Brouet, W. L. Yang, X. J. Zhou, Z. Hussain, Z. X. Shen, J. Laverock, S. B. Dugdale, N. Ru, and I. R. Fisher, arXiv:0801.2672 .

[11] H. Yao, J. A. Robertson, E. A. Kim, and S. A. Kivelson, Phys. Rev. B **74**, 245126 (2006).

[12] E. DiMasi, M. C. Aronson, J. F. Mansfield, B. Foran, and S. Lee, Phys. Rev. B **52**, 14516 (1995).

[13] A. Kikuchi, J. Phy. Soc. Japan **67**, 1308 (1998).

[14] K. Y. Shin, private communication.

[15] C. Malliakas, S. J. L. Billinge, H. J. Kim, and M. G. Kanatzidis, J. Am. Chem. Soc. **127**, 6510 (2005).

[16] C. D. Malliakas and M. G. Kanatzidis, J. Am. Chem. Soc. **128**, 12612 (2006).

[17] G. H. Gweon, J. D. Denlinger, J. A. Clack, J. W. Allen, C. G. Olson, E. DiMasi, M. C. Aronson, B. Foran, and S. Lee, Phys. Rev. Lett. **81**, 886 (1998).

[18] H. Komoda, T. Sato, S. Souma, T. Takahashi, Y. Ito, and K. Suzuki, Phys. Rev. B **70**, 195101 (2004).

[19] A. Sacchetti, L. Degiorgi, T. Giamarchi, N. Ru, and I. R. Fisher, Phys. Rev. B **74**, 125115 (2006).

[20] A. Fang, N. Ru, I. R. Fisher, and A. Kapitulnik, Phys. Rev. Lett. **99**, 046401 .

[21] H. Kim, C. Malliakas, A. Tomic, S. Tessmer, M. Kanatzidis, and S. Billinge, Phys. Rev. Lett. **96**, 226401 (2006).

[22] Y. Iyeiri, T. Okumura, C. Michioka, and K. Suzuki, Phys. Rev. B **67**, 144417 (2003).

[23] N. Ru and I. R. Fisher, Phys. Rev. B **73**, 033101 (2006).

[24] E. DiMasi, B. Foran, M. C. Aronson, and S. Lee, Chem. Mater **6**, 1867 (1994).

[25] J. Laverock and S. B. Dugdale, private communication.

[26] *Binary alloy phase diagrams second edition plus updates.*, edited by T. B. Massalski (ASM International, Materials Park, Ohio, 1996).

[27] H. C. Montgomery, J. Appl. Phys. **42**, 2971 (1971).

[28] N. Ru, C. L. Condron, G. Y. Margulis, K. Y. Shin, J. Laverock, S. B. Dugdale, M. F. Toney, and I. R. Fisher, Phys. Rev. B **77**, 035114 (2008).

[29] C. L. Condron, J. H. Chu, I. R. Fisher, and M. F. Toney, private communication.

[30] International Centre for Diffraction Data (ICDD) Powder Diffraction File (PDF) 2005.

[31] J. Pouget, C. Noguera, A. Moudden, and R. Moret, Journal de Physique **46**, 1731 (1985).

[32] A. J. C. Wilson, *X-ray Optics; the Diffraction of X-rays by Finite and Imperfect Crystals*, *Methuen's monographs on physical subjects*, 2nd ed. (Methuen & Co LTD, London, 1962).

[33] K. Yamaji, J. Phy. Soc. Japan **51**, 2787 (1982).

[34] K. Yamaji, J. Phy. Soc. Japan **52**, 1361 (1983).

[35] K. Maki and A. Virosztek, J. Magn. Magn. Mat. **90/91**, 758 (1990).

[36] B. Barbiellini, S. B. Dugdale, and T. Jarlborg, Computational Materials Science **28**, 287 (2003).

[37] R. G. Moore and Z.-X. Shen et al., private communication.

[38] N. Ru, A. Rost, R. A. Borzi, J. Laverock, S. B. Dugdale, A. P. Mackenzie, and I. R. Fisher, in progress.

[39] C. Bergemann, A. Mackenzie, S. Julian, D. Forsythe, and E. Ohmichi, Advances in Physics **52**, 639 (2003).

[40] K. Yamaji, J. Phys. Soc. Japan **58**, 1520 (1989).

[41] A. Sacchetti, E. Arcangeletti, A. Perucchi, L. Baldassarre, P. Postorino, S. Lupi, N. Ru, I. R. Fisher, and L. Degiorgi, Phys. Rev. Lett. **98**, (2007).

[42] M. B. Maple, private communication.

[43] A. Sacchetti, F. Pfuner, C. L. Condron, J. H. Chu, I. R. Fisher, and L. Degiorgi, private communication.

[44] N. Ru, J. H. Chu, and I. R. Fisher, in progress.

[45] A. Guinier, *X-Ray Diffraction: In Crystals, Imperfect Crystals, and Amorphous Bodies* (Dover Publications, Inc., New York, 1994).

[46] A. Yamamoto, Acta. Cryst. **A 38**, 87 (1982).

[47] P. M. de Wolff, Acta. Cryst. **A 37**, 625 (1981).

[48] D. Shoenberg, *Magnetic oscillations in metals.* (Cambridge University Press., Cambridge, UK, 1984).

[49] C. Bergemann, Ph.D. thesis, University of Cambridge, UK, 1999.

Errata

Figs. 4.4 and 6.2: "Increasing T" and "Decreasing T" labels are interchanged.

Fig. 6.15: Orientations for resistivity measurements are as follows: (a) Currents along *ac*-plane. (b) Currents along *b*-axis. (c) Currents along *ac*-plane.